Summer 8-15-2019

Solid-State NMR of CO2 Mineralization and NMR Crystallography

Jinlei Cui
Washington University in St. Louis

Recommended Citation

Cui, Jinlei, "Solid-State NMR of CO2 Mineralization and NMR Crystallography" (2019). *Arts & Sciences Electronic Theses and Dissertations*. 1847.
https://openscholarship.wustl.edu/art_sci_etds/1847

WASHINGTON UNIVERSITY IN ST. LOUIS

Division of Chemistry

Dissertation Examination Committee:
Sophia E. Hayes, Chair
Alexander Barnes
Julio M. D’Arcy
Joseph A. Fournier
Jill D. Pasteris

Solid-State NMR of CO_2 Mineralization and NMR Crystallography

by
Jinlei Cui

A dissertation presented to
The Graduate School
of Washington University in
partial fulfillment of the
requirements for the degree
of Doctor of Philosophy

August 2019
St. Louis, Missouri

Table of Contents

List of Figures

List of Tables

List of Abbreviations

BSE	Backscatter Electron
CS	Chemical Shift
CSA	Chemical Shift Anisotropy
CP	Cross Polarization
DFT	Density Functional Theory
DOR	Double Rotation
EFG	Electric Field Gradient
FID	Free-Induction Decay
GCS	Geological Carbon Sequestration
GGA	Generalized Gradient Approximation
PAW	Projector Augmented Wave
MAS	Magic Angle Spinning
MQMAS	Multiple Quantum
NMR	Nuclear Magnetic Resonance
PBE	Perdew-Burker-Ernzerhof
PXRD	Powder X-Ray Diffraction
REDOR	Rotational-Echo Double-Resonance
RF	Radio Frequency
RFDR	Radio Frequency Driven Recoupling
SSNMR	Solid-State Nuclear Magnetic Resonance
TMS	Tetramethylsilane
VASP	Vienna Ab-initio Simulation Package
vdW	Van der Waals

Acknowledgments

First, I would like to express my greatest gratitude to my advisor, Dr. Sophia Hayes. She is a smart and responsible advisor. Her continues excitement about the research and profound knowledge in the field of chemistry and NMR technology is extremely contagious. I am grateful for her solid support over the past four years. Without her guidance, this project and dissertation would not be possible. In addition, she is not just an advisor for my search but also a friend and knowledgeable guide in my life.

Second, I want to acknowledge the collaborators who have helped and provided the support for the DOE-NETL, DIBBS and CSMC project. I would like to thank Dr. Daniel Giammar, Dr. Rachel Wells and Dr. Xiong Wei, who have helped to prepare and analyze the samples of CO_2 mineralization in the DOE-NETL project, and from whom I learned much geologic chemistry. I also want to thank Dr. Mark Conradi, who gave me the opportunity to study the NMR theory from him. I want to express my gratitude to Dr. David Olmsted and Dr. Mark Asta, who have supported me for the NMR computation. I am also so fortunate to have Dr. Anil Mehta as a close collaborator, who has expertise in REDOR experiment and simulation. I want to thank Dr. Ivan Hung, Dr. Zhehong Gan and Dr. Kuizhi Chen for their support and discussion about the high field NMR in the CSMC project.

Third, I want to thank the individuals with whom I have spent the last four year in my lab. Dr. Zayd Ma is a great mentor and leader for teaching me to run the NMR experiment. Dr. Blake Hamman is a great friend and resource in the lab. I still remember the days that we fixed the NMR probe together. Dr. Matthew Willmering is brilliant and taught me the basic theory and experimental details of NMR. I also miss Dr. Robert Marti, who has been a co-worker and dis-

cussed the research with me. I also really appreciate the help of Dr. Erika Sesti. She is smart and built the NMR probe for the study. Dr. Chia-Hsin Chen is a nice friend and resource for discussion about the research. Dr. Yvonne Afriyie and I entered the group together, and we co-worked in the CSMC project. Dr. Daphna Shimon has profound knowledge about DNP and solid-state NMR. Michael West is a kind friend. We talked a lot about not only the research but also the lives and cultures in America and China. Sun He is accommodating in the computation. My physics coworkers also have helped me throughout my graduate career. Dr. Sam Emery is a kind friend and has such profound knowledge of hardware. Without him, it is impossible for me to fix the instruments and keep working. Dr. Hongyang Zou is also from China, and we have a good time together, whenever we meet for discussion.

Fourth, I owe a lot to my committee members, Prof. Julio D'Arcy, Prof. Alexander Barnes, Prof. Jill Pasteris and Prof. Joseph Fournier. They have been sharing their experience, asking excellent questions and providing feedback regarding my research.

Finally, I want to thank all of the friends in my life. I am so honored to be a part of your life and have a good time with you. I also want to acknowledge my parents, Fengling Wang and Baoqi Cui. I am so proud to be your son. And I want to thank my best friends in China, Hao Ma and Bin Wang. You are the best friends for me forever and thank you for taking care of my parents when I am not there. I also want to express my thanks to all my family and relatives for helping my parents and me in my life.

This dissertation described herein was funded by several grants: the Department of Energy under Award Number DE-FE0023382; the U.S. National Science Foundation (NSF), Award Number 1640899 and U.S. National Science Foundation (NSF), Award Number 1606982.

Jinlei Cui

Washington University in St. Louis

August 2019

Dedicated to my parents, Fengling Wang and Baoqi Cui

Abstract of the Dissertation

Solid-State NMR of CO_2 Mineralization and NMR Crystallography

by

Jinlei Cui

Doctor of Philosophy in Physical Chemistry

Washington University in St. Louis, August 2019

Research Advisor: Professor Sophia E. Hayes

The work described in this dissertation has been accomplished by using solid-state nuclear magnetic resonance (SSNMR) spectroscopy to investigate CO_2 mineralization and to refine the positions of protons in the crystalline system. The reaction of forsterite (Mg_2SiO_4) and $^{13}CO_2$ is presented here, which is measured using in-situ ^{13}C NMR spectroscopy without removing the sample from the reactor. ^{29}Si SSNMR is used to investigate the reaction of forsterite with $^{13}CO_2$ in the presence of water or NaCl brine as a function of depth in the sample. Additionally, we also show that NMR crystallography can significantly improve structure refinement of hydrogens' positions in hydrated materials. $^{13}C\{^1H\}$ rotational-echo double-resonance (REDOR) and ^{13}C chemical shift anisotropy (CSA) tensor values from SSNMR are exploited as the standard in NMR crystallography. The optimized atomic coordinates are validated by comparing DFT prediction to experimental data through $^{13}C\{^1H\}$ REDOR and ^{13}C CSA tensors. The research presented herein demonstrates that solid-state NMR is a useful tool for studying the CO_2 mineralization mechanism and the understanding of the crystalline structure of CO_2 mineralization products.

Chapter 1:

Introduction

1.1 CO_2 Capture and Storage

The excessive emission of CO_2 into the atmosphere may lead to severe environment issues by global warming. Over the past 150 years, human activity has made the most substantial contribution to increasing level of CO_2 in the atmosphere.[1] The IMO Marine Environment Protection Committee has made a proposal to reduce CO_2 output by 50 percent by 2050, which requires an extensive portfolio of CO_2 capture and storage technologies, if we continue to use fossil fuels as an energy source.

Geological carbon sequestration (GCS) is one approach to mitigate atmospheric CO_2 by storing it deep underground and has significant economic potential in the future.[2] GCS offers several trapping mechanisms: (1) stratigraphic and residual entrapment (stuck beneath the low-permeability caprocks); (2) solubility entrapment (dissolution of CO_2 in aqueous phases underground); (3) hydrodynamic entrapment (storage as the supercritical CO_2 phase underground); (4) mineral entrapment (where CO_2 forms stable solid carbonate precipitates). Currently, most of the completed and ongoing geologic carbon sequestration projects inject CO_2 into sandstone because of its large storage capacity for CO_2 storage.[3,4] For instance, since 1996, StatoilHydro has been injecting 1 million metric tons of CO_2 into a sandstone reservoir, which is 1000 m below the sea surface in the North Sea.[5] In Canada, the world's first commercial post-combustion coal-fired carbon capture and storage projects were started in 2014.[6]

GCS is a promising strategy for mitigating the impacts of anthropogenic CO_2 emissions on global climate change. The ultimate fate of injected carbon includes free supercritical CO_2 trapped within pores and beneath capping formations, dissolved CO_2 in aquifers, and carbonate minerals formed upon CO_2-water-rock reactions.[7,8] Most geologic systems currently used or proposed for carbon sequestration are sandstone and carbonate saline aquifers.[9] These systems are attractive because they have porosity and permeability that facilitate injection of CO_2, but they have limited capacities for mineral trapping because of the dearth of silicate minerals that contain the Ca, Mg, and Fe necessary for carbonate mineral formation. However, Mg- or Ca-rich basalts are target systems that can provide excellent mineral carbonation. [10–13]

Nuclear magnetic resonance (NMR) spectroscopy is an inherently element-selective, powerful and non-destructive analytical technology. Solid-state NMR (SSNMR) can identify the various carbonate species in the mineralization process (bicarbonate, CO_2 gas, supercritical CO_2, solid-state carbonate and amorphous or crystalline species), which are often impossible for powder X-ray diffraction (PXRD) to characterize. Our group has been focusing on developing SSNMR methods for investigating CO_2 mineralization. We first reported a home-built elevated pressure and temperature probe in 2013 (shown schematically in Figure 1.1) and used it to monitor mineralization in an unmixed, batch reactor by static NMR.[14] The pH, which is very important for mineralization, was also determined by using ^{13}C NMR measurement in this probe.[15] Some representative static ^{13}C NMR results are shown in Figure 1.1 simply to illustrate the kind of data one can collect.

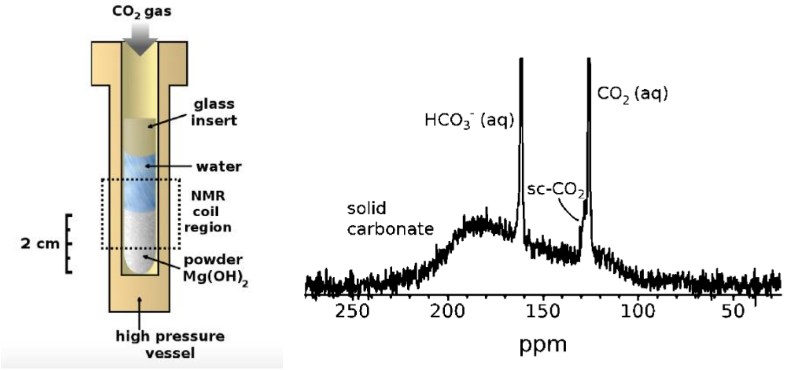

Figure 1.1 Zirconia high-pressure vessel used in the NMR sample space for in-situ ^{13}C static NMR of $^{13}CO_2$ introduced to a slurry of water and brucite ($Mg(OH)_2$). The spectrum was recorded after 58 hours at 80°C and 88.5 bar pressure.

However, our limited understanding of the extent and mechanisms of carbon sequestration in fractured basalts poses challenges to accurately estimate the CO_2 storage capacity and ultimately to ensuring GCS security. Also, the geological sequestration of CO_2 is improved by obtaining a fundamental understanding of the structure and bonding of carbonate minerals. Such fundamentals can help to develop the predictive simulations and thermodynamic models to optimize the conditions for carbonate formation and a more in-depth understanding of the mechanism of CO_2 mineralization. Thus, in this project, we are focusing on two targets. First, we are studying a GCS reaction in forsterite (Mg_2SiO_4) with the groups of Prof. Daniel Giammar (Washington University in St.Louis) and Prof. Brian Ellis (Michigan State University) at elevated temperatures and pressures to understand better the location of carbonate minerals in fractures and the macroscopic changes in morphology of the starting minerals. We are also focusing on the study of the structure of CO_2 mineralization products, such as hydromagnesite and nesquehonite, using “NMR Crystallography” techniques to determine precise atomic coordinates.

1.2 Nuclear Magnetic Resonance

After the first detection of magnetic resonance in 1937 by Rabi,[16] NMR has experienced a steady increase in popularity. The rapid development of NMR is spurred by the invention of new techniques that enable high resolution to be achieved. Today, NMR spectroscopy has been widely applied in many fields, such as chemistry, physic, biology, pharmacy, and materials science. NMR is a powerful characterization tool, in that it monitors the local bonding environment surrounding an isotope of interest. This section will provide the necessary introduction of the theory of NMR and some definitions of NMR terms used in this dissertation.

1.2.1 Spin Quantum Number

NMR is performed in the presence of an external magnetic field, denoted as B_o. In the presence of an external magnetic field, the nuclear spin states are split into two or more energy levels due to interaction between the spin magnetic moment and the external magnetic field. For nuclei with non-zero spin angular momentum (I), there will be ($2I$+1) energy levels in the presence of the magnetic field given by the equation 1.1: [17]

$$E_{m_I} = -m_I \hbar \gamma B_o \tag{1.1}$$

where m_I is z-component of spin angular momentum and has the value of $-I$, $-I+1$,…..$I-1$, or I; γ is the magnetogyric ratio of nuclei (ratio of magnetic moment to angular momentum), which is nuclear isotope specific; and ħ is the Planck's constant divided by 2π; B_o is the external magnetic field. A simple example will be for spin =1/2 nuclei, such as ^{13}C. For ^{13}C, there will be two energy levels due to the external magnetic field, which corresponds to parallel and anti-parallel state. The energy difference between these two energy states is called the Zeeman splitting, and is given by equation 1.2

$$\Delta E_{Zeeman} = \hbar\gamma B_o = \hbar\omega_o \tag{1.2}$$

where ω_o is the Larmor frequency. Figure 1.2 shows the energy of the spin state splitting in an external magnetic field.

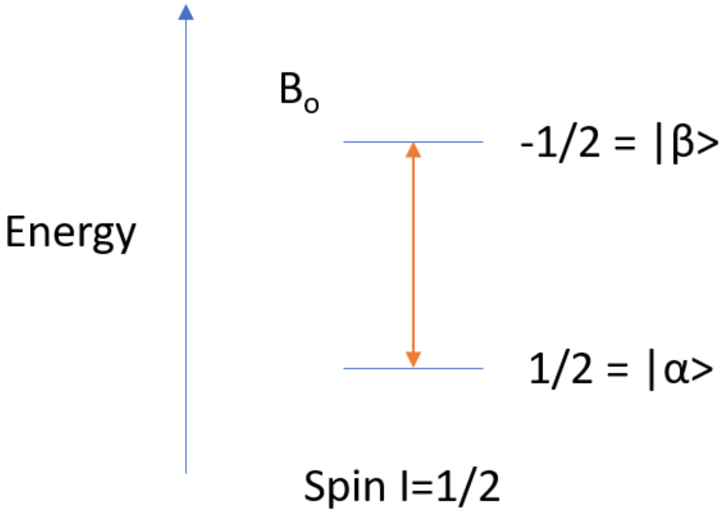

Figure 1.2 Energy levels for nuclei with spin number I=1/2 in an external magnetic field (B_o)

NMR requires a population difference between the spin states. In the presence of a magnetic field, the equal population differences can be described by equation 1.3.

$$\frac{n_\alpha}{n_\beta} = e^{\gamma\hbar B_o/kT} \tag{1.3}$$

where n_α/n_β is the population ratio between two nuclear spin states, k is Boltzmann constant and T is the temperature of the sample. From the definition of population ratio, we find that the population can be manipulated by two factors, B_o and T. Therefore, scientists have been working on building higher magnetic field magnets (such as 36T in the National High Magnetic Field Laboratory)[18] or decreasing the temperature of the sample (such as lowering temperature of NMR experiment by cryogenic liquids) to improve the NMR signal. Besides that, dynamic nuclear polarization can increase the population differences by transferring the polarization from electron to nuclei.[19]

1.2.2 NMR Hamiltonian

In this section, we will focus on the basic theory of SSNMR. The total Hamiltonian ($\hat{H}_{NMR}$) for SSNMR is the sum of multiple interactions, which can shift, broaden or split the NMR signal. Equation 1.4 can describe the total Hamiltonian relevant for NMR:

$$\hat{H}_{NMR} = \hat{H}_{Z} + \hat{H}_{CS} + \hat{H}_{D} + \hat{H}_{J} + \hat{H}_{Q} + \hat{H}_{RF} \tag{1.4}$$

The first term is the Zeeman Hamiltonian for the splitting of the nuclear spin state in the magnetic field. It is the dominant interaction in the NMR Hamiltonian and determines the Larmor frequency. It is described by equation 1.5:

$$\hat{H}_{Z} = -\gamma \hbar B_{o} \hat{I}_{Z} \tag{1.5}$$

where $\hat{I}_Z$ is the spin operator in the Z-direction.

The second term is the chemical shift Hamiltonian, and it is used to describe the chemical shift interaction. It can be depicted by equation 1.6:

$$\hat{H}_{CS} = -\gamma \hbar \sigma B_{o} \hat{I} \tag{1.6}$$

The chemical shift Hamiltonian is due to the secondary magnetic field generated by the electrons surrounding the nuclei. This field tends to shield the nucleus from the external magnetic filed B_o, and the interaction between this field and the nuclei is the shielding interaction. In general, the electron distribution around the nuclei in a molecule is not spherically symmetric. Therefore, the size of the shielding interaction will depend on the orientation of the molecule in the magnetic field. The shielding tensor, σ, is a second rank tensor and describes the orientation dependence of the chemical shielding interaction with the external magnetic field. A matrix usually represents the shielding tensor σ:[17]

$$\sigma = \begin{bmatrix} \sigma_{XX} & \sigma_{XY} & \sigma_{XZ} \\ \sigma_{YX} & \sigma_{YY} & \sigma_{YZ} \\ \sigma_{ZX} & \sigma_{ZY} & \sigma_{ZZ} \end{bmatrix}$$

The shielding tensor includes an isotropic and anisotropic portion. By diagonalizing the matrix, the system is transformed from lab frame to fixed molecular frame (also called as principal axis system). As a result, the principal value of the chemical shielding tensor can be defined with matrix elements denoted by σ_{XX}, σ_{YY} and σ_{ZZ}, and all off-diagonal elements, like σ_{XY}, will be zero.

In the static SSNMR experiment, the chemical shift anisotropy (CSA) lineshape of SSNMR can be described by the three-principal chemical shifts tensor elements, δ_{XX}, δ_{YY} and δ_{ZZ}. In this study, the Haeberlen convention[20] is applied and defined in the following equations (from 1.7 to 1.10) to depict the chemical shift anisotropy. One series of simulated CSA-broadened lineshapes for different values of η_{CSA} are represented in Figure 1.3

$$\delta_{iso} = \frac{1}{3}(\delta_{XX} + \delta_{YY} + \delta_{ZZ}) \tag{1.7}$$

$$\delta_{aniso} = \delta_{ZZ} - \delta_{iso} \tag{1.8}$$

$$|\delta_{ZZ} - \delta_{iso}| \geq |\delta_{XX} - \delta_{iso}| \geq |\delta_{YY} - \delta_{iso}| \tag{1.9}$$

$$\eta_{CSA} = \frac{\delta_{YY} - \delta_{XX}}{\delta_{aniso}} \tag{1.10}$$

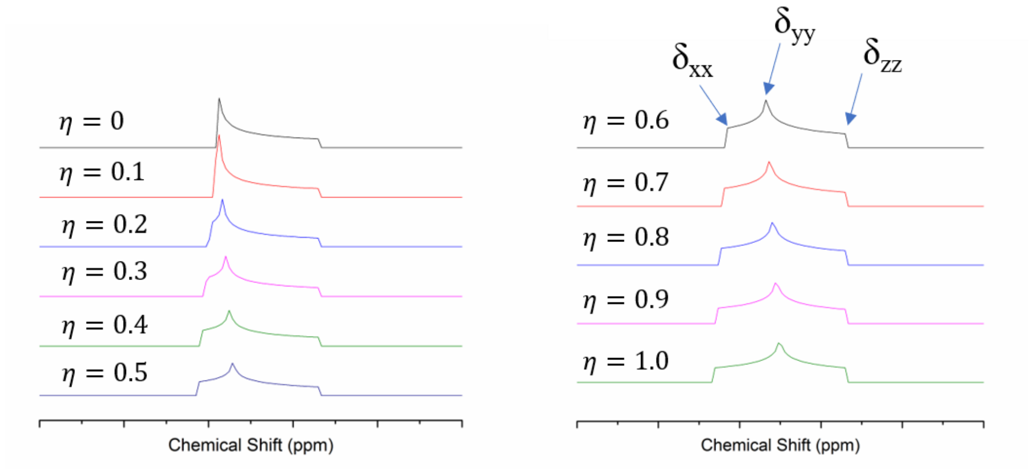

Figure 1.3 Series of static NMR lineshapes with different η_{CSA} values, from 0 to 1.0.

The third term is the dipolar Hamiltonian. It is used to describe the through space interaction between two nuclei. For instance, if there are two different nuclei (denoted I and S), the dipolar interaction Hamiltonian between them is, to first order, given by equation 1.11:[17]

$$\hat{H}_D = \frac{\gamma_I \gamma_S \hbar}{r^3}(1 - 3cos^2\theta)\hat{I}_Z\hat{S}_Z \tag{1.11}$$

where r is the distance between the two nuclei; γ_I and γ_S are the gyromagnetic ratios of nuclei I and S; θ is the angle between the internuclear vector and the external magnetic field B_o; $\hat{I}_Z$ and $\hat{S}_Z$ are the spin operators in the z-direction of both nuclei. This interaction will also introduce broadening to the SSNMR signal. Two common techniques can be applied to eliminate the dipolar coupling: one is magic angle spinning (MAS) NMR,[21] and another is decoupling.

Because the dipolar interaction is related to the distance between two nuclei, it is also used to measure the distance for structural information. Several NMR pulse sequences have been developed to re-introduce the dipolar interaction as a tool to obtain the distance between interesting nuclei during MAS, such as rotational echo double resonance (REDOR)[22] and radio frequency driven recoupling (RFDR).[23] In the following section, a detail of REDOR pulse sequence will be discussed.

The fourth term is the J-coupling between two nuclear spins. J-coupling occurs through the bonding between two nuclei. The J-coupling between two nuclei can be described by equation 1.12:

$$\hat{\mathrm{H}}_J = J\hat{\mathrm{I}}\hat{\mathrm{S}} \tag{1.12}$$

where J is the J-coupling constant. In SSNMR, J-coupling is usually not observed since its strength is too small compared to other interactions. Therefore, we do not discuss J-coupling too much here.

The fifth term is the quadrupolar Hamiltonian for nuclei with spin number > ½. This Hamiltonian is used to depict the interaction between a nuclear electric quadrupole moment and an electric field gradient. The electric field gradient comes from the distribution of other nuclei or electrons in the sample. In the periodic table, 74 % of NMR active nuclei have a spin number >1/2. Equation 1.13 describes the quadrupolar Hamiltonian:[24]

$$\hat{\mathrm{H}}_Q = \frac{eQ}{6I(2I-1)\hbar}\hat{\mathrm{I}} \cdot eq \cdot \hat{\mathrm{I}} \tag{1.13}$$

where eq is the electric field gradient (EFG) at the nuclei (I); $\hat{\mathrm{I}}$ is nuclear spin operator, and Q is the nuclear quadrupole moment. Quadrupolar interaction contains the first-order and second-order interactions, which always broadens the SSNMR lineshape. The first-order quadrupolar Hamiltonian can be averaged out by MAS since it also contains $3\cos^2\theta$-1 in the expression. However, the second-order quadrupolar Hamiltonian has higher order related to angle θ. Therefore, it can't be simply averaged out by MAS. Multiple quantum magic angle spinning (MQMAS) and double rotation (DOR)[25] have been developed to solve this problem.

1.2.3 Magic Angle Spinning

To improve the resolution of the SSNMR signal, magic angle spinning was developed by E.R. Andrew.[26] In the experiment, the NMR rotor spins at an angle θ_m (54.7°) between the rotor and the external magnetic field B_o. θ_m is called the magic angle and leads to a result through equation 1.14:

$$3cos^2\theta_m - 1 = 0 \tag{1.14}$$

Figure 1.4 shows the magic angle spinning set for a spin rotor, and it is depicted in the laboratory frame. ω_r is the rotor's spinning angular frequency.

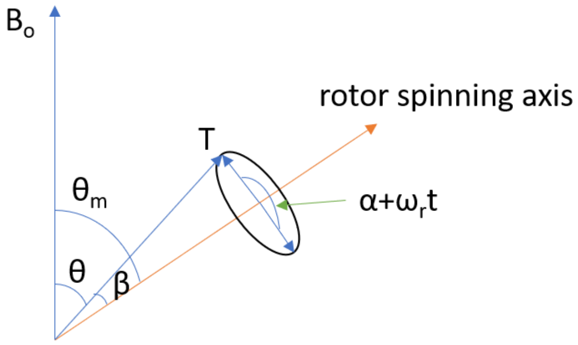

Figure 1.4 Relative position of a spinning rotor in an external magnetic field (B_o). The vector T could be the internuclear vector for dipolar interaction, the principal Z axis for the EFG tensor and the principal axis for the chemical shift tensor.

To prove this, the lab frame is tilted and shown in Figure 1.5, where i, j, k, h, r_1, and r_2 are unit vectors along each orientation.

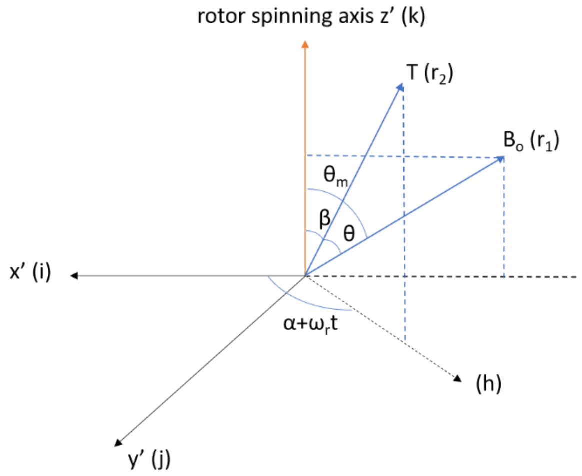

Figure 1.5 Tilted relative position of a spinning rotor in an external magnetic field (*B_o*).

The equations (from 1.15 to 1.20) are used to prove that the Hamiltonian is zero in one spin cycle rotor.[27]

$$\hat{h} = \hat{\imath}cos(\alpha + \omega_r t) + \hat{\jmath}sin(\alpha + \omega_r t) \tag{1.15}$$

$$\widehat{r_2} = \hat{h}sin\beta + \hat{k}cos\beta = \hat{\imath}sin\beta cos(\alpha + \omega_r t) + \hat{\jmath}sin\beta sin(\alpha + \omega_r t) + \hat{k}cos\beta \tag{1.16}$$

$$\widehat{r_1} = -\hat{\imath}sin\theta_m + \hat{k}cos\theta_m = -\sqrt{\frac{2}{3}}\hat{\imath} + \sqrt{\frac{1}{3}}\hat{k} \tag{1.17}$$

$$cos\theta = \widehat{r_1} \cdot \widehat{r_2} = -\sqrt{\frac{2}{3}}sin\beta cos(\alpha + \omega_r t) + \sqrt{\frac{1}{3}}cos\beta \tag{1.18}$$

$$1 - 3cos^2\theta = -[sin^2\beta cos2(\alpha + \omega_r t) - \sqrt{2}sin2\beta cos(\alpha + \omega_r t)] \tag{1.19}$$

$$\overline{1 - 3cos^2\theta} = \frac{1}{T_r}\int_0^{T_r}(1 - 3cos^2\theta)dt = -\frac{1}{T_r}\left[\frac{sin^2\beta cos2(\alpha+\omega_r t)}{2\omega_r} - \frac{\sqrt{2}sin2\beta cos(\alpha+\omega_r t)}{\omega_r}\right]\Big|_0^{T_r} = 0 \tag{1.20}$$

T_r is the time for one spin cycle and $\omega_r * T_r$ equals 2π. As we prove here, the average of $3\cos^2\theta - 1$ over one spin cycle is zero. Equation 1.19 could be applied to the dipolar interaction, the chemical shift anisotropy, and the first-order quadrupole interaction through MAS.

1.2.4 Spin Process and Detection

In the absence of a magnetic field, all the magnetic moments are randomly orientated. As a result, they will cancel each other out, and there is no net moment. However, in the presence of a magnetic field, there is a net magnetization along the magnetic field direction (the Z-axis) at equilibrium, which can be represented by a magnetization vector. In the NMR experiment, an external radio frequency pulse (RF, denoted as B_1) is applied perpendicular to the external filed B_o. It will rotate the net magnetization to a single plane. Once the pulse B_1 is stopped, the nuclear spin in the plane will process at Larmor frequency. This process will induce a current in the coil, which is measured by the spectrometer as a function of time. It will result in a signal known as the free induction decay (FID). The FID will be Fourier transformed into the frequency domain, which is a typical NMR spectrum. The equation 1.21 can express the angle of nuclear spin rotation by the pulse B_1: [17]

$$\alpha = \gamma t_p B_1 \tag{1.21}$$

where α is the degree of rotation and γ is the gyromagnetic ratio, t_p is the pulse length, B_1 is the pulse strength in Tesla. As the vector model illustrated in Figure 1.6, a 90 ° pulse will yield the largest amount of signal, and 180 ° pulse will completely flip magnetization to the -z axis and generate a zero signal, because only the magnetization in xy-plane will be detected by the NMR coil. The classical evolution of magnetization is formally described by the Bloch equations, which will not be discussed in detail here. We will also not discuss the density matrices here.

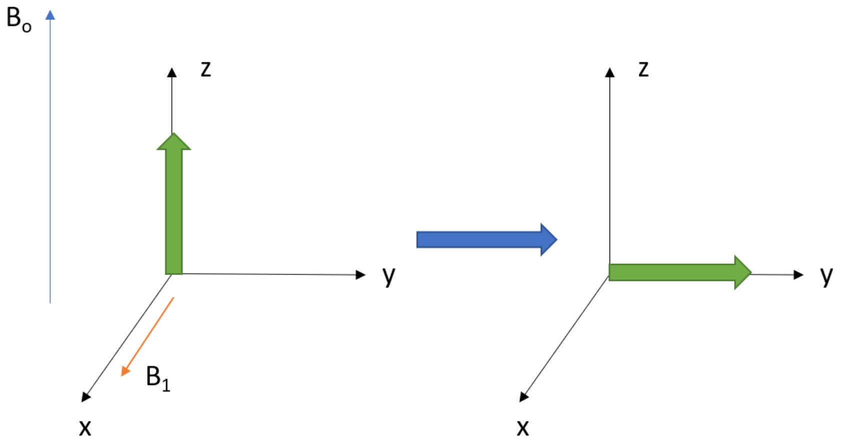

Figure 1.6 Basic vector model of NMR represents the changing of bulk magnetization after 90° pulse.

After the 90 ° pulse, the net magnetization is along the y axis. The transverse components of magnetization (M_{xy}, the magnetization in the xy-plane) will decay or dephase by the interactions among the spins of different nuclei. This relaxation time is called T_2 (spin-spin relaxation time or transverse relaxation time) The expression for T_2 can be found in equation 1.22:

$$M_{xy} = M_{xy}^{0}(e^{-t/T_2}) \tag{1.22}$$

where M_{xy} is the magnetization of spins in the xy-plane for a give delay time, t, and M^0_{xy} represents the full magnetization of spin at time following B_1 pulse.

In addition, after the pulse, the net magnetization in z-axis will return to its initial maximum value parallel to B_o in the presence of the external magnetic field. The recovery of longitudinal component of magnetization (M_z) is accompanied by the interactions between the nuclei and the system around it, known as the “lattice”. This relaxation time for this is named as T_1 (spin-lattice relaxation time or longitudinal relaxation time) and expressed in Equation 1.23:

$$M_z^{(t)} = M_z^{(0)}(1 - e^{-t/T_1}) \tag{1.23}$$

where $M_z^{(t)}$ is the longitudinal magnetization along the B_o at a time t, and $M_z^{(0)}$ is the represents the initial maximum magnetization before B_1. In solid state NMR, T_2 and T_1 have different values. The typical T_2 has a value of several milliseconds, but T_1 could be as long as hours. Both T_1 and T_2 both contribute to the decay of the NMR signal resulting from the precession of magnetization after B_1.

1.3 NMR Pulse Sequence

1.3.1 Bloch Decay

Bloch decay (also known as “pulse and acquire” or “one-pulse NMR”) is achieved by acquiring the NMR signal after a single pulse. The pulse width can be varied, and different intensities of the NMR signal will be observed. The signal intensity will be a sine curve related to the pulse width, which is known as a nutation curve. The NMR scientist usually applies this experiment to find the pulse duration for 90° pulse, which gives the maximal magnetization signal. Figure 1.7 shows the pulse sequence of “Bloch decay”. The angel α means the alternation of angle for the nuclear spin after pulse. For instance, 90° pulse means the nuclear spin will be change from z axis to xy plane after pulse, as described in the previous section.

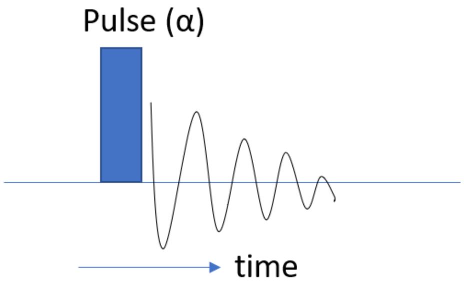

Figure 1.7 Schematic of the NMR pulse sequence—Bloch decay. The blue box represents the α angle pulse.

1.3.2 Hahn Echo

Different from the Bloch decay, the pulse sequence of the Hahn echo consists of two pulses in one sequence. The first Hahn echo experiment was detected by Erwin Hahn in 1950.[28] The typical pulse sequence of the Hahn echo is expressed in Figure 1.8.

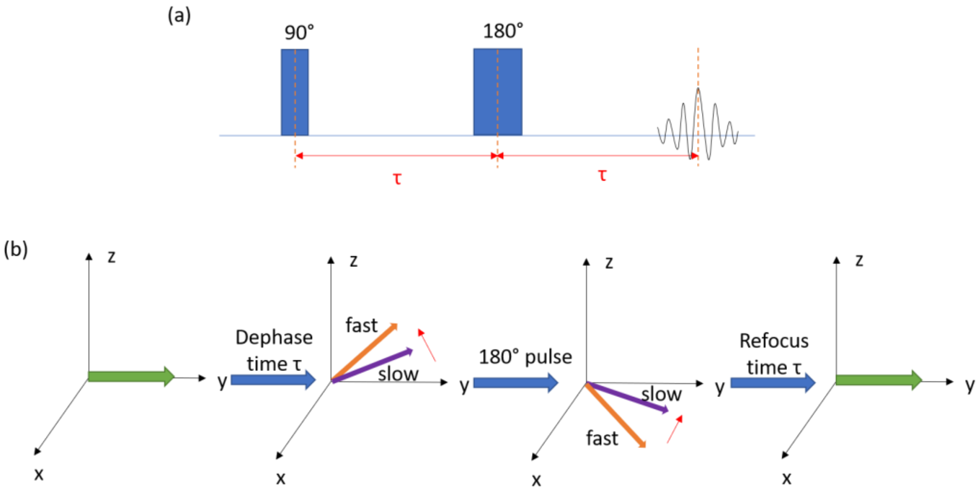

Figure 1.8 (a) Schematic of the NMR pulse sequence—Hahn Echo. The resulting echo is formed after time τ. (b) The basic vector model for Hahn Echo.

In Figure 1.8a, the first excitation pulse is a 90° pulse, followed by a time interval τ, and the second pulse is a 180° refocusing pulse. This type of pulse sequence results in an echo forming at time τ after the second pulse. Figure 1.8b shows the vector model for Hahn echo after the 90° pulse. The 180° pulse is used to rephase the magnetization. The Hahn echo pulse sequence can be used to refocus the signal and remove the processing in the offset of the NMR receiver during the experiment. It is also used to determine the T_2 of the NMR signal. Besides, in combination with the phase cycle, Hahn echoes are used to suppress signals generated by imperfections in the spectrometer hardware or acoustic ringing.

1.3.3 Rotational Echo Double Resonance

REDOR is one of the most widely used and reliable methods to measure the distance between nuclei.[22,29] It can provide the interatomic distance between a pair of nuclei up to an accuracy of 0.1 Å. Typically, it consists of two parts: S_o and S. Figure 1.9 shows the typical pulse sequence of REDOR. 180° pulses (also called as dephasing pulse) are present in the middle of each rotor cycle on the nuclei I. When the dephasing pulse is off, the sequence gives a full-echo spectrum of S spin (S_o). By flipping the spin population on nuclei I, the 180° dephasing pulse will re-introduce the dipolar coupling and decrease the intensity of the signal to S ($\Delta S = S_o - S$). The internuclear distance can be obtained by plotting the $\Delta S/S_o$ versus the dephasing time.

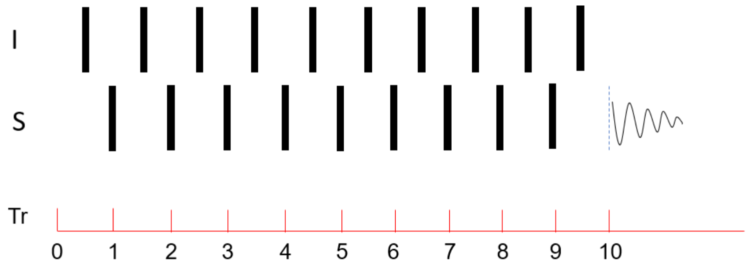

Figure 1.9 Schematic of the pulse sequence for REDOR. The number in the axis is the number of spin rotor cycles. In the schematic, it is a $10T_r$ evolution time for REDOR. T_r is one spin rotor time.

The heteronuclear dipolar Hamiltonian can be expressed in the following equations (from 1.24 to 1.25):

$$\hat{\mathrm{H}}_{IS} = 2\omega_D I_Z S_Z \tag{1.24}$$

$$\omega_D = \frac{1}{2} D(1 - 3cos^2\theta) \tag{1.25}$$

When the sample is spinning at magic angle in the magnetic field, we can substitute equation 1.19 for equation 1.25 and will get the time-dependent ω_D (equation 1.26):

$$\omega_D = -\frac{1}{2} D[sin^2\beta cos2(\alpha + \omega_r t) - \sqrt{2} sin2\beta \cos(\alpha + \omega_\gamma t)] \tag{1.26}$$

The dipolar coupling Hamiltonian in one rotor spin cycle is averaged out by magic angle spinning and is proved by the following equation 1.27 and 1.28:

$$\overline{H} = \frac{1}{T_r} \int_0^{T_r} H_{IS}(t)dt = \frac{2}{T_r} I_Z S_Z \int_0^{T_r} \omega_D(t)dt = 2\overline{\omega}_D I_Z S_Z \tag{1.27}$$

$$\overline{\omega}_D = \frac{1}{T_r} \int_0^{T_r} \omega_D(t)dt = -\frac{D}{2T_r} \left[\frac{sin^2\beta cos2(\alpha+\omega_r t)}{2\omega_r} - \frac{\sqrt{2} sin2\beta \cos(\alpha+\omega_r t)}{\omega_r}\right] \Big|_0^{T_r} = 0 \tag{1.28}$$

As a result, we can find that the average dipolar Hamiltonian during one complete rotor cycle is 0, which implies there is no dipolar evolution. On the contrary, when the dephasing pulse is on and in the center of one rotor cycle ($\frac{1}{2} T_r$), the average dipolar Hamiltonian is non-zero and can be proved by equations 1.29:

$$\overline{\omega}_D = \frac{1}{T_r} [\int_0^{\frac{T_r}{2}} \omega_D(t)dt - \int_{\frac{T_r}{2}}^{T_r} \omega_D(t)dt] \tag{1.29}$$

The negative sign in front of the second term in equation 1.29 arises from the I-spin π pulse,[30] which flipped the net magnetization of the nuclei I and the sign of the interaction. The average dipolar coupling in one rotor spin cycle will be as equation 1.30:

$$\bar{\omega}_D = -\frac{\sqrt{2}D}{\pi} sin2\beta sin\alpha \tag{1.30}$$

The dephased signal (S) in one rotor spin cycle with dephasing pulse can then be simplified into equation 1.31:[29]

$$S = S_o cos\bar{\omega}_D T_r \tag{1.31}$$

where S_o is the signal without dephasing pulse. A powder sum over the angles α and β provides the normalized dipolar dephased intensity ratio S/S_o. The results for several rotor spin cycles (N) are shown as equation 1.32:[22]

$$\frac{S}{S_o} = \frac{1}{4\pi}\int_0^{2\pi}\left(\int_0^{\pi}\cos(NT_r\bar{\omega}_D) sin\beta d\beta\right)d\alpha = \frac{\sqrt{2}\pi}{4} J_{1/4}\left(\sqrt{2}NT_rD\right)J_{-1/4}\left(\sqrt{2}NT_rD\right) \tag{1.32}$$

where J is the Bessel function of the first kind; D is in the unit of Hertz; N is the number of spin rotor cycles. Because the dephased REDOR signal ratio is only related to the evolution time NT_r and dipolar coupling strength (D), a plot of REDOR dephasing curve with evolution time NT_r can be fitted to equation 1.36 to extract the internuclear distance between I and S.

1.4 NMR Crystallography

NMR crystallography combines NMR, X-ray diffraction (XRD) and computational chemistry [31–38] to resolve atomic positions within crystals. A strength of this scheme is using NMR chemical shifts and dipolar couplings between nuclei to validate *ab inito* quantum calculations for refining atom positions that are (in some cases) invisible to XRD.[39–41]

Structural analysis of crystalline materials generally employs XRD to determine atomic coordinates of crystal structures,[42,43] which is unparalleled in determining long-range crystalline order.[44] In comparison, NMR spectroscopy excels at determining local site symmetry.[45] XRD suffers, however, from being insensitive to low atomic number (Z) nuclei, such as hydrogen; hence, in some cases, the structural models produced by XRD are not sufficiently accurate for understanding how the resulting chemistry is directed by coordination.[46] Creative efforts in the emerging field of "NMR crystallography" [47–51] have pushed the use of NMR as a complementary tool for elucidation of precise atomic coordinates, especially protons, in the unit cell.

Generally, isotropic chemical shifts (δ_{iso}) are used to identify spin-1/2 (nuclear spin, I=1/2) NMR active species in structures, because they are the most readily observed in NMR spectra. However, the use of these δ_{iso} values alone disregards the precision that is afforded when the full CSA tensor is determined. These tensors sensitively reflect the local electronic environment surrounding the nucleus being probed, including small perturbations by the NMR-active species in the vicinity. Getting accurate CSA information, therefore, increases the precision of the structural model being determined. It is worthwhile to note, that while δ_{iso} values are used ubiquitously by the NMR community, they have two limitations. For instance, to acquire high resolution ^{1}H NMR of solids requires very fast spinning rates (80 kHz, or higher) to average out the network of strong dipolar couplings among protons. In addition, under high spinning rates, structurally informative interactions of chemical shift anisotropy and first-order quadrupolar couplings are averaged.[52] All these interactions contain detailed information about the three-dimensional shape and chemical bonding network.

Atomic positions can be optimized with computational chemistry, such as density functional theory (DFT),[53,54] and these calculations can be validated by comparison with experimental data.[55,56] Facelli and Grant gave an early demonstration that the combination of calculated *ab initio* chemical shift tensors and experimentally measured ^{13}C chemical shift tensors can be used together to provide structural models.[57]

DFT is widely used to study structure, bonding and properties of solids.[58] DFT calculations based on generalized-gradient approximation (GGA)[59] exchange-correlation functionals have been widely applied and demonstrated to yield high accuracy for a wide variety of materials systems, displaying a range of bonding types.[60,61] However, these semi-local functionals are known to not describe weak bonding interactions well, including in particular dispersion forces. Several "van der Waals" corrected approaches have been developed to better describe such non-bonded interactions within DFT. [62–64] It can be expected that hydrated carbonate minerals provide an interesting test case for such approaches, since they feature a variety of chemical bonding environments, spanning strong covalent and ionic interactions to weaker interatomic forces including hydrogen-bonding and dispersion. In this thesis, we will illustrate the influence of different functionals on the calculation of NMR tensors, and are evaluated by comparison to experimental CSA tensors.

1.5 Conclusions

The following chapters will discuss the use of SSNMR to study the CO_2 mineralization process and products. The samples studied here are either crystalline or amorphous. In chapters 2 and 3, I will show the results of in-situ SSNMR of CO_2 mineralization. These chapters include ^{13}C and

^{29}Si NMR to investigate the formation of products, and changes to starting materials. In chapters 4 and 5, I applied NMR crystallography to investigate the structure of CO_2 mineralization products—hydromagnesite and nesquehonite. NMR crystallography will provide a foundation for understanding CO_2 mineralization mechanisms and products.

Chapter 2: NMR Study of Magnesium Carbonate Formation Through In-Situ Solid-State NMR

The material in this chapter is adapted with permission from Rachel K. Wells, Wei Xiong, Erika Sesti, Jinlei Cui, Daniel Giammar, Philip Skener, Sophia E. Hayes, Mark S. Conradi, Geochimica et Cosmochimica Acta, 2017. 204, 252 and Erika L. Sesti, Jinlei Cui, Sophia E. Hayes, Mark S. Conradi, Journal of Magnetic Resonance, 2017, 282, 136. Copyright 2017 Geochimica et Cosmochimica Acta and Journal of Magnetic Resonance.

2.1 Introduction

Forsterite (Mg_2SiO_4) is a reactive mineral envisioned for carbonate mineral formation with dissolution-precipitation reactions. Forsterite is the pure Mg end member of olivine ($(Mg, Fe)_2SiO_4$), and commonly found in basalts and peridotites, which are formations envisioned for geologic carbon sequestration applications. This mineral has been frequently studied in term of its reactions with CO_2.[65] Research has been conducted at elevated temperature and pressure to mimic GCS conditions. Such elevated temperature and pressure reactions are also studied in saline aquifers in the presence of forsterite or olivine using injected CO_2.

Lackner et al. were perhaps the first to suggest forsterite carbonation for CO_2 mineralization.[66] Mineralization is based on dissolution-precipitation reactions and can be explained by the following coupled chemical equations.[67]

$$CO_{2(g)} \leftrightarrow CO_{2(aq)} \tag{1}$$

$$CO_{2(aq)} + H_2O \leftrightarrow HCO_3^- + H^+ \leftrightarrow CO_3^{2-} + 2\ H^+ \tag{2}$$

$$Mg_2SiO_{4(s)} + 4H^+ \leftrightarrow 2Mg^{2+} + H_4SiO_4 \tag{3}$$

$$Mg^{2+} + CO_3^{2-} \leftrightarrow MgCO_{3(s)} \tag{4}$$

$$H_4SiO_4 \leftrightarrow SiO_{2(s)} + 2H_2O \tag{5}$$

Hanchen et al. demonstrated that forsterite dissolution is the first rate-limiting step, and magnesite ($MgCO_3$) precipitation is the second rate-limiting step in the overall process of carbonation of olivine.[68] There are multiple factors which can affect the dissolution processes, such as temperature, pH, and CO_2 concentration.

This study is focused on the spatial and geochemical interaction between forsterite and CO_2-rich fluids, and there are two objectives. First, this study is to observe the precipitation growth through time, characterize the composition of the precipitates, and determine their spatial distribution in the samples in a batch reaction. We reacted sintered forsterite cylinders in water at 100°C equilibrated with 100 bar (the pressure about 1 km depth underground) CO_2 for up to 52 days. Post-reaction samples were characterized using optical and electron microscopy, and ex-situ SSNMR spectroscopy. Second, in CO_2 sequestration, CO_2 gas is pumped into underground geological formations, especially aquifers and understanding how this flow of CO_2-loaded fluid affects mineralization is essential. Characterizing the flow of CO_2-rich fluids in reactive geological storage "reservoirs" is vital for understanding the details of the dissolution of minerals and precipitation of carbonates. Therefore, a flow-through elevated-temperature and -pressure NMR apparatus was built to monitor CO_2 reactions with forsterite.

2.2 Experimental methods

2.2.1 Probe Design for In-Situ Solid-State NMR in Batch Reactions

This section describes the probe designed and built by Andy Surface.[69] The NMR coil in probe is a tank circuit with an Alderman-Grant design,[70] which is tuned to 89.07 MHz for ^{13}C in an 8.3 T magnetic field by two non-magnetic 0.8-10 pF variable Polyflon capacitors. The coil has a 0.7-inch inner diameter and 1-inch in length.

The high-pressure reaction vessel is made of yttria-stabilized zirconia called AmZirOx 86 (sold by AstroMet Inc. Cincinnati, Ohio). It consists of 95% zirconia and 5% yttria, and can withstand 400°C temperature and 400 bar pressure. The reaction vessel has a lot of advantages: non-conductive, high-tensile strength, containing no carbon, unreactive to most chemicals, impermeable to gas, and 0% water retention. The NMR coil is set to ½ inch above the bottom of the reaction vessel to reduce susceptibility inhomogeneity caused by position at the bottom of the tube within the ‘fixing range’ of shims. The temperature in the probe is monitored via two Type K thermocouples. One is in the heated zone of the probe to the monitor temperature in the reaction vessel. Another one is near the variable tuning capacitor to monitor the temperature of the NMR circuitry in the cooling region of the probe. Figure 2.1 shows the details of the in-situ ^{13}C NMR probe and the high-pressure zirconia reaction vessel.

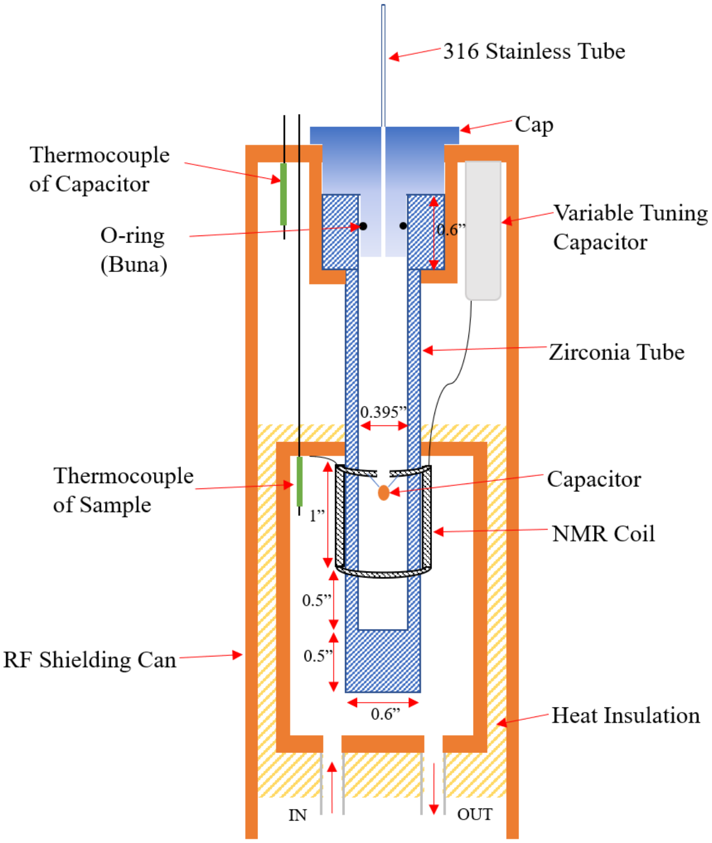

Figure 2.1 The elevated pressure, elevated temperature NMR probe, including a zirconia reaction vessel, NMR coil, heat box, capacitors and thermocouples

The high-pressure tubing and associated valves, capacitor tuning rods, thermocouple wires, RF cables and cooling tubes enter from the top of the probe. The heating tube and vent tube enter from the bottom of the probe. Heating is accomplished by flowing heated air from the pipe to heated region. Cool air is blown over temperature-sensitive variable tuning capacitors and protects them against damage from overheating (The maximum operating temperature of capacitors is 125°C). The pressure in the zirconia tube is monitored via an MSP-300 pressure transducer (Measurement Specialties Inc.). The high pressure of $^{13}CO_2$ is created by cryogenic pressurization. A recollection vessel is submerged in liquid nitrogen (LN_2) to freeze $CO_{2(g)}$ from a CO_2 source. When the recollection vessel is closed, a hand-held hair dryer is used to heat it and build high pressure in the vessel before opening the valve to the probe. Figure 2.2 displays the sketch of the in-situ NMR probe with the high pressure $^{13}CO_2$ manifold. More details about the coil design and gas manifold can be found in a previous publication.[14,69]

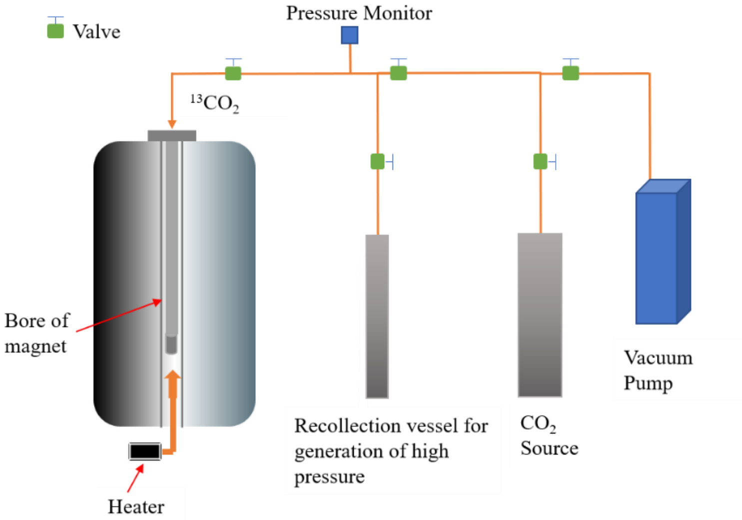

Figure 2.2 Schematic of the in-situ NMR probe with the high-pressure $^{13}CO_2$ manifold

2.2.2 Probe Design for Flow-Through NMR Apparatus

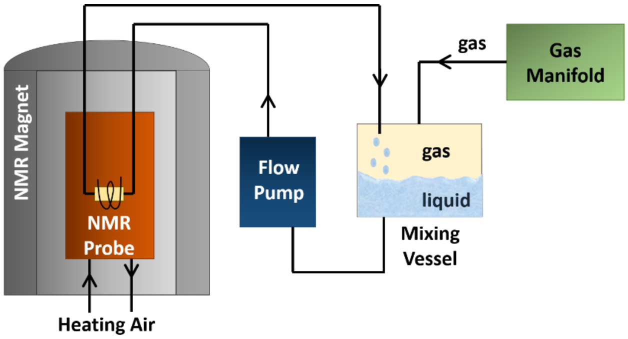

Figure 2.3. Schematic of the flow-through, elevated temperature and pressure NMR apparatus.

The flow-through, elevated pressure and temperature NMR apparatus consists of four main interconnected parts: a gas manifold, a gas and solution mixing vessel, a flow pump, and an NMR probe capable of elevated temperature and pressure.[71] It was designed and built by Prof. Mark Conradi and Dr. Erika Sesti. The schematic of the flow-through NMR apparatus is shown in Figure 2.3. All components are connected through 1/16'' OD 316 stainless steel tube (High-Pressure Equipment Company), selected because it is much more resistant to corrosion from the CO_2-infused solutions (i.e., acidic conditions) than other types of steel.

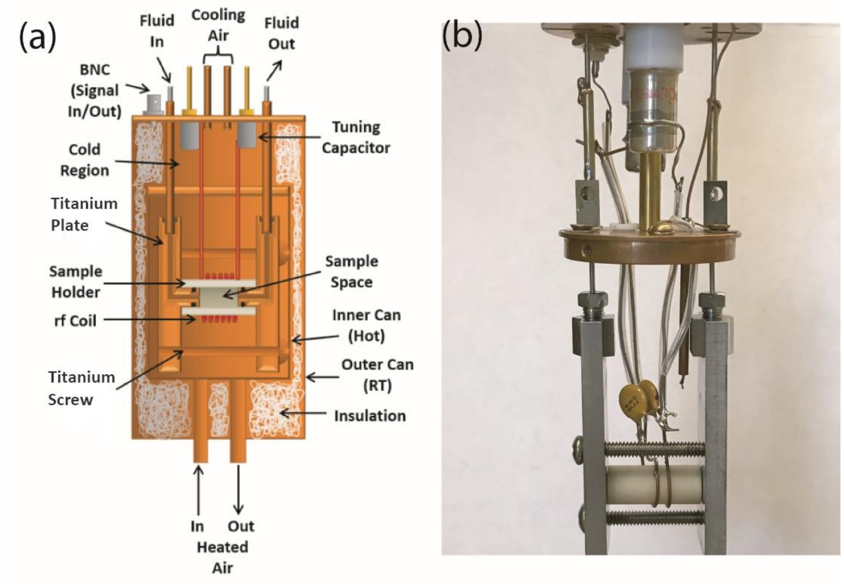

Figure 2.4. Schematic (left) and photo (right) of the elevated pressure and temperature, flow-through NMR probe. The schematic shows the coil region and the high-pressure reaction vessel, minus the copper "can" probe head caps that contain the heated air (the inner cap), and the insulation (the outer cap). Some of the hardware shown in the photo includes fixed capacitors (yellow disks), not shown in the schematic.

The schematic and photo of the NMR probe are shown in Figure 2.4. The single-channel, elevated temperature and pressure NMR probe is "home built" and capable of observing liquids, gases, supercritical fluids and solids. The sample holder is fabricated from zirconia. The NMR electronics are comprised of a tuned circuit and a radio-frequency (RF) solenoid coil, which is tuned to 89.07 MHz for ^{13}C in an 8.3 Tesla magnetic field. Tuning of the probe is accomplished by two non-magnetic 5-25 pF variable capacitors (Polyflon), which have a maximum working voltage of 3 KV and maximum operating temperature of 125°C.

The high-pressure reaction vessel within the coil region has a 1.2 cm outer diameter and 0.66 cm inner diameter. To maintain the high-pressure environment, we used two titanium alloy (6Al-4V) plates on either end held together with two titanium alloy screws. A machined fitting (AF1, High-Pressure Equipment Co.) was used to join the 1/16” 316 stainless steel tube to each of the titanium plates. The assembly can withstand 400 bar of pressure and is rated to 400 °C. The NMR coil is a 2-turn coil, which can form a low-inductance/high capacitance tuned circuit. The design of temperature control and cooling air is similar to the static probe.

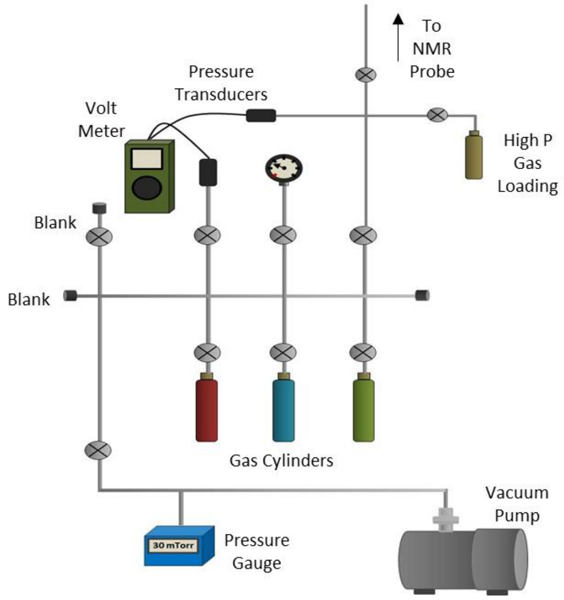

Figure 2.5. Schematic of the gas manifold.

The gas manifold for the flow probe was assembled using commercial components for delivering CO_2 to the mixing vessel, and is shown schematically in Figure 2.5. The “High-P (pressure) Gas Loading” vessel is designed to be submerged in liquid nitrogen to freeze $CO_{2(g)}$ from the manifold at the pressure of a conventional (medium pressure) gas cylinder, as seen on the schematic of the gas manifold. An MSP-300 pressure transducer (Measurement Specialties Inc., 0-172 bar, 1-5 V), is used to monitor the pressure in the system electronically, while multiple additional mechanical pressure gauges are installed at the indicated points for watching various portions of the manifold pressure independently.

A gas-liquid mixing vessel was fabricated to provide a reservoir for mixing liquids and gases at elevated pressures. The schematic of the mixing vessel is displayed in Figure 2.6. The vessel has a 10 mL volume and capitalizes on a large diameter that permits a high surface area between liquid and gas layers. This aspect helps to reach equilibrium quickly between these two phases. The heater in the base of the mixing vessel is used to maintain the partial pressure of $^{13}CO_2$ in the liquid phase, since the temperature in the circulating line should be same as that of the reaction vessel as much as possible. For avoiding corrosion by these acidic solutions, the base and O-ring-sealed cap are made of the titanium alloy (6Al-4V). There are two ports on the top cap: one is for the introduction of gas into the vessel, and the other is for returning solution to the mixing vessel after passing through the NMR probe. Two ports also exist on the base: one comes from the bottom of the vessel and is connected to the flow pump. Another side port on the wall is used as a solution level indicator. Temperature regulation is carried out through a cartridge heater (Omega) in the base of the vessel, which is controlled by a temperature controller.

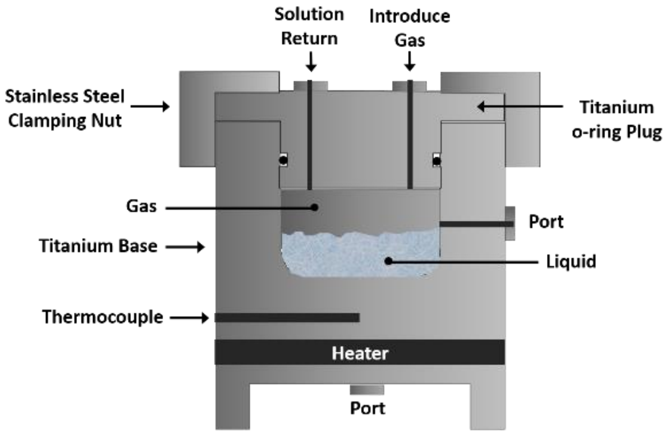

Figure 2.6. Schematic of the titanium mixing vessel.

The flow pump is an HPLC-style pump (Waters 6000). The pump has an operating pressure range of 0-414 bar and a flow rate range from 0.1 to 9.9 ml/min with variability of 0.1 ml/min increments. The solution enters the pump from the base of the mixing vessel, and goes into the sample space of the NMR probe, notably outfitted so that this can be accomplished while the probe is inside the magnet.

2.2.3 Synthesis of Starting Materials

All experimental samples were synthesized by our collaborator, Dr. Rachel Wells (Department of Earth & Planetary Sciences, WUSTL). The samples were prepared from pure synthetic forsterite powders (Fo_{100}) (Mg_2SiO_4; 99 % purity; Alfa Aesar), which was sieved to yield particles smaller than 44 μm. The pure forsterite was chosen to avoid the interference between paramagnetic iron and collection of NMR spectra. The powders were pressed and vacuum-sintered following established procedures.[72]

For the batch reaction, the cylindrical pellet was made with a 13 mm diameter die mold (3.7 mm length). The pellet was then vacuum-sintered at 1300°C for 48 h at a pressure of less than 10^{-5} Torr. Under these conditions, no evidence of grain growth was observed. After that, the sample was cut in half along the diameter, yielding two semi-circular “half” cylinders (6.5 mm width for each pellet).

For the flow-through reaction, the sample was also prepared with the same procedure as described previously. The compressed pellet was cut in half, and one side was milled. Finally, a pure forsterite monolithic sample with a 2 mm thick fracture was prepared. The information of samples and pressure/temperature conditions for the reaction are summarized in Table 2.1.

Table 2.1 Samples for in-situ SSNMR in batch and flow-through reaction

Experiments	Sample ID	Geometry	Width, Length (mm)	Temperature (°C)	Starting Pressure (bar)	Final Pressure (bar)	Flow Rate (ml/min)	Reaction Time (days)
1 (batch)	Fo_{100}_f	Cylinder with saw cut	6.5, 3.7	100	100	100	--	53
2 (flow)	Fo_{100}_fr	Cylinder with fracture	4, 13, 0.2	100	100	100	0.1	38

2.2.4 In-Situ Solid-State ^{13}C NMR Experiment

For batch reaction: elevated pressure ^{13}C-enriched CO_2 gas (99% purity from Sigma Aldrich) was loaded into a small volume vessel attached to the manifold, and then released into the probe. Fo_{100}_f cylinders were submerged in 2 mL of ultrapure water (resistivity >18.2 MΩ) and then heated to a constant temperature of 100 °C. Fo_{100}_f cylinder was cut in half, and each side was placed side-by-side to simulate a fracture. The sample was placed freestanding on a spacer. The pressure was observed to be stable within 1 hr at 100 bar. The sample was monitored throughout 53 days, and the pressure was kept at 100 bar. At the end of the experiment, the vessel was cooled to room temperature over 1–2 hr, and any remaining enriched $^{13}CO_{2(g)}$ was collected. For this sample (Fo_{100}_f), ^{13}C NMR experiments were conducted at a Larmor frequency of 89.07 MHz with no ^{1}H decoupling. For in-situ static ^{13}C NMR experiment, the Hahn echo NMR pulse sequence with a $\pi/2$ pulse of 16.85 μs, a π pulse of 33.7 μs, and a τ delay of 130 μs were used. The recycle delay was 30 s, and the number of transients recorded was 1440. The spectra were referenced using the $^{13}CO_{2(g)}$ peak at 128.6 ppm for these experimental conditions.[69]

For flow-through reaction: the forsterite monolithic sample (Fo_{100}_fr) was reacted within the zirconia reaction vessel in situ, in the flow-through NMR probe. The fractured piece was submerged in a solution of water (resistivity >18.2 MΩ), and the reaction was kept at a pressure of 100 bar and a temperature of 100°C. $^{13}CO_2$ was refilled during the experiment to keep the pressure constant. The reaction was finished after 38 days since no significant growth of solid carbonate signal was observed. In-situ static ^{13}C NMR spectra were recorded with a ^{13}C Hahn echo pulse sequence at a Larmor frequency of 89.07 MHZ. Typical conditions utilized $\pi/2$ pulses of 7 μs and π pulses of 14μs, with a τ delay value of 130 μs. 1024 transients were recorded for each time point, with a recycle delay (between transients) of 60 s. Schematic of the batch and flow-through reaction with samples are shown in Figure 2.7.

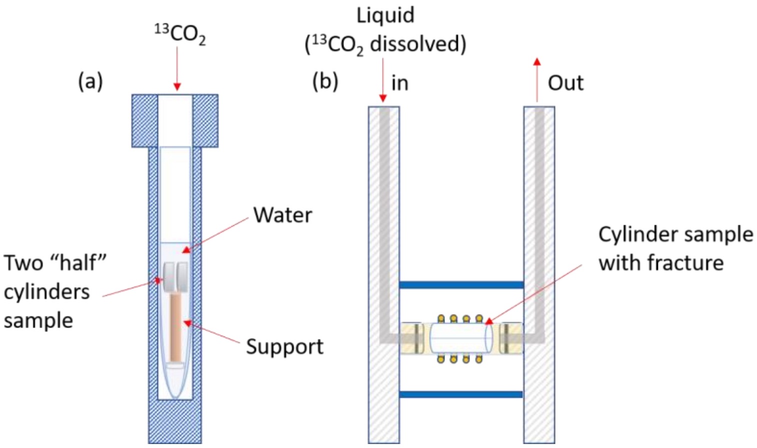

Figure 2.7. Schematic of forsterite cylinder with $^{13}CO_2$ inside (a) static batch probe and (b) flow-through probe.

2.2.5 Ex-Situ Solid-State ^{13}C NMR Experiment

For the batch reaction: ex-situ $^{13}C\{^1H\}$ MAS and static $^{13}C\{^1H\}$ NMR spectra were acquired on a Chemagnetics 4 mm MAS triple resonance probe using a Larmor frequency of 74.18 MHz. ^{13}C static and MAS experiments were conducted using a Hahn echo sequence with $\pi/2$ pulses of 4.23

μs, π pulses of 8.46 μs, a rotor-synchronized τ delay of 193.65 μs and a recycle delay of 30s. 1440 transients were acquired for the static experiments, and 256 scans were recorded for the MAS spectra.

For flow reaction: ex-situ static $^{13}C\{^{1}H\}$ and ^{13}C MAS NMR were also performed on the 7 T magnet with same equipment using a Larmor frequency of 74.18 MHz. The static ^{13}C experiment was conducted using a Hahn echo sequence with π/2 pulses of 3.5 μs, π pulses of 7 μs, and a τ delay of 30 μs. The data were acquired with 1440 transients with a 60 s recycle delay. ^{13}C MAS NMR was performed with π/2 pulses of 3.5 μs with 64 transients using a 60 s recycle delay.

The ^{1}H decoupling strength for all experiments was 58.8 kHz at a ^{1}H Larmor frequency of 294.97 MHz. The spinning frequency for MAS experiments were 5 kHz. All spectra were referenced to adamantane at 38.48 ppm.

2.2.6 Microscopy of Reacted Sample

The reacted Fo100_f was cut in half horizontally and the lower part was analyzed by electron microscopy (JEOL 7001LVF FE-SEM; FEI Nova 230, studied by our collaborator, Dr. Rachel Wells). Backscatter electron (BSE) and secondary electron (SE) imaging were used to document microstructures.

2.3 Results and Discussion

2.3.1 Fractured Cylinder Experiment

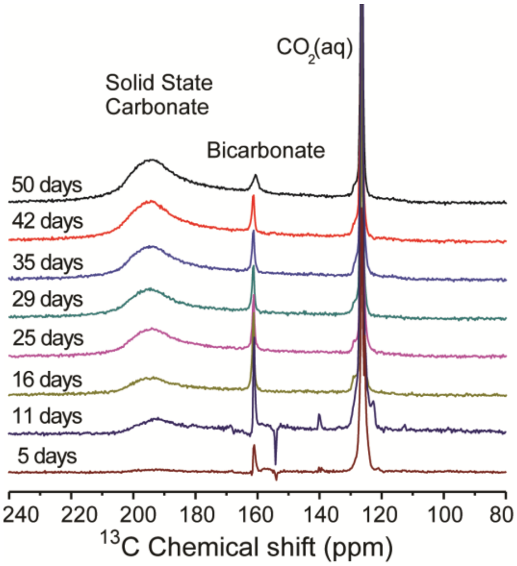

Figure 2.8 In-situ static ^{13}C NMR spectra of sample Fo$_{100}$_f at different reaction times, held at 100 °C and 100 atm ($^{13}CO_2$ pressure). A broad resonance consistent with solid-state carbonate formation (most evident peaked around 195 ppm) grows in over time. Other resonances are $HCO_3^-{}_{(aq)}$ and $CO_{2(aq)}$.

As the cut Fo$_{100}$ cylinder (Fo$_{100}$_f) was reacted within the in-situ ^{13}C NMR batch probe, we observed the growth of the carbonate mineral resonance as a function of time (Figure 2.8). A small broad resonance became evident (around 195 ppm) after 5 days, and this feature is indicative of a CSA lineshape that becomes increasingly intense over time. Throughout the reaction, an axially-symmetric carbonate CSA powder pattern became more apparent. Change in the solution-state bicarbonate resonance (at 161 ppm) was observed, which indicates that the pH of system changes. At the beginning of experiment, CO_2(g) is dissolved into the water and converts to bicarbonate which increases initially (from 5 days to 11 days). After 16 days, the increasing signal of solid phase carbonate was observed, which is due to conversion from carbonate/bicarbonate ions in the solution. Therefore, the bicarbonate signal decreases after 16 days. Note: there was some small instrumental noise or artifacts in the 5- and 11-days spectra that were not present in other experiments. Those unassigned peaks are not genuine signals.

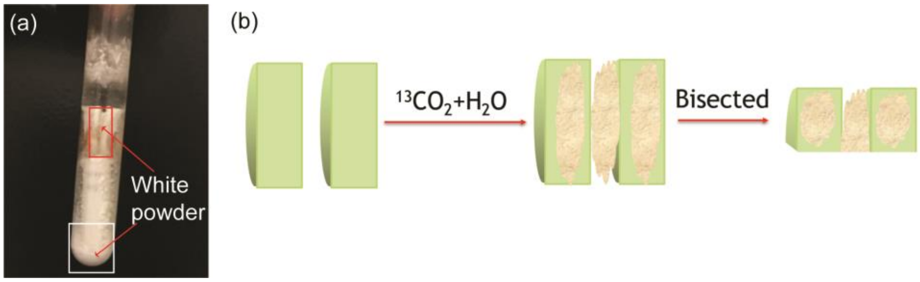

Figure 2.9 (a) Pictures of the Fo_{100}_f after the reaction. New white precipitation is found between two pellets (red box) and in the bottom of the glass tube (white box). There is a white zirconia spacer between them. (b) Schematic of the cut sample before and after the reaction.

After the reaction, the reaction vessel was taken out. White powder was found between the two semi-circular pellets of Fo_{100}_f and at the bottom of the glass tube, which is shown in the photo of Figure 2.9a. The reacted sample was bisected in half, as shown in Figure 2.9b. Ex-situ NMR analyzed the top half, and the lower half was tested through electron microscopy; photos of the reacted sample are shown in Figure 2.10. All sides of the Fo_{100}_f sample are coated in precipitates that are easily observed in optical microscopy, as shown in Figure 2.10a and b. The vertical sides and curved underside are covered in a precipitate, which is shown to be magnesite ($MgCO_3$) by ex-situ ^{13}C MAS NMR and will be discussed below. The fine magnesite grains also fill the gap between the two halves of the sample.

Backscatter electron (BSE) pictures of the Fo_{100}_f (lower half after bisection) are shown in Figure 2.10c and d. Within one side of the fractured Fo_{100}_f cylinder, we observe a transition from a magnesite-rich area (gray particles outside the sample) to an amorphous silica-rich area (dark coat) that is oriented approximately parallel to the edge of sample (Figure 2.10c). Magnesite forms an intergranular cement around the host forsterite grains, only rarely as cement near amorphous silica, and is more common on the edge of the sample (Figure 2.10c). The amorphous silica is present in a thick layer (200 um) on the fracture side (Figure 2.10c). Moving further from the surface of sample, the homogeneous amorphous silica layer translates into a mix of amorphous silica with Fo_{100} centers (Figure 2.10d). The larger grains as a light particle on the edge of the forsterite are primarily Zn-carbonates (Figure 2.10c). The zinc comes from the unintentional dissolution of a brass piece of the probe located near the inlet of the NMR reactor.

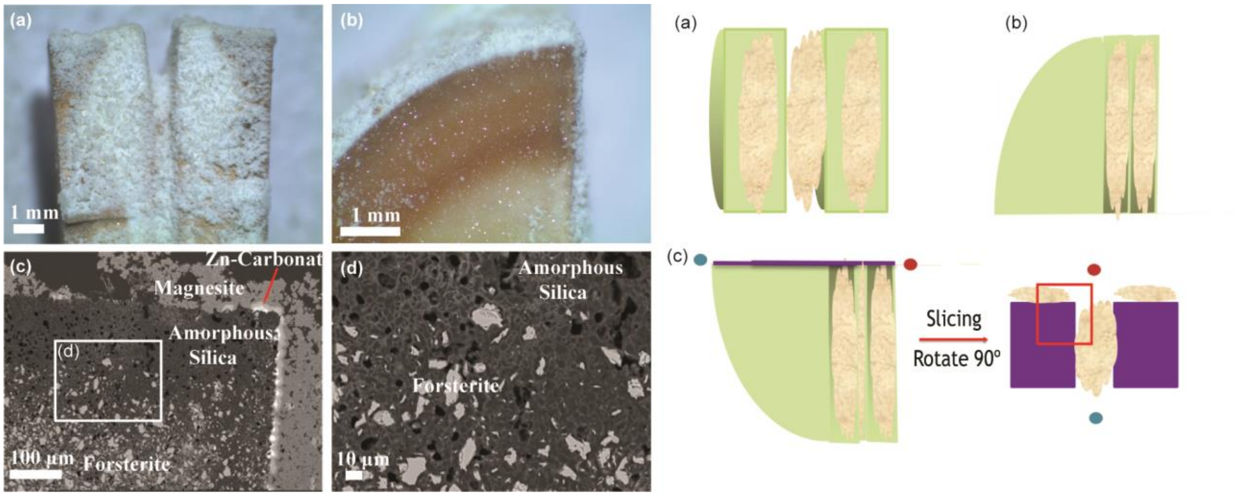

Figure 2.10 Optical photomicrograph of (a) the sample Fo100_f after reaction and (b) cross-section after cutting. The BSE images of (c) the edge of the Fo_{100}_f and (d) the area that Fo_{100} observed inside amorphous silica. Cartoon schematic for photo (a)-(c) of sample is shown in the right.

In CO_2 sequestration, any structural heterogeneity (e.g., intergranular and interconnected porosity, fractures) of the host material may also, over time, contribute to the complexity of the texture. Preexisting pores and fractures, and the interconnection between these spaces create zones for diffusive transport of solutes, which result in areas more favorable for magnesite precipitation. In experiments where there are no limited diffusion zones and the surface area-to-volume ratio is low,[67,73] the time needed to reach supersaturation is slow, compared to samples where these zones or high surface area-to-volume ratios are present. In the reaction of Fo_{100}_f with $^{13}CO_2$, the high surface-to-volume ratio in the zone between two pellets will help to precipitate magnesite.

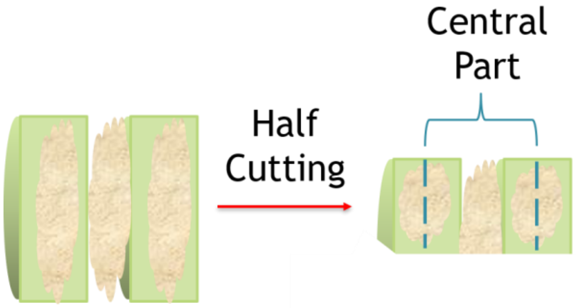

Figure 2.11 Schematic of cutting of the sample after reaction (Fo_{100}_f)

The top part of the reacted sample was split into three sections as shown in Figure 2.11. Ex-situ $^{13}C\{^1H\}$ NMR of the central part in Fo_{100}_f after the reaction is shown in Figure 2.12. $^{13}C\{^1H\}$ MAS NMR of the central part in Fo_{100}_f shows a single ^{13}C isotropic peak at 169.5 ppm under MAS (figure 2.12b). This peak is assigned to magnesite ($MgCO_3$). The unique resonance means there was no detectable formation of other solid carbonates, such as hydromagnesite or nesquehonite. Static ^{13}C NMR powder pattern for the central part of the sample is shown in Figure 2.12a, which is deconvoluted in Dmfit (red curve). The lineshape has a η_{CSA} value of 0.32, δ_{aniso} value of -57.6 ppm and is centered at δ_{iso} = 169.5 ppm. The near-axially symmetry powder pattern (Figure 2.12a), is similar to what has been assigned as magnesite (η_{CSA} = 0.14, δ_{aniso} = -54.5 ppm) previously.

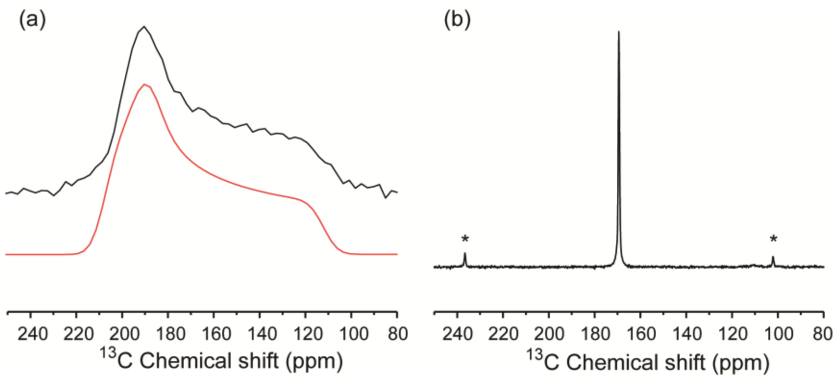

Figure 2.12 Ex-situ $^{13}C\{^{1}H\}$ NMR of the central part of reacted Fo_{100}_f sample are shown in (a) static ^{13}C (with ^{1}H decoupling) lineshape, experimental data is shown in black and simulation by Dmfit is shown in red. and (b) $^{13}C\{^{1}H\}$ MAS spectrum. * indicates the spinning sidebands.

Ex-situ $^{13}C\{^{1}H\}$ NMR analysis of the powder in the bottom of the glass tube is shown in Figure 2.13. The ^{13}C MAS spectrum was collected on this sample, and the 169.5 ppm isotropic resonance was found, consistent with $MgCO_3$ (Figure 2.13b). The single resonance also suggests that there is only one carbon site, similar to what was found from the central part of the reacted sample. Static ^{13}C NMR spectra is exhibited in Figure 2.13a with Dmift deconvolution. The model gives an η_{CSA} value of 0.33 and δ_{aniso} value of -56.6 ppm, centered at δ_{iso} = 169.5 ppm. The agreement of ex-situ ^{13}C NMR between the middle of the reacted sample and powders in the bottom of the glass tube indates there is no obvious differences between them.

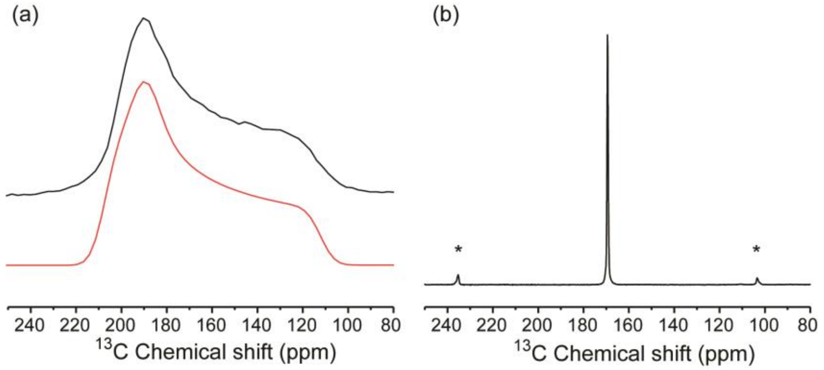

Figure 2.13 Ex-situ $^{13}C\{^{1}H\}$ NMR of white powder in the bottom of the glass tube of the reacted Fo_{100}_f sample are shown in (a) static ^{13}C (with ^{1}H decoupling) lineshape, experimental data is shown in black and simulation by Dmfit is shown in red. and (b) $^{13}C\{^{1}H\}$ MAS spectrum. * indicates the spinning sidebands

2.3.2 Fracture Cylinder Sample in Flow-through Experiments

A pure sintered forsterite sample with a 2mm width artificial fracture (with dimensions 4 mm (OD) x 13 mm) was reacted at 100°C and 100 bar $^{13}CO_2$ in ultrapure water within the flow-through NMR probe. The reaction was monitored for more than one month, and the recorded in-situ static ^{13}C NMR spectra are shown in Figure 2.14. Evidence for solid-state carbonate formation (a broad axially-symmetry lineshape with a peak near 195 ppm) was distinguishable as early as 5 hours of reaction, which is more rapid than found in previous batch reaction experiments. The reason for the faster formation of solid-state carbonate signal could be due to the higher surface area-to-volume ratios in the fracture, which can shorten the time to reach supersaturation of Mg^{2+}. In addition to the solid-state carbonate, resonances for solution-phase bicarbonate (at 162 ppm) and dissolved CO_2 (at 125 ppm) are also evident.

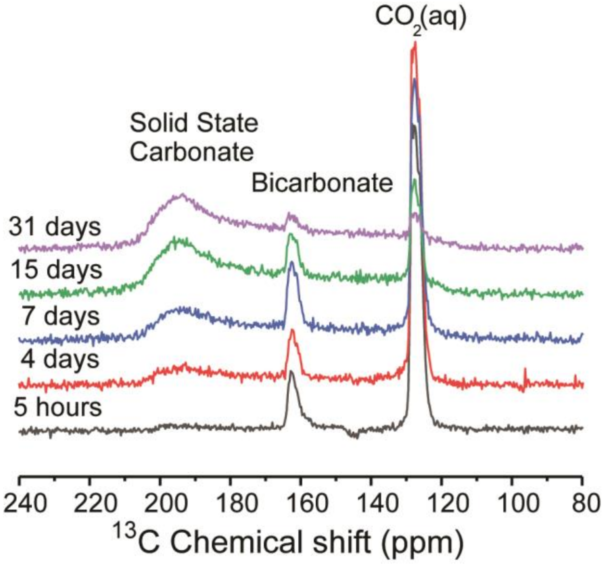

Figure 2.14 In-situ static ^{13}C NMR spectra of Fo_{100}_fr at different reaction times, held at 100 °C and 100 atm ($^{13}CO_2$ pressure). A broad near axially-symmetric resonance consistent with carbonate formation (most evident around 195 ppm) grows in over time. Other resonances are identified, $HCO_3^-{}_{(aq)}$ and $CO_{2(aq)}$.

We also noted that the (dissolved) $^{13}CO_{2(aq)}$ NMR resonance decreased after 10 days in one of the experiments. This find suggests a hardware issue because the $^{13}CO_2$ is always replenished in the mixing vessel of the flow-through probe apparatus. By monitoring the $CO_{2(aq)}$ and bicarbonate resonances, we could determine there was a blockage in the inlet of the pump, and this blockage might have caused the pump to separate the gas inadvertently, leading to less transport of $^{13}CO_{2(aq)}$ through the system. Thus, the faster decay of the bicarbonate may be not entirely due to conversion to solid-state phases.

When the sample was removed from the NMR probe, many translucent particles (around 25 μm) were found inside the fracture of Fo_{100}_fr, which proved to be pure magnesite by Raman spectroscopy and shown in the Figure 2.15b. The euhedral grains of magnesite are similar to what Dr. Xiong Wei has observed in the reaction of fractured olivine with CO_2 in a stirred solution. In their study, the surface in the fracture will reduce the free energy barrier for nucleation, which facilities nucleation rate and growth of crystal.[74] The euhedral grains of magnesite indicate the crystal growth following heterogeneous nucleation.

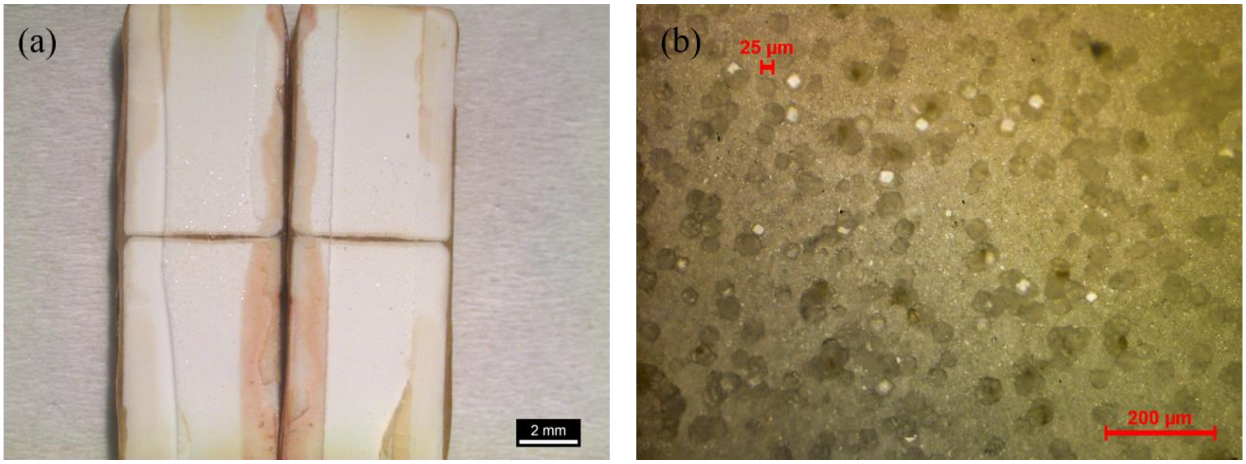

Figure 2.15 (a) Photo of sample Fo_{100}_fr, the forsterite monolith sample after the reaction(38 days) in water and $^{13}CO_2$. (b) Microscope image: solid-state carbonate crystals found on the fracture surface of this forsterite sample.

Ex-situ ^{13}C static and MAS NMR spectroscopy were performed on the reacted forsterite sample after the in-situ experiments (removing the sample at 38 days from the flow probe). The data are depicted in Figure 2.16. One resonance centered at 169.7 ppm is found at ^{13}C MAS NMR and assigned to magnesite ($MgCO_3$). The static ^{13}C NMR also has a characteristic near-axially-symmetry lineshape. The shape and the width are consistent with other reports of magnesium carbonates (Moore et al., 2015), with an η_{CSA} value of 0.22, and δ_{aniso} value of -52.1 ppm.

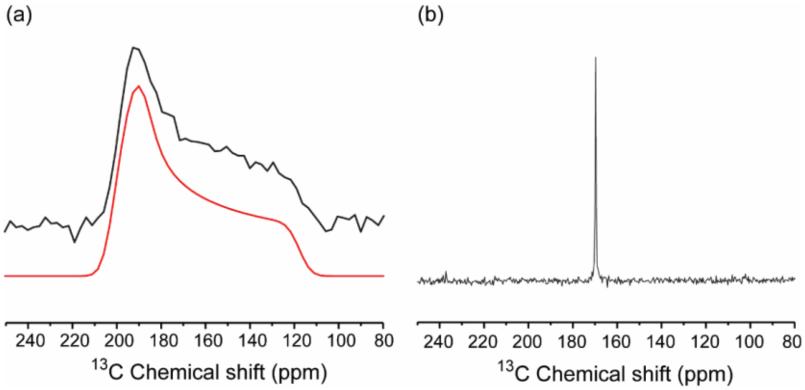

Figure 2.16 Ex-situ ^{13}C{^{1}H} NMR of the reacted Fo_{100}_fr sample are shown in, (a) static ^{13}C (with ^{1}H decoupling) lineshape (experimental data is shown in black and simulation by Dmfit is shown in red). and (b) MAS spectrum.

The results of the batch and flow-solution reactions demonstrated the ability of custom NMR probe. Using the custom probe, we can study the CO_2 mineralization at real time by in-situ ^{13}C NMR without taking out the sample. The final products are magnesite for both reactions under the condition of elevated temperature and pressure.

2.4 Conclusions

In-situ NMR is a useful tool in documenting the formation of bicarbonate and carbonates, which occur within a few days from the start of each experiment at elevated temperature and pressure. Compositional analysis of the reaction products found no other magnesium carbonate phases (e.g., nesquehonite, hydromagnesite) except magnesite ($MgCO_3$) under these high-temperature conditions. At lower temperatures (<100 °C) and pressures, nesquehonite and hydromagnesite are more likely to precipitate than magnesite.[75–77] Xiong and Giammar (2014) documented the occurrence of hydromagnesite within 5 days of reaction using packed forsterite powder beds at 100°C, but hydromagnesite was not observed in those samples reacted for more extended periods.[78] These observations suggest that there might also be a time component to the formation of magnesite, or the dehydration from hydromagnesite to magnesite. All samples within this study were reacted at 100°C, which is more likely for magnesite. All the magnesite as final products display a ^{13}C carbonate lineshape with a mild "axial asymmetry", which could be possible due to the distortion by a fraction of water molecules that are present in the $MgCO_3$ structure. For the reaction of Fo_{100} with $^{13}CO_2$, pre-existing structures (the channel between two pellets in the batch reaction, and the artificial fracture in flow-through reaction) therefore must act as limited diffusion zones for carbonate precipitation. Localized precipitation of magnesite occurred within fractures.

Here, we also reported a new home-built apparatus to conduct in-situ NMR flow experiments at elevated temperatures and pressures. The probe can monitor the reactions of minerals with a $^{13}CO_2$/water solution and the effects of flow on mineralization. In-situ ^{13}C NMR of the reactions of forsterite with $^{13}CO_2$ demonstrates the ability of the flow-through probe for investigating CO_2 sequestration reactions. Compared with the batch reaction, crystalline particles of magnesite with diameters around 25 μm are found inside the fracture.

2.5 Acknowledgements

This material is based upon work supported by the Department of Energy under Award Number DE-FE0023382. This report was prepared as an account of work sponsored by an agency of the United States Government. The in-situ NMR probe for batch reactions was built by Andy Surface. Erika L. The flow-through in-situ NMR probe was built primarily by Erika L. Sesti. We also would like to thank Dan Giammar, Wei Xiong, Phil Skemer, Rachel Wells, and Brian Ellis for valuable discussions about the experimental design and results.

Chapter 3: Evidence from ^{29}Si Solid-State NMR of Dissolution-Precipitation Reactions of Forsterite

The material in this chapter is adapted with permission from Jinlei Cui, Erika Sesti, Jeremy K. More, Daniel Giammar and Sophia E. Hayes, Environmental Engineering Science, 2016, 33. 10. Copyright 2016 Environmental Engineering Science.

3.1 Introduction

The objective of this chapter is to characterize the silicon chemical species present during a reaction of CO_2 with forsterite (Mg_2SiO_4) as well as the solid state carbonate. The solid silica that is formed in CO_2 mineralization is believed to be amorphous,[79] and possibly a gel.[80] The formation of the amorphous silica can be envisioned as the condensation /polymerization and dehydration of the orthosilicic acid, H_4SiO_4. The resulting silica is polymerized on the surface of forsterite when the Mg_2SiO_4 is dissolved[79]. This phenomenon has been observed for forsterite dissolution under conditions with $pH < 9$.[81] In 2011, Daval observed the formation of amorphous silica layers of 15 to 40 nm by TEM, which causes the dissolution rate of olivine to decrease dramatically.[79] In experiments with forsterite dissolution in the presence of high-pressure CO_2, declining dissolution rates could be explained by the changes in surface area and pH with reaction extent, attributable to the possible formation of such a layer.[82] The amorphous silica on the surface is believed to stop the formation of $MgCO_3$,[10] which is an unfavorable situation in conditions where mineralization is desired. However, in the previous chapter, the amorphous silica does not seem to stop the reaction of minerals with $^{13}CO_2$. Thus, we want to use ^{29}Si NMR in this instance (on forsterite) to characterize the silica that is present.

In this chapter, forsterite samples were reacted with $^{13}CO_2$ at elevated temperatures and pressures (to mimic GCS conditions) in both water and brine (dissolved NaCl) as a packed bed, which can be analyzed as a function of depth of the sample. We have been able to detect (semi-quantitatively) with ^{29}Si NMR both the silicate mineral dissolution, as well as the precipitation of amorphous silica as a function of depth in the reacting column. The carbonate precipitate was also monitored as a function of depth by ^{13}C solid-state NMR. We are reporting on NMR conducted “ex-situ”, performed on solids collected from the inner reactor of the in-situ NMR probe but studied by conventional solid-state NMR. In doing so, we can then have the combination of both measurement schemes—comparing results from in-situ studies with higher-resolution spectra from ex-situ MAS solid-state NMR to refine the results from static experiments.

3.2 Experimental methods

3.2.1 Reactions of Forsterite with $^{13}CO_2$ under Elevated Temperature and Pressure

Forsterite (Mg_2SiO_4) powder (Alfa Aesar, Stock # 43807), sample size of 1.902 g, was mixed with 1.138 mL ultrapure water (resistivity 18.2 MΩ-cm) to make a slurry and loaded into the NMR sample space (a cylindrical space 4.3 cm in length and 10 mm in diameter) as reported previously.[15] In reactions with NaCl, a 1.0 M solution (in ultrapure water) was mixed into the forsterite. The sample, a slurry, was pressurized and maintained with a pressure transducer at 100 atm $^{13}CO_2$, (99% ^{13}C-labeled gas, Sigma Aldrich), and the temperature was set to 100°C. After equilibrating at that temperature and pressure for several hours, the reaction was allowed to proceed for 25 days. (The sample that was reacted with the 1.0 M NaCl solution was reacted for 29 days). The solid remaining after the reaction was removed from the liquid, dried, and apportioned into 2 mm-thick disks for (ex-situ) SSNMR analysis of the ^{29}Si species. For example, the sample labeled “2 mm” extends from the top of the sample (0 mm) to a depth of 2 mm below the surface.

Figure 3.1 is a schematic of the sample space in the homebuilt elevated-temperature and -pressure in-situ NMR probe, which can perform with reaction conditions (temperature up to 250°C, pressure up to 300 bar) meant to mimic geological sequestration environments. As shown in the schematic, the packed bed of forsterite was separated into 2 mm-thick samples after reaction, and those analyzed here are at depths (from the top of the reaction bed) of 0 to 2 mm (“2 mm”), 4 to 6 mm (“6 mm”) and 14 to 16 mm (“16 mm”).

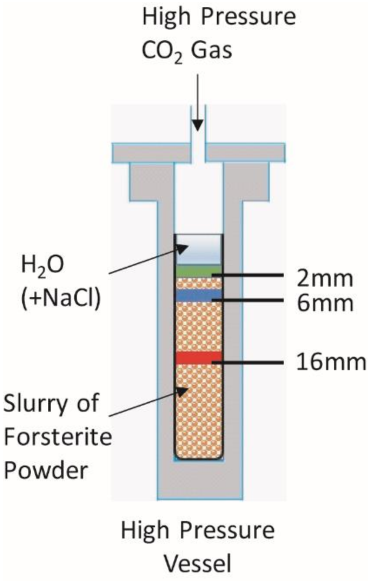

Figure 3.1 Schematic of the in-situ reaction vessel for the forsterite slurry and elevated-pressure $^{13}CO_2$.

3.2.2 ^{29}Si {^{1}H} MAS NMR

Solid-state ^{29}Si{^{1}H} MAS NMR (with proton decoupling) was used to probe the silicon-containing reaction products from the dissolution of forsterite. (The use of proton decoupling was necessary to observe resonances from the amorphous silica that were broadened by nearby protons.) The experiments were performed in a commercial HXY Chemagnetics MAS 4 mm probe on a Tecmag spectrometer at a resonance frequency of 58.6 MHz for ^{29}Si (with 294.97 MHz for ^{1}H decoupling) at 7 T. Magic-angle spinning (MAS) was carried out at a 14 kHz rotation frequency. Typical data acquisition used 4-step phase cycle spin echo experiments with $\pi/2$ pulse lengths of 4.4 μs, a rotor-synchronized τ delay of 136.2 μs, and recycle delays of 390 s, which is approximately 2*T_1 time for forsterite and more than 5*T_1 for amorphous silica (detailed in the section below). The number of transients recorded was 800 per ^{29}Si{^{1}H} spectrum. ^{1}H decoupling was used in the experiments with B_1 field strengths of 18 kHz; in the absence of decoupling, portions of the amorphous silica spectra were obscured by heteronuclear dipolar coupling to nearby protons. The spectra were referenced to tetramethylsilane (TMS) at a ^{29}Si chemical shift of 0.0 ppm.

NMR data integration was completed using the peak fitting software Dmfit. All the peaks were fit using Gaussian functions.

The T_1 spin-lattice relaxation time was measured for 4 of the 6 samples reported here by saturation recovery. The forsterite T_1 for the three samples with the highest signal-to-noise ratios are 136 – 153 s; a fourth sample with a much weaker signal has such a poor signal-to-noise ratio as to undermine the accuracy of the measurement. The amorphous silica all have shorter T_1 times, measured as 19-80 s.

3.2.3 $^{13}C\{^{1}H\}$ MAS Solid-State NMR

The solid-state $^{13}C\{^{1}H\}$ MAS NMR (with proton decoupling) was used to probe magnesium carbonate precipitates from the reaction of forsterite and $^{13}CO_2$. The experiments were performed in a commercial HX Doty 5mm MAS probe on a Tecmag spectrometer at a resonance frequency of 75.4 MHz for ^{13}C (with 299.67 MHz for ^{1}H decoupling). MAS was carried out at a 5 kHz rotation frequency. Typical data acquisition was using 4-step phase one-pulse experiments with $\pi/2$ pulse lengths of 8.8 μs. The T_1 spin-lattice relaxation time is very long, estimated to be (5-20min). Owing to the isotopic ^{13}C enrichment, a single transient was recorded after holding the sample for 45 minutes in the field to allow the sample to magnetize. ^{1}H decoupling was used in the experiments; typical B_1 field strengths of 29.4 kHz were used. The spectra were referenced to adamantane at a ^{13}C chemical shift of 38.48 ppm for the $–CH_2$ resonance.

3.3 Results and Discussion

3.3.1 The Silica-Rich Layer

Figure 3.2 is a diagram of sites typically found in silica and silicates, categorized by the bonding environment of the silicon and labeled by the terms “Q^1, Q^2, Q^3 and Q^4.” Q^4 silicon has 4 Si-O-Si bonds without any protons. A Q^3 site has 3 Si-O-Si bonds and a single Si-OH bond, a Q^2 site has 2 Si-O-Si bonds and 2 Si-OH bonds, and a Q^1 site has just one Si-O-Si and 3 Si-OH bonds. Forsterite has been studied by ^{29}Si NMR previously,[83–85] and the resonance observed at ~-61ppm is representative of SiO_4^{4-} tetrahedra that are interspersed with the Mg^{2+} cations, sometimes referred to as “Q^0” units, following the nomenclature above. It has been well established that the Q^1 to Q^4 sites in amorphous silica may be assigned based on their isotropic chemical shifts, falling into ranges that reflect the presence of protons as well as the O-Si-O bonding angles.[86]

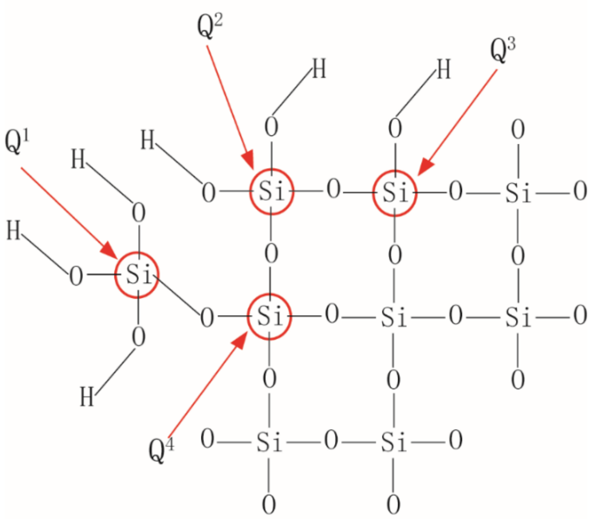

Figure 3.2 A schematic for nomenclature used for the sites present in silica: Q^1, Q^2, Q^3 and Q^4.

However, ^{29}Si SSNMR has a set of experimental challenges that make this isotope less-commonly studied and difficult to quantitative characterization. ^{29}Si experiments are complicated by samples with long T_1 spin-lattice relaxation times, making quantitative characterization very difficult. Also, mineral species such as forsterite (Mg_2SiO_4) and Q^4 sites in amorphous silica both suffer from a lack of protons that can't be exploited for cross-polarization experiments.

3.3.2 T_1 Measurement of Forsterite and Amorphous Silica

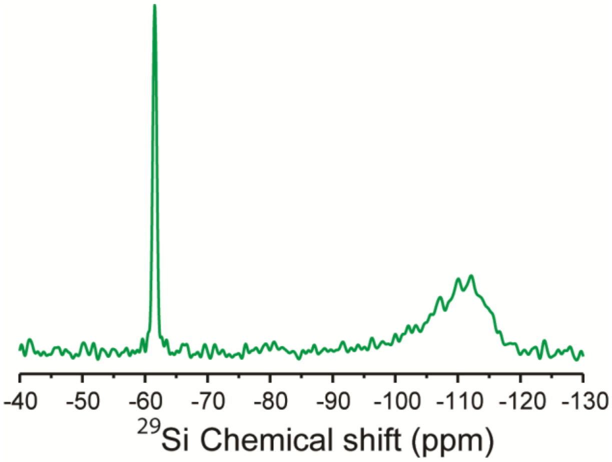

Figure 3.3 ^{29}Si{^{1}H} MAS spectra with ^{1}H decoupling for the forsterite reacted in water at a sample depth of 2 mm.

Figure 3.3 exhibits a ^{29}Si{^{1}H} rotor synchronized spin echo NMR spectrum of the 2 mm slice in the reaction of forsterite with $^{13}CO_2$ with water. There are two resonances present: one is around -61 ppm and assigned to forsterite; another is around -110 ppm and assigned to amorphous silica.

The measurement of ^{29}Si spin-lattice relaxation times (T_1) used the saturation recovery sequence. M is the magnetization at the infinite time (after full relaxation), and M_t is the magnetization at different t (delay times) used in the pulse sequence. It is significant that we have found a better fit to the stretched exponential function for silica (and silicates) as reported by Stebbins and coworkers.[84] Both the exponential growth curves and the semilog (linear) plots were fit using this revised functional form:

$$M_t = M[1 - e^{-(t/T_1)^n}]$$

The stretched exponent was fit with a fixed value of n = ½. The stretched exponential fit was found to be more appropriate for relaxation in solid silicates and amorphous silica than a conventional exponential expression for which n=1, isotropic relaxation. The exponential growth curve and linear T_1 plot for forsterite reacted in both water and brine in 0-2 mm and 4-6 mm slices are shown in Figure 3.4 and Figure 3.5, respectively. The exponential growth curve plots of T_1 for amorphous silica at different depths are shown in Figure 3.6. It turns out that the last delay of 390 s is about 2*T_1 of forsterite and more than 5*T_1 of amorphous silica.

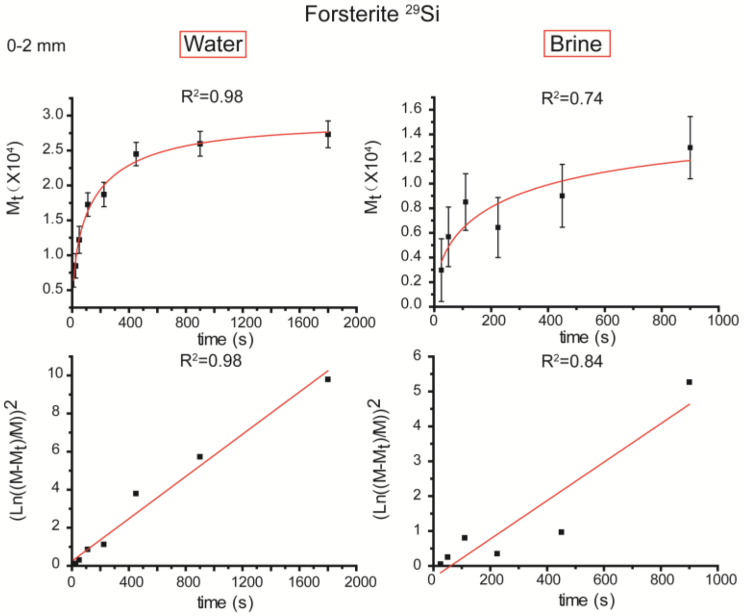

Figure 3.4 The exponential growth curve of the forsterite ^{29}Si NMR resonance from the 0-2 mm slice for the reactions in water and brine are shown. The semi-log plot of the same data is also exhibited for reference. The ^{29}Si T_1 values extracted from the stretched exponential plots are 153 s for water and 293 s for the brine. The values from the semi-log plots are 180 s (±11 s) for water and 181 s (± 33 s) for brine.

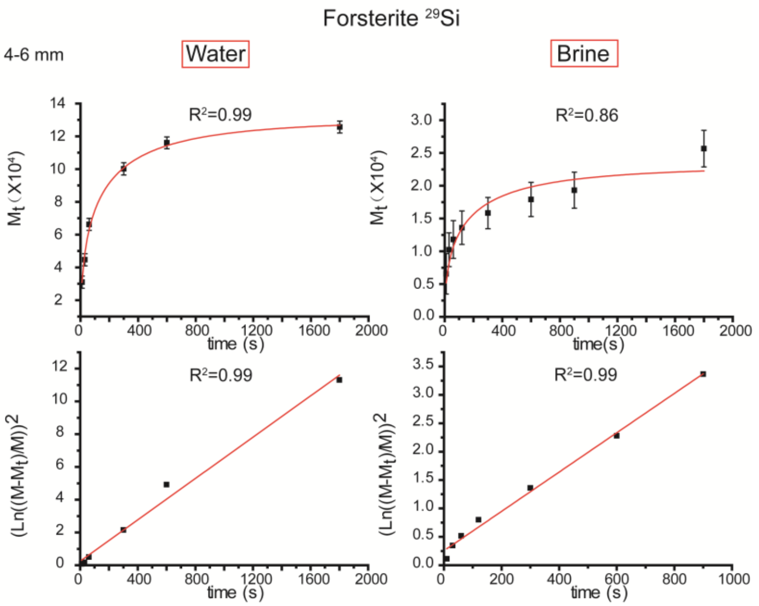

Figure 3.5 The exponential growth curve of the forsterite ^{29}Si NMR resonance from the 4-6 mm slice for the reactions in water and brine are shown. The semi-log plot of the same data is also displayed for reference. The ^{29}Si T_1 values extracted from the stretched exponential plots are 136 s for water and 153 s for the brine. The values from the semi-log plots are 159 s (± 8 s)for water and 289 s (± 11 s) for brine.

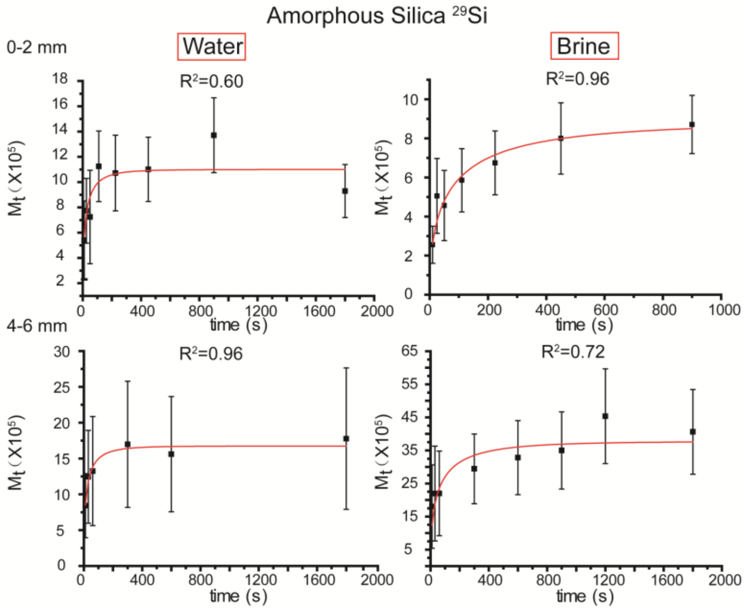

Figure 3.6 The exponential growth curve of the amorphous silica ^{29}Si NMR resonance(s) of the 0-2 mm and 4-6 mm slices for the reactions in water and brine are shown. The T_1 values extracted from the stretched exponential plots are 19 s for water and 80 s for brine (for the 0-2 mm slices). The T_1 values derived from the stretched exponential plots are 20 s for water and 63 s for brine (for the 4-6 mm slices). Semi-log plots are not helpful here, because the

poor signal-to-noise ratios lead to large errors in the estimate of the infinite time magnetization, M. Consequently, the linear (semi-log) plots were less reliable at giving estimates of the T_1 values.

3.3.3 ^{29}Si{^{1}H} MAS NMR as a Function of Depth

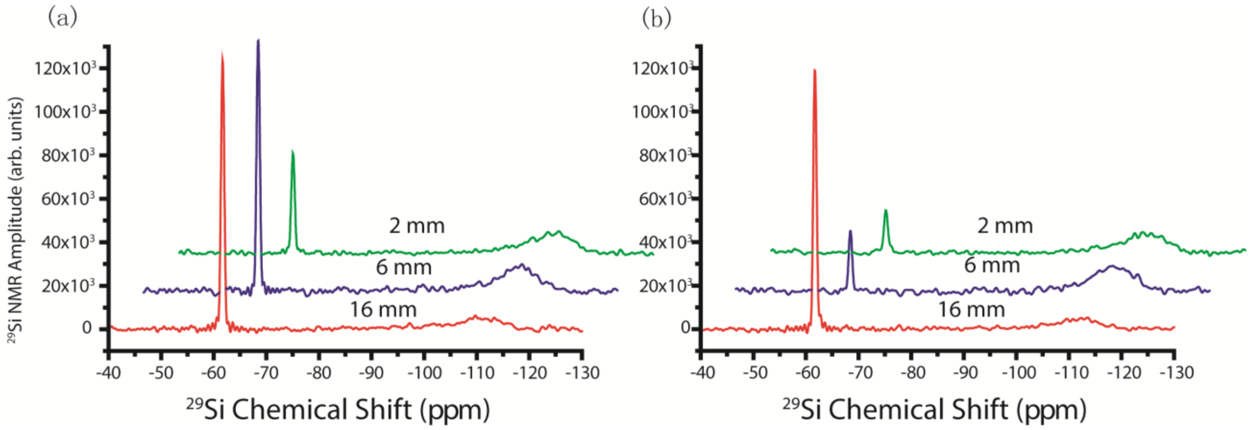

Figure 3.7 ^{29}Si{^{1}H} MAS spectra with ^{1}H decoupling for the reacted forsterite at sample depths 2 mm, 6 mm and 16 mm, (a) in water and (b) with 1.0 M NaCl (brine).

Figure 3.7(a) shows the ^{29}Si {^{1}H} MAS NMR spectra for the reaction of forsterite with ^{13}C labeled $^{13}CO_2$ in water. The resonance at -61.70 ppm is assigned to forsterite, similar to prior reports.[83] The resonance has a narrow linewidth (0.74 ppm) that agrees well with these reports, consistent with a polycrystalline high-purity solid. A broad resonance centered at approximately -110 ppm is typical amorphous silica. Figure 3.7(b) shows the ^{29}Si {^{1}H} MAS NMR spectra for the same reaction mixture in the presence of NaCl brine. The smaller peak area for the forsterite resonance means more extensive dissolution near the top of the packed bed (2 mm). These peak areas are recorded with recycle delays that are approximately 2*T_1 relaxation time for forsterite because of the need to record many transients and the inability to signal average over very long periods. (A recycle delay of 765 s would be required for the spectrum to be quantitative.) Therefore, the peak areas are not quantitative, but they may be used qualitatively.

While not rigorously quantitative (which would require a recycle delay of 5^*T_1 between transients), the relative areas of these peaks can be readily compared. The relative intensities within the series shown in Figure 3.7 (a) and (b) are meaningful, as well as the comparison between them. Table 3.1 presents the values for the integrated area of the (reactant) Mg_2SiO_4 ^{29}Si resonance and the precipitated amorphous ^{29}Si resonances for each of the slices. The amorphous silica that is formed (as a percentage of the total ^{29}Si signal) through dissolution-precipitation is larger in the 6 mm slice, as shown in Table 3.1, which matches the trend found for the forsterite dissolution, with more dissolution found closer to the surface of the packed bed.

Table 3.1 Deconvoluted peak areas of ^{29}Si{^{1}H} MAS NMR for different sample slices, with or without NaCl.

Sites	In water			In NaCl brine		
^{29}Si (mm)	Mineral starting materials area	Amorphous product	Total area	Mineral starting materials area	Amorphous product	Total area
2 mm	2166-2716	6005	8171-8721	1010-1475	5811	6821-7286
6 mm	5445-6672	6689	12134-13361	1335-1674	6639	7974-8313
16 mm	5839-7299	3552	9391-10851	5638-7048	2904	8542-9952

*Forsterite mineral "starting materials" columns give a range of areas, considering that they are recorded with recycling delays less than 5^*T_1. Areas have been scaled from ~2^*T_1 to 5^*T_1 based on their projected magnetization buildup.

The ^{29}Si{^{1}H} NMR and the data in Table 3.1 demonstrate the dramatic differences observed in the presence of NaCl: the NaCl leads to a greater extent of forsterite dissolution but not to a correspondingly higher amount of amorphous silica precipitation. A larger amount of forsterite dissolved in the 2 mm and 6 mm samples in brine compared to the reaction in water, indicating that NaCl facilitates the dissolution of forsterite. These observations are consistent with an earlier batch dissolution study of forsterite in CO_2-saturated solutions that found greater extents of dissolution in NaCl solution than in a more dilute solution.[82] We surmise that in the process of mineralization, the pH drops upon CO_2 exposure, and the Na^+ present reacts with Si-OH to form Si-ONa,[87] which could inhibit the formation of amorphous silica by preventing its condensation polymerization from building the silica network. As a result, more orthosilicic acid would be released from the packed bed in the 2 mm and 6 mm samples. Notably, the 6 mm slice in Figure 3.7(b), does show a somewhat larger ^{29}Si amorphous silica resonance compared to others in this packed bed, but it is not substantially more significant for the water-only sample. These results suggest that while more forsterite has dissolved at 6 mm in the presence of NaCl brine, it does not lead to a concurrently larger amorphous product.

Also, while there is significant forsterite dissolution in the water-based slurry, the amorphous silica is not proportionally greater in the topmost layer. The amorphous silica component is similar between 2 mm and 6 mm samples, even though there is significantly less dissolution deeper in the packed bed. It is possible that at the top (0 to 2 mm), the orthosilicic acid (H_4SiO_4) can diffuse out of the sample. A similar process of reactant diffusion out of the topmost layers of the packed bed has been suggested by reactive transport modeling[88] to limit magnesite precipitation in this layer with the greatest magnesite accumulations occurring somewhat more in-depth into the bed.

3.3.4 Analysis of Q^n Sites in Amorphous Silica

With the help of {^{1}H} decoupling, we could identify Q^3 sites. However, Q^1 and Q^2 resonances are not evident here. ^{29}Si{^{1}H} CPMAS spectra, as one more piece of evidence, were recorded

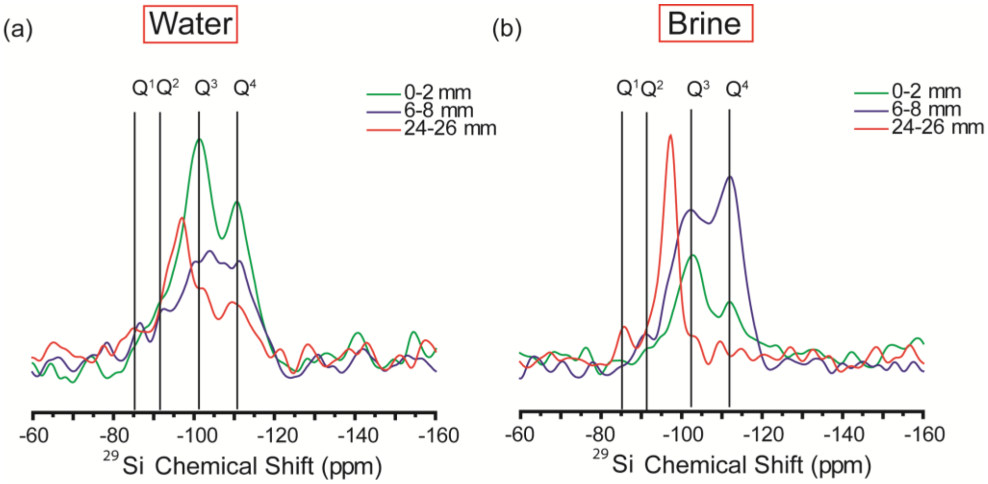

Figure 3.8 $^{29}Si\{^1H\}$ CP MAS of representative slices of the packed bed reactor of forsterite (a) in water and (b) in brine: 0-2, 6-8, and 24-26 mm.

and are shown in Figure 3.8 to show the absence of Q^1 and Q^2. While CPMAS is not quantitative (owing to different coupling strengths to protons that may be distant—as for the Q^4 species), it can serve to identify the various types of silica sites that are present. The different positions for Q^1, Q^2, Q^3 and Q^4 amorphous silica sites are shown by the vertical bars. Importantly, the presence of Q^3 silica is seen in all the water-reacted forsterite, and it is only absent in the deepest (24-26 mm) slice from the brine-reacted sample. The resonance that appears between Q^2 and Q^3 is assigned to a distortion of the O-Si-O bonding angle for Q^3. From these spectra, we know of the presence of Q^3, and $^{29}Si\{^1H\}$ MAS NMR can help us to quantify different Q^n signal. To best resolve the carbonation reaction in brine versus a water-only slurry, we used the DMFIT program to deconvolute the amorphous silica resonances from $^{29}Si\{^1H\}$ MAS into Q^3 and Q^4 sites. Figure 3.9 shows the deconvolution of the amorphous silica ^{29}Si NMR resonance into multiple Gaussian peaks. While a Q^3 species was fit to both sets of samples, the water-only packed bed had more intensity of Q^3 resonances overall, which is due to the effect of Na^+ as discussed above. In the NaCl-brine, Q^3 sites were fit to the amorphous region based on the same chemical shift and peak width, yet there is only minor evidence of its presence given the low signal-to-noise ratios for Q^3 in the 6mm and 16mm samples.

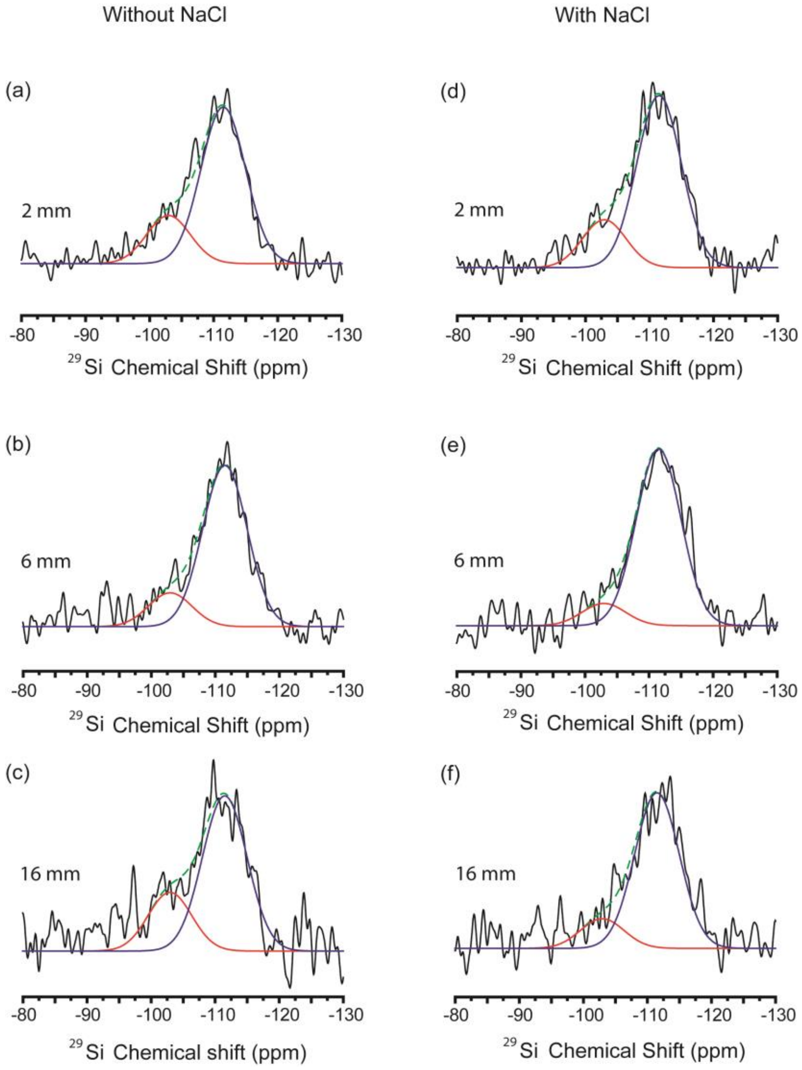

Figure 3.9 Deconvolution of amorphous silica ^{29}Si{^{1}H} MAS NMR resonance by Dmfit into two Gaussian line-shapes. (a-c) are from the slurry with water only, no NaCl, and (d-f) are from the slurry with 1.0 M NaCl present.

Previous studies have shown the dissolution of amorphous silica was affected by the pH, metal cation(s) present, and temperature.[89,90] At the surface of the packed bed, the pH of the solution is estimated to be approximately 3.2,[78] which will affect the top 2 mm sample. Consequently, the Q^3 silica will be the most stable.[10,90] These conditions lead to the high relative Q^3 content for the top layer. Also, there is increasing pH as a function of depth, creating conditions that differ at the surface. For the samples in the packed bed, the pH will increase with depth, favoring deprotonation of Q^3, $–SiO^–$ over –SiOH. Thus, there is lower Q^3 signal in 6 mm and 16 mm slices.

3.3.5 $^{13}C\{^1H\}$ MAS NMR

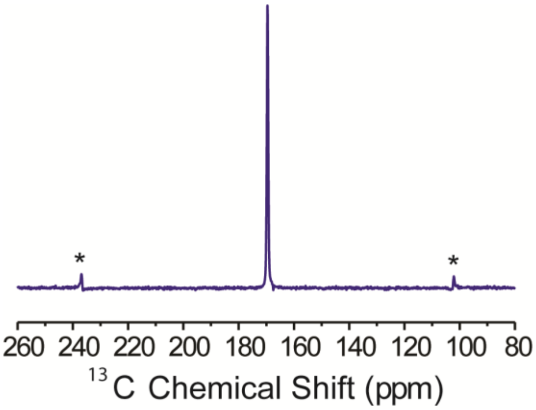

Figure 3.10 $^{13}C\{^1H\}$ MAS NMR of the 6 mm sample for the reaction of forsterite and $^{13}CO_2$ in pure H_2O as described previously. The resonance is assigned based on the chemical shift to $MgCO_3$. Spinning sidebands are marked by "*".

Figures 3.7 shows a diminution of forsterite dissolution as a function of depth in the column of the reacting slurry—as evidenced by the intensity of its ^{29}Si NMR resonance. The dissolution of forsterite is most extensive in the regions closest to the CO_2-saturated water because the pH will be lowest in this zone, especial in the 2 or 6 mm section. Investigating the formation of solid-state carbonate as a function of depth is also useful to accompany the ^{29}Si spectra. $^{13}C\{^1H\}$ MAS NMR of the 6 mm slice for the reaction of forsterite with $^{13}CO_2$ in water is shown in Figure 3.10. There is a single ^{13}C resonance around 170 ppm, and assigned to magnesite.[91] The spectra of ^{13}C NMR for different slices are the same for both samples in water or NaCl solution, implying a single type of carbonate is formed. The $^{29}Si\{^1H\}$ and $^{13}C\{^1H\}$ MAS NMR integrated peak areas as a function of depth in the packed bed are shown in Figure 3.11. This plot permits comparison between the single-shot ^{13}C MAS NMR data and the intensity of forsterite silicon or amorphous silica as a function of depth. In Figure 3.11, the magnitude of the ^{13}C signal is related to the precipitation of carbonate after dissolution of forsterite. For the reaction with water, the intensity of ^{13}C decreases going to the deeper slices, which is a result of decreasing forsterite dissolution. The maximum signal for ^{13}C is found in 6-8 mm slices for the reaction of forsterite with $^{13}CO_2$ in NaCl solution, since NaCl can facilitate the dissolution of forsterite.

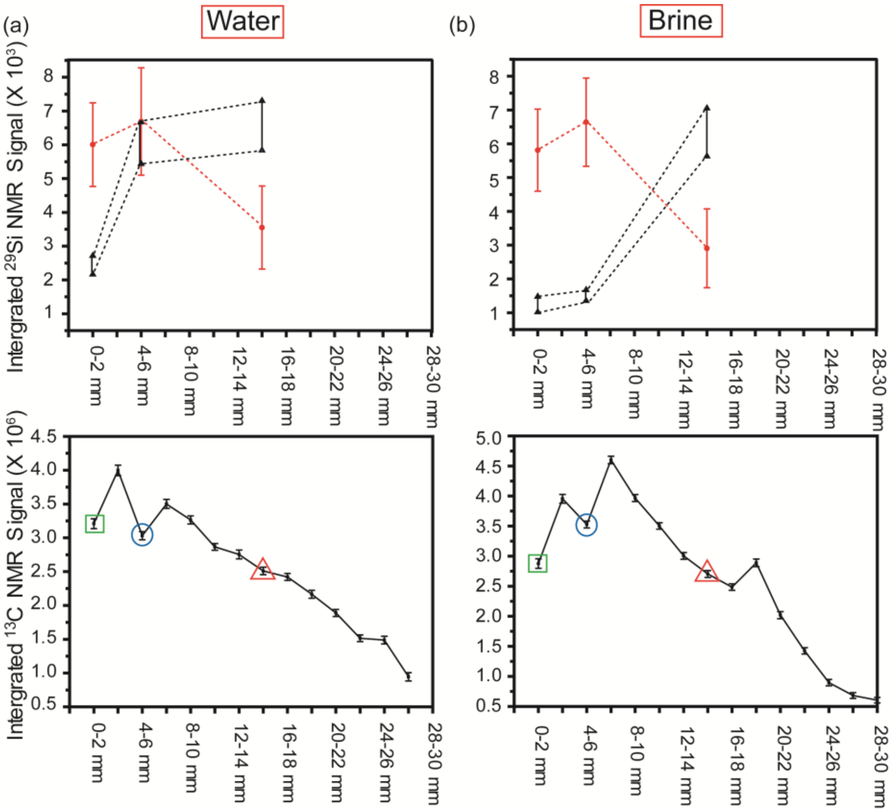

Figure 3.11 ^{29}Si{^{1}H} and ^{13}C{^{1}H} MAS NMR integrated peak areas of as a function of sample depth in the packed bed. The ^{29}Si data are shown in the upper figures--forsterite is shown as black triangles (giving a range of values to reflect the incomplete relaxation of this resonance), and amorphous silica is shown as red circles. The ^{13}C NMR data are shown in the lower figures with data points circumscribed by a shape to indicate the corresponding slices where ^{29}Si was also analyzed (a) from the reaction of forsterite with $^{13}CO_2$ in water and (b) from the reaction of forsterite with $^{13}CO_2$ in brine.

3.4 Conclusions

We have undertaken an NMR study of two packed beds of forsterite reacted with $^{13}CO_2$: one with a water-slurry and one with a 1.0 M NaCl brine-slurry, reacted with elevated-temperature and -pressure conditions. We have evaluated ^{29}Si SSNMR of the packed beds as a function of depth for three samples: at 0-2 mm, at 4-6 mm, and 14-16 mm for typical amorphous silica. Related ^{13}C SSNMR data for the precipitated $MgCO_3$ are also reported as a function of depth for comparison. The maximum magnesite formation was found in the range of 4 mm – 8 mm, with a decrease in total magnesite as a function of depth. We have conducted a series of experiments with a relatively long recycle delay (390 s) to achieve sufficient signal-to-noise ratios to qualitatively probe the identity of silicon-containing reaction products from forsterite dissolution, including amorphous silica that has been challenging to identify using other techniques.

The fate of the silicon from forsterite (Mg_2SiO_4) is essential to determine since the precipitation of amorphous silica can affect forsterite dissolution. The ^{29}Si NMR data show both dissolutions of the forsterite and condensation of amorphous silica—as both Q^3 and Q^4 silica species. NaCl-containing brine enhances dissolution of forsterite deeper in a packed bed than water alone. The water-only reactions favor the formation of both Q^3 and Q^4 amorphous silica, whereas there is less Q^3 silica in the presence of the brine. NaCl appears to inhibit the formation of the Q^3 species. Even with the enhanced dissolution of forsterite in NaCl-brine, it is notable that the amounts of amorphous silica found were not concomitantly larger, suggesting some of the silica may have dissolved into the liquid phase.

3.5 Acknowledgements

This material is based upon work supported by the Department of Energy under Award Number DE-FE0023382. This report was prepared as an account of work sponsored by an agency of the United States government. The design of initial experiments with NaCl solutions benefits from discussions with Fei Wang. Early experiments were conducted with funding from Washington University's Consortium for Clean Coal Utilization.

Chapter 4: NMR Crystallography: Evaluation of Hydrogen Positions in Hydromagnesite

The material in this chapter is adapted with permission from Jinlei Cui, David L. Olmsted, Anil .K. Mehta, Mark Asta and Sophia E. Hayes, Angewandte Chemie, 2019, 58. 4210. Copyright 2019 Angewandte Chemie International Edition.

4.1 Introduction

Structural information of hydrogen positions is a critical aspect of materials science,[92] biochemistry[93,94] and the growing field of crystal engineering.[95] Physical and chemical properties of solids are strongly influenced by atomic positions that dictate coordination geometry and hydrogen bonding.[96,97] One example is divalent metal carbonates, which have garnered interest for geological sequestration of CO_2 as solid-state carbonate minerals.[98,99] Although magnesite ($MgCO_3$) is considered the most thermodynamically stable carbonate product from sequestered CO_2, different thermodynamically stable hydrated carbonates including hydromagnesite [$4MgCO_3 \cdot Mg(OH)_2 \bullet 4H_2O$][75] form under various conditions.[100,101] Determining the atomic structure of hydrated carbonate minerals will lead to an improved understanding of how coordination and H-bonding stabilizes the magnesium carbonates on the pathway to full dehydration to the $MgCO_3$ endmember. This has been a long-standing geochemical question addressed by researchers seeking to explain cation (i.e., Mg^{2+} and Ca^{2+}) hydration and its role in crystallization as hydroxy-hydrated carbonate structures.[102–105]

In this chapter, we apply NMR crystallography principles to hydromagnesite to adjust hydrogen atomic positions in the unit cell to better reflect the experimental data. Structure refinement was evaluated with SSNMR and computational methods. Hydromagnesite offers a unique opportunity for study because the hydrogen sites (as H_2O and OH^- moieties) are sufficiently sparse to enable us to probe them through heteronuclear dipolar interactions to carbon via ^{13}C observe, ^{1}H dephase rotational-echo double resonance ($^{13}C\{^{1}H\}$ REDOR) NMR[22,106]. Dipolar coupling between ^{13}C and ^{1}H is normally complicated to measure, as protons are typically strongly coupled to each other via homonuclear dipole-dipole interactions. The sparse density of hydrogens in hydromagnesite and other minerals diminishes such ^{1}H-^{1}H influence and offers a unique opportunity to probe ^{13}C-^{1}H interactions. This hydromagnesite study is one of only a few REDOR examples involving ^{1}H--from a search of the literature, we have found only 16 reports of ^{1}H-dephased REDOR, and only 4 of those are between ^{1}H and ^{13}C.[107–110]

4.2 Experimental methods

4.2.1 Preparation of 10% ^{13}C Enriched Hydromagnesite

10% ^{13}C enriched hydromagnesite was prepared as previously reported.[91] 0.011g of 98% ^{13}C enriched $NaH^{13}CO_3$ (Sigma) and 0.096g natural abundance $NaHCO_3$ (Sigma) were added to a solution of 2.5 mmol $MgCl_2 \cdot 6H_2O$ in 7.8 ml of de-ionized (DI) water. 10% ^{13}C enrichment was chosen to diminish the ^{13}C-^{13}C homonuclear dipole-dipole interaction for the $^{13}C\{^{1}H\}$ REDOR experiments.[110] After 1 minute of mixing, the solution was heated and held at 92°C for four days in a closed vessel. Upon cooling, the precipitate was rinsed with DI water and dried under vacuum at room temperature for one day.

4.2.2 Powder XRD

Powder X-ray diffraction (PXRD) of the 10% ^{13}C enriched hydromagnesite was obtained with a Bruker d8 Advance X-ray diffractometer using Cu-Kα radiation at 40 kV and 40 mA. The sample was held in a Plexiglas PXRD slide. Data were collected over a 2θ range from 5° to 90° with a step size of 0.019°.

4.2.3 Solid-State NMR

Static ^{13}C (74.18 MHz) NMR spectra with ^{1}H (294.97 MHz) decoupling were collected in an Oxford superconducting 7.05 T magnet with a Tecmag (Houston, TX) console equipped with a Chemagnetics 4 mm MAS HXY probe. ^{13}C spectra were acquired using a Hahn-echo pulse sequence [28,111](π/2-τ-π-τ-echo) with a π/2-pulse of 4 μs, a π-pulse of 8 μs, and a τ delay of 30 μs. 720 transients were recorded with a recycle delay of 480 s, which is approximately 3 times the spin-lattice relaxation time.[91] ^{1}H decoupling was applied with an RF strength of ν_{RF} = 42 kHz. The static ^{13}C NMR spectrum was fit using Dmfit[112] to obtain principal values of the chemical shift tensor: δ_{xx}, δ_{yy} and δ_{zz}, which are reported using the Haeberlen convention.[20]

^{13}C (148.34 MHz) and ^{1}H (589.84 MHz) NMR spectra with MAS were recorded on a 13.8 T Oxford superconducting magnet using a Bruker 2.5 mm HX MAS probe. ^{1}H MAS NMR spectra were acquired using a rotor-synchronized Hahn-echo with a π/2-pulse length of 4.9 μs, π-pulse length of 9.8 μs, MAS rotation frequency (ν_r) of 25kHz, and a τ delay of 32.65 μs to center the π-pulse at the middle of the rotor period. ^{1}H MAS spectra were recorded with 32 transients and a 10 s recycle delay. $^{13}C\{^{1}H\}$ CPMAS spectra were acquired with an initial ^{1}H π/2 pulse width of

3.4 μs, ^{1}H-^{13}C cross-polarization Hartman-Hahn contact time of 750 μs, 64 transients and a recycle delay of 10 s. The MAS rotational frequency was maintained at 25 kHz with a Tecmag MAS controller.

$^{13}C\{^{1}H\}$ REDOR[29] measurements were acquired with ^{13}C π-pulse widths of 10.8 μs and ^{1}H π-pulse widths of 6.8 μs. Observe spin (^{13}C) refocusing pulses were centered every rotor period, and dephasing (^{1}H) pulses were centered halfway through the rotor period for maximum dephasing. XY-4 phase cycling of the rotor-synchronized ^{13}C and ^{1}H π-pulses was used to minimize artifacts from RF-inhomogeneity and resonance frequency offsets during the REDOR evolution time.[113] The MAS rotational frequency was maintained at 25 kHz with a Tecmag MAS controller.

For all NMR experiments, ^{13}C chemical shifts were referenced to adamantane as an external secondary reference with the $^{13}CH_2$ resonance set to 38.48 ppm. ^{1}H chemical shifts were referenced to liquid tetramethylsilane (TMS) at 0 ppm.

$^{13}C\{^{1}H\}$REDOR simulations of the 10-spin systems (1 carbon and 9 nearest hydrogens) were carried out using SIMPSON[114]. The maximum time step (max dt) over which the Hamiltonian is approximated to be time-independent was set to 1 μs in SIMPSON. XY-4 phase cycling of the rotor-synchronized ^{13}C and ^{1}H π-pulses was used to simulate the real experiment. Finite pulse widths were assumed. All calculations contained negligible imaginary contributions, and the initial amplitudes of the real parts were taken for REDOR analyses. Data convergence was checked by repeating selected calculations using smaller max dt (maximum time step over which the Hamiltonian is considered time independent) and more extensive powder averaging schemes.

RMSE values are computed between the experimental data and the REDOR curve, and are denoted on the figure to assess quality of the match.

4.2.4 DFT Calculations

All of the DFT calculations were performed using the Vienna Ab initio Simulation Package (VASP)[115], versions 5.3.5 and 5.4.4.18Apr17-6-g9f103f2a35 by collaborators Mark Asta and David Olmsted (UC Berkeley). These calculations made use of the projector-augmented wave (PAW) method[116,117] and Perdew−Burke−Ernzerhof (PBE)[59] GGA based potentials from the VASP library. All calculations were non-spin-polarized. In the structural optimizations, the PBE-GGA functional was used, as well as 2 different functionals incorporating van der Waals (vdW) interactions within DFT. They include the vdW-DF[118–120] and vdW-DF2[118–121] functionals.

The electronic wave functions were expanded in a plane-wave basis set, using a kinetic-energy cutoff of 610 eV. In the structure optimization calculations, cell parameters and atomic positions were relaxed until the components of the stress tensor were less than 0.1 kbar, and force on each atom was less than 0.001 eV/Å in magnitude. During the structural relaxations of the hydromagnesite compound (which has a finite bandgap), the sampling of the Brillouin zone was performed using the tetrahedron method with Blöchl corrections and a k point density of 2x2x2.[122]

To provide input files for VASP, the Materials Project "Crystal Toolkit" [123] was employed to convert structure files (.cif) to VASP input format. We note that this conversion interchanged the definition of the a and c axes, causing these to be reported differently between the ICSD data and that shown in Table 4.3.

The calculation of NMR chemical shifts made use of the linear response formalism[124,125] implemented in VASP, within the PBE-GGA functional. In these calculations use was made of a Gaussian smearing of 0.1 eV set to ensure negligible partial occupancies of the electronic states. Convergence was tested with respect to the k-point grid, the real-space grid, and the plane wave cutoff. Using higher levels of convergence only led to small changes in calculated NMR CSA parameters: the largest variation in η_{CSA} was 0.002, and the largest variation in δ_{iso} or υ was 1 ppm. (see the equations in chapter 1)

We find that the calculated structures for hydromagnesite obtained with some of these vdW functionals, when used as the basis for the NMR chemical shift calculations, yield improved agreement with experimentally measured CSA parameters relative to calculations based on the structure derived from semi-local GGA-PBE. Other vdW functionals lead to agreement no better than structures from GGA-PBE. The version 2 (vdW-DF2),[118–121] was found to yield the best agreement with experimental measurements, and is the focus of the calculation results presented in the main text.

4.3 Results and Discussion

4.3.1 XRD of Synthesized Hydromagnesite

The powder XRD (PXRD) pattern of the synthesized sample is shown in Figure 4.1, along with the reference patterns of hydromagnesite[126,127] in red (ICSD 920) and nesquehonite[128] in blue (ICSD 91710). There is good agreement between the PXRD pattern of the synthesized sample with 10% ^{13}C enrichment and that of the hydromagnesite reference, indicating that hydromagnesite is formed and no other crystalline phases of hydrated magnesium carbonate.

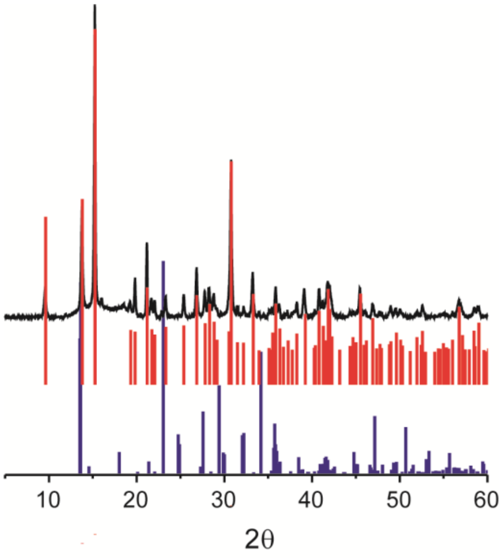

Figure 4.1 Powder XRD characterization of synthesized hydromagnesite. Top (black) diffraction pattern is experimental data, middle (red) pattern is the hydromagnesite reference diffraction pattern,[126] and bottom (blue) is the diffraction pattern of nesquehonite, another potential byproduct of the reaction. The XRD pattern matches well to that of the hydromagnesite crystal structure, and the experimental data show that nesquehonite was not formed.

4.3.2 ^{13}C MAS NMR and ^{1}H MAS NMR

Hydromagnesite possesses two distinct carbon sites in its lattice. While both are nominally carbonates (CO_3^{2-}), they are magnetically inequivalent, and through their ^{13}C NMR spectra one can distinguish specific interactions with water molecules and hydroxides (OH^-). The two sites are highlighted (by ovals) in the crystal structure of hydromagnesite, published by Akao,[127] in Figure 4.2.

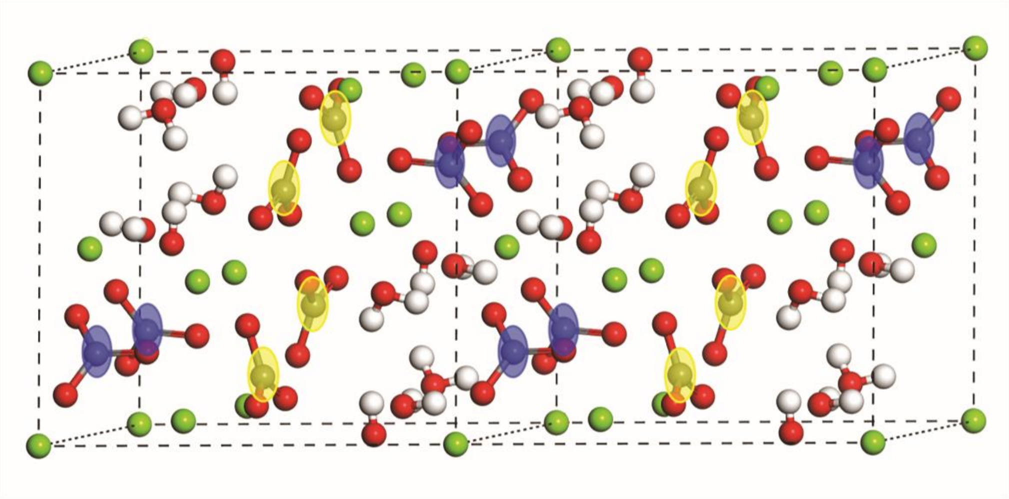

Figure 4.2 Crystal structure of hydromagnesite (two-unit cells shown, side by side). Magnesium is shown in green (spheres), oxygen is red, hydrogen is white, and carbon is gray. The blue and yellow oval shapes added to highlight representative carbon atoms correspond to the two types of carbon environments, Carbon 1 and Carbon 2, respectively.

Consistent with prior results[91] two ^{13}C solid-state NMR resonances are observed (Figure 4.3a) with isotropic chemical shifts of 163 ppm (hereafter “Carbon 1”) and 165.3 ppm (“Carbon 2”). The peak areas are approximately in a 1:1 ratio. The protons are separated in well-defined crystallographic sites, such that they are not subject to significant ^{1}H homonuclear dipole-dipole interactions. Two well-resolved ^{1}H resonances are observed in the ^{1}H spin-echo MAS NMR spectrum (Figure 4.3b) at -1.7 ppm assigned to OH^-, and at 5.0 ppm assigned to H_2O.[129]

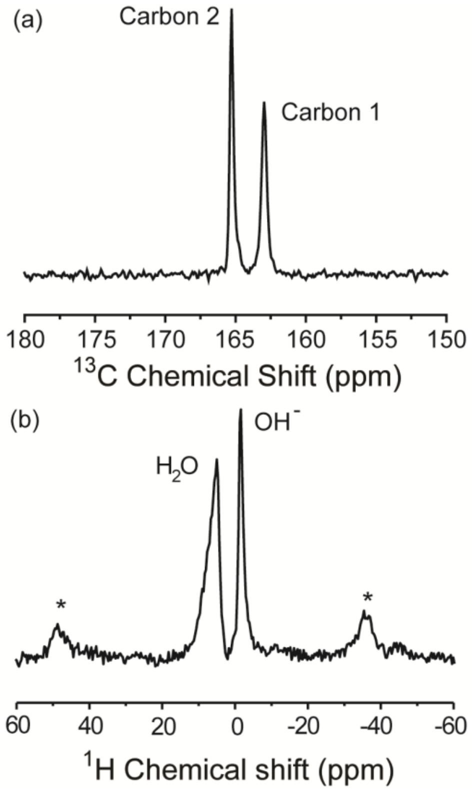

Figure 4.3 SSNMR of ^{13}C-enriched hydromagnesite powder. (a) $\{^1H\}^{13}C$ CPMAS (ν_r=25 kHz), and (b) ^{1}H rotor-synchronized Hahn echo MAS (ν_r=25 kHz). * denotes spinning side bands of H_2O.

4.3.3 Static ^{13}C NMR and Slow Spinning ^{13}C CPMAS NMR

Of particular utility are the static carbonate ^{13}C lineshapes that are dominated by CSA broadening of the local carbon environment, especially how the oxygens of the carbonate interact with nearby water and hydroxide protons. The static ^{13}C NMR spectrum (with ^{1}H decoupling) at 7.05T for 10% ^{13}C-enriched hydromagnesite is shown in Figure 4.4 (in black).

The static lineshape reflects the values of the ^{13}C CSA tensor and is related to the local geometric and electronic structure that distorts the carbonate from ideal axial (D_{3h}) symmetry. This lineshape therefore is sensitive to structural changes such as torsion angles and hydrogen-bonding.

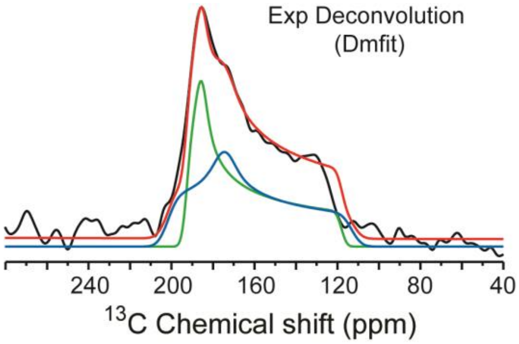

Figure 4.4 ^{13}C static NMR spectra of hydromagnesite. Experimental ^{13}C data are shown in black, the simulated CSA-broadened lineshapes for Carbon 1 in blue and Carbon 2 in green, and the sum of both carbons in red. The spectrum was fit using Dmfit, denoted "Exp Deconvolution".

Using the 2008 IUPAC conventions[130] (that derive from the Haeberlen convention[20]), we can describe the CSA lineshapes from elements of the diagonalized chemical shift tensor: the asymmetry parameter (η_{CSA}), isotropic chemical shift (δ_{iso}) and reduced anisotropic chemical shift (δ_{aniso}) expressed as:

$$\eta_{CSA} = \frac{\delta_{YY} - \delta_{XX}}{\delta_{ZZ} - \delta_{iso}} \qquad (1)$$

$$\delta_{iso} = \frac{1}{3}(\delta_{XX} + \delta_{YY} + \delta_{ZZ}) \qquad (2)$$

$$\delta_{aniso} = \delta_{ZZ} - \delta_{iso} \qquad (3)$$

The value for η_{CSA} provides insights about the local symmetry of a carbon site. For instance, the existence of a high-symmetry C_3 axis leads to an η_{CSA} value of 0, and any lowering of that 3-fold symmetry leads to a nonzero η_{CSA} value ($0 \leq \eta_{CSA} \leq 1.0$).

Deconvolution of the static ^{13}C NMR spectrum into individual lineshapes corresponding to the two carbon sites is performed with Dmfit and also shown in Figure 4.4. These are the best fits assuming that the areas under both curves are equal, finding the best static CSA-broadened lineshape that matches the experimental spectra (values shown in Table 4.1). Blue and green lineshapes are the two CSA powder patterns for Carbon 1 and Carbon 2, respectively. The red spectrum is the sum of the fits for both carbons.

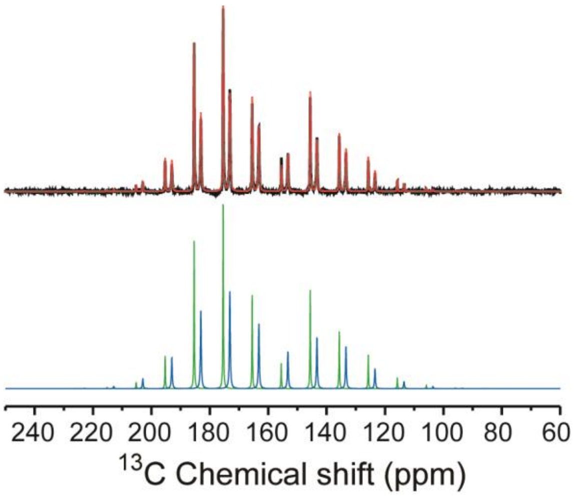

Figure 4.5 Slow spinning $^{13}C\{^{1}H\}$ CPMAS NMR (ν_r = 2 kHz) of hydromagnesite and the simulation of the spectrum by Dmfit. Experimental ^{13}C data are shown in black, Carbon 1 in blue, Carbon 2 in green, and their sum in red. The η_{CSA} of Carbon 1 and Carbon 2 is 0.54 and 0.15, respectively, and the δ_{aniso} of Carbon 1 and Carbon 2 is -47.0 and -46.8 ppm, respectively.

Slow spinning $^{13}C\{^{1}H\}$ CPMAS NMR ($\nu_{rotation}$ = 2 kHz) performed by Ivan Hung (NHMFL, Florida) and simulation of the spectrum are also shown in Figure 4.5 as evidence to confirm the CSA tensor from static lineshape. These data further confirm the η_{CSA} value for Carbon 1. Three elements of the diagonalized chemical shift tensor determined by ^{13}C static NMR and slow spinning $^{13}C\{^{1}H\}$ CPMAS NMR are summarized in Table 4.1. Carbon 1 (in blue) has the largest asymmetric distortion (η_{CSA} value of 0.55). Such a distortion implies that the proximity of OH^{-} and/or H_2O to the CO_3^{2-} group alters the electronic environment around the carbon.[131]

Table 4.1 ^{13}C Chemical shift tensor elements determined from slow spinning (ν_r = 2 kHz) ^{13}C{^{1}H} CPMAS NMR and static NMR.

	δ_{XX} (ppm) δ_{11} (ppm)*	δ_{YY} (ppm) δ_{22} (ppm)*	δ_{ZZ} (ppm) δ_{33} (ppm)*
Carbon 1			
Slow MAS NMR	199.2	173.8	116
Static NMR	201.8	174.3	113
Carbon 2			
Slow MAS NMR	192.2	185.2	118.5
Static NMR	192.5	185.4	117.9

*we are presenting both "standard" notation δ_{11}, δ_{22} and δ_{33}, (ordered by frequency from high to low) and the Haeberlen notation δ_{XX}, δ_{YY} and δ_{ZZ}, (where $| \delta_{ZZ} - \delta_{iso} | \geq | \delta_{XX} - \delta_{iso} | \geq | \delta_{YY} - \delta_{iso} | \geq$) for the diagonalized chemical shift tensor values.

4.3.4 Chemical Shift Computation by DFT and Simulation of Static Line-shape

Table 4.2 Experimentally and computationally (VASP) determined ^{13}C NMR CSA parameters for hydromagnesite using XRD atomic coordinates and atomic structures derived from DFT relaxation using different functionals.

Sites	Method	δ_{iso} (ppm)	δ_{aniso} (ppm)	η_{CSA}
Carbon 1	Exp ^{13}C NMR deconvolution (Dmfit)	163.0	50	0.55
Carbon 2		165.3	-47.4	0.15
Carbon 1	DFT (XRD)	154.1	-45.5	0.70
Carbon 2		161.4	-49.0	0.19
Carbon 1	DFT (GGA-PBE)	161.8	-47.7	0.28
Carbon 2		165.2	-49.1	0.14
Carbon 1	DFT (vdW-DF2)	165.0	-47.7	0.47
Carbon 2		167.8	-49.7	0.13

CSA paramters can also be calculated using quantum mechanical methods that reflect the atomic and electronic structure. The results of such calculations depend not only on the local environment but the extended 3D network found in crystals. Using atomic coordinates from the hydromagnesite crystal structure from the published X-ray refinement in the ICSD,[127] Vienna Ab initio Simulation Package (VASP)[115] calculations of the ^{13}C CSA tensors were performed using the GGA-PBE functional. To convert the calculated chemical tensors to predicted chemical shift for hydromagnesite, a linear relationship between calculated CSA tensors and experimentally determined chemical shift of magnesite, hydromagnesite and nesquehonite is shown in Figure 4.6. All the DFT calculations are run using GGA-PBE functional-relaxed structure. The CSA parameters from DFT calculations are shown in Table 4.2. The XRD crystal structure leads to predictions of NMR tensors that do not agree well with the experimental data: the prediction of the δ_{iso} and values for η_{CSA} both deviate from experimental measurements.

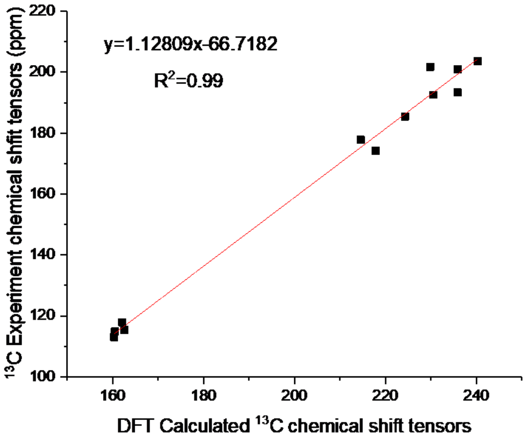

Figure 4.6 Linear rescaling of ^{13}C chemical shift tensor values. Experimentally measured values of diagonalized tensors are plotted versus VASP calculated values for magnesite ($MgCO_3$), hydromagnesite and nesquehonite. The experimental data of magnesite and nesquehonite are from a previous publication.[91]

To further refine the CSA tensor calculations, the atomic coordinates are optimized using the GGA-PBE functional. The results of the DFT calculations derived from the GGA-PBE relaxed structure are also shown in Table 4.2 (labeled as DFT (GGA-PBE)). The isotropic chemical shift of Carbon 1 and Carbon 2 through GGA-PBE atomic coordinates match experimental data better compared to the XRD-determined atomic coordinates. However, for Carbon 1, the computed result predicts a much higher-symmetry environment than XRD crystal structure and experiment (an smaller η_{CSA} value of 0.28); hence, the surrounding H_2O and OH^- species are predicted to interact less strongly with the carbonate represented by Carbon 1. The effects of such interactions are depicted in the lineshapes shown in Figure 7c (discussed below).

As described above, modifications of DFT have been proposed to more accurately model systems where weak interactions such as hydrogen bonding and dispersion forces are important. We optimized the atomic coordinates with in VASP for the hydromagnesite structure using multiple vdW-corrected functionals. The overall best agreement with both the CSA lineshape and isotropic chemical shift is obtained using the relaxed geometries obtained from the vdW-DF2 functional. The DFT calculation results from vdW-DF2 functionals are shown in Table 4.2, which gives a reasonably good match to experimental data for δ_{iso} and η_{CSA}.

To depict the static lineshapes, we simulated the ^{13}C static NMR lineshape through DFT calculation results. Given the precision of the isotropic chemical shift values, in the simulation of the static CSA lineshapes, the δ_{iso} is constrained to the experimentally-measured value, while the values for η_{CSA} and δ_{aniso} matched those determined by DFT. Figure 4.7. shows (a) the deconvolution result by Dmfit from experiment, simulated ^{13}C static lineshape from (b) DFT calculation using atomic coordinates from X-ray diffraction, (c) relaxations to atomic coordinates using GGA-PBE functional in VASP, and (d) using the vdW-DF2 functional in VASP. The simulation is done under the consideration of equal intensity for Carbon 1 and Carbon 2. For the XRD crystal structure, Carbon 1 indicates a higher asymmetry lineshape, and the sum of two carbons (red) does not match well with the experiment data (Figure 4.7b). The simulation of ^{13}C static line from GGA-PBE functional is shown in Figure 4.7c. We find that Carbon 1 has less asymmetry than the experimental deconvolution. Compared with others, the vdW-DF2 exhibits the best agreement from the simulation to the experimental curve. The best agreement with the experimental CSA lineshape data is found for the vdW-DF2 functionals.

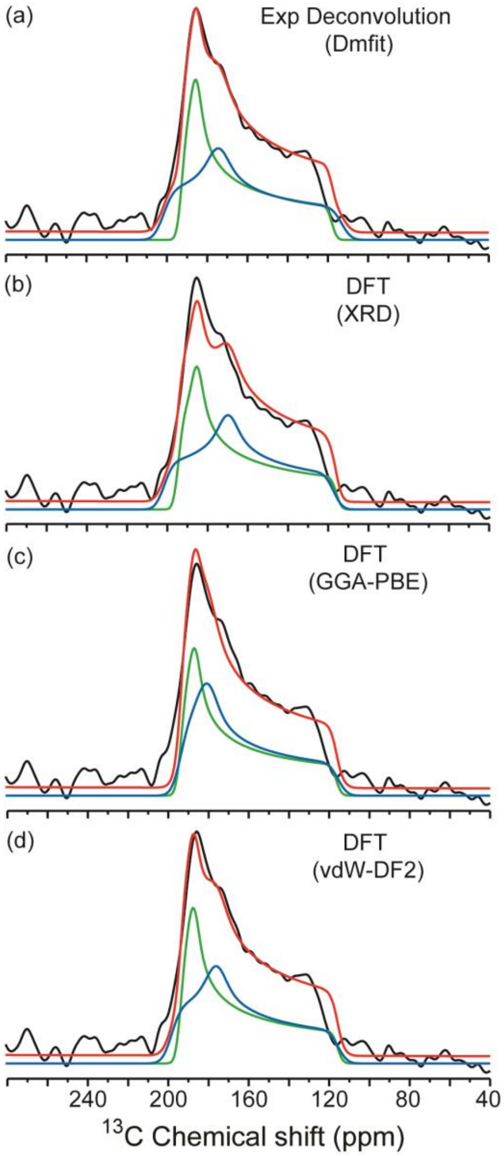

Figure 4.7 ^{13}C static NMR spectra of hydromagnesite and computed ^{13}C chemical shift tensors. Experimental ^{13}C data are shown in black, the simulated CSA-broadened lineshapes for Carbon 1 in blue and Carbon 2 in green, and the sum of both carbons in red. Best fit using: (a) Dmfit, denoted “Exp Deconvolution”; and simulated from NMR tensors determined (b) from VASP calculations using atomic coordinates from X-ray diffraction, (c) from relaxations using the GGA-PBE functional, and (d) from relaxations using the vdW-DF2 functional. δ_{iso}, η_{CSA} and δ_{aniso} determined by the simulations are shown in Table 4.2.

4.3.5 ^{13}C{^{1}H} REDOR and SIMPSON Simulation

Besides the CSA lineshape and DFT calculation of chemical shift tensors, we also tested the atomic coordinates by ^{13}C{^{1}H} REDOR, which is used to measure the distance between ^{1}H and ^{13}C in hydromagnesite. To locate hydrogens of the H_2O and OH^- groups surrounding the carbonate positions in the lattice, we determined ^{1}H-^{13}C distances by measuring the ^{13}C-^{1}H heteronuclear dipolar coupling using the NMR sequence, ^{13}C{^{1}H} REDOR.[132–134]The ^{13}C{^{1}H} REDOR experiment reintroduces the ^{1}H-^{13}C dipolar coupling that is averaged to nearly zero by MAS.[29,59]

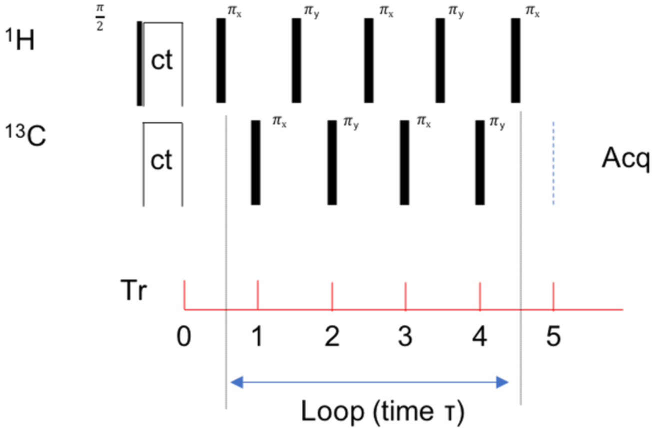

Figure 4.8 Pulse sequence of ^{13}C{^{1}H} REDOR NMR. ^{1}H is used as the dephasing channel, and ^{13}C is the observe channel. XY-4 phase cycling is used to minimize the influence of resonance off-set and inhomogeneities of B_1. “ct” stands for contact time, “Acq” for acquisition, “Tr” for rotor period, and “τ” for the evolution time for each successive loop number.

^{13}C{^{1}H} REDOR data are collected in two sets of experiments (Figure 4.8): a full-echo (S_o) spectrum with rotor-synchronized π-pulses on the ^{13}C observe spin to account for the effects of T_2 relaxation, and the S spectrum with dephasing π-pulses on the ^{1}H channel which reintroduces the ^{13}C-^{1}H dipolar coupling. The intensity difference ($\Delta S = S_o - S$) between the full-echo (S_o) and the dephased (S) spectra reflects the influence of ^{1}H-^{13}C dipolar coupling. S_o and S spectra are deconvoluted with Dmfit with the isotropic chemical shift and linewidth for each carbon held constant, allowing only the intensity to vary. Figure 4.9 shows $^{13}C\{^1H\}$ REDOR dephasing ($\Delta S/S_o$) as a function of REDOR evolution time for Carbon 1 and Carbon 2.

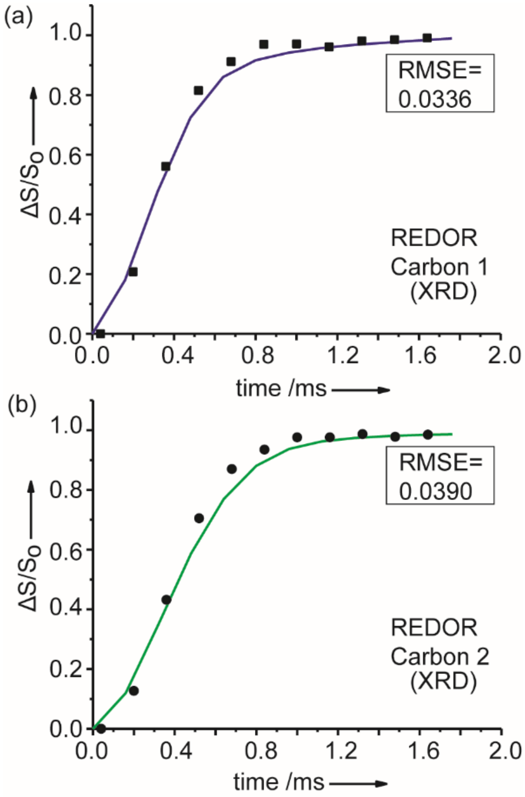

Figure 4.9 $^{13}C\{^1H\}$ REDOR NMR data (black squares and circles for Carbon 1 and Carbon 2, respectively) and calculated dephasing for (a) Carbon 1 at 163 ppm (blue line) and (b) Carbon 2 at 165.3 ppm (green line). The $^{13}C\{^1H\}$ REDOR simulations use atomic coordinates from the published crystal structure refined from X-ray diffraction (XRD) measurements.[127] RMSE values are given in the legend, comparing the agreement of the calculated REDOR curve to the experimental data.

First, from the atomic coordinates in the XRD crystal structure, $^{13}C\{^1H\}$ REDOR curves are simulated with SIMPSON[114] using the positions of the closest H_2O and OH^- species, amounting to 9 hydrogens specified by the published crystal structure (ICSD 920),[127] which is shown in Figure 4.10. Simulated $^{13}C\{^1H\}$ REDOR curves for both carbons exhibit an overall shape that agrees relatively well with the experimental data, especially at longer (> 1.2 ms) REDOR evolution times, where ^{13}C-^1H spin interactions from multiple distant ^1H spins dominate. However, the region just after initial slope of the simulated $^{13}C\{^1H\}$ REDOR dephasing curves for both Carbon 1 (shown in blue, Fig. 4.9a) and Carbon 2 (shown in green, Fig. 4.9b), underestimates the experimental dephasing, suggesting that the position of hydrogen atoms–especially those in close proximity whose interactions dominate the initial portion of the REDOR curve—are inaccurately specified. In addition, the XRD structure (ICSD 920) yields computationally (VASP) determined tensors that predict ^{13}C δ_{iso} (Table 4.2) that deviate substantially (5 – 10 ppm) from those found by experiment. *The ^{13}C CSA lineshape (Figure 4.7b), DFT predicted chemical shift (Table 4.2) and simulation of ^{13}C{^{1}H} REDOR (Figure 4.9) both suggest that the hydrogen positions are not accurately determined in hydromagnesite.*

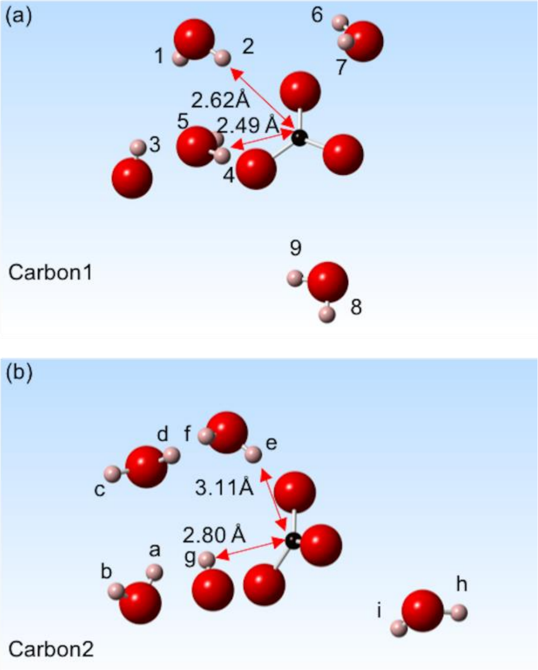

Figure 4.10 Positions of the nine hydrogens on the closest H2O and OH^- species (pink) from the XRD crystal structure (ICSD 920) surrounding (a) Carbon 1 (black) and (b) Carbon 2 (black) used in the calculation of REDOR dephasing. Oxygens are colored red. Distances from each carbon to the two closest protons are indicated, and all other distances are listed in Table 4.4. The hydrogens are denoted by numbers for Carbon 1 and alphabetical letters for Carbon 2 to distinguish easily between sets. 5 hydrogens from H_2O and OH^- are selected from each, plus 4 hydrogens that are part of the pair present in water molecules.

^{13}C{^{1}H} REDOR dephasing curve of Carbon 1 and Carbon 2 are also simulated for the atomic coordinates GGA-PBE relaxed structure and shown in Figure 4.11. There is a poorer match to the Carbon 1 experimental data (RMSE = 0.0505) over-estimating the initial slope of the experimental data curve, which is dominated by ^{13}C-^{1}H dipolar interactions of the protons closest to Carbon 1. In addition, the prediction of η_{CSA} for Carbon 1 by GGA-PBE is also 50% lower than experimental determination. Considering the ^{13}C CSA lineshape, CSA asymmetry parameter (η_{CSA}) and ^{13}C{^{1}H} REDOR, these all suggest that the relaxed structure obtained from the GGA-PBE functional does not accurately represent the atomic coordinates in hydromagnesite.

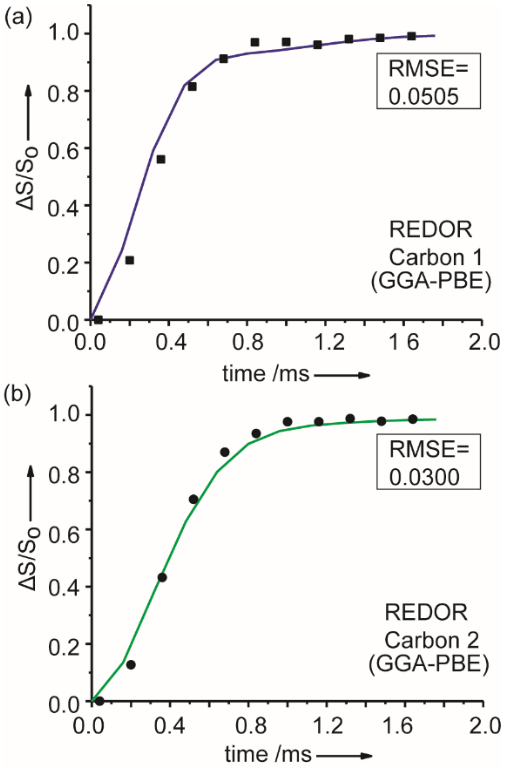

Figure 4.11 ^{13}C{^{1}H} REDOR NMR data (black squares and circles for Carbon 1 and Carbon 2, respectively) and calculated dephasing for (a) Carbon 1 at 163 ppm (blue line) and (b) Carbon 2 at 165.3 ppm (green line). The ^{13}C{^{1}H} REDOR simulations use atomic coordinates from relaxed crystal structure using GGA-PBE functional RMSE values are given in the legend, comparing the agreement of the calculated REDOR curve to the experimental data.

^{13}C{^{1}H} REDOR dephasing curves of Carbon 1 and Carbon 2 are also simulated for the vdW-DF2 relaxed structure and shown in Figure 4.12. The close match of the ^{13}C{^{1}H} REDOR dephasing of Carbon 1 and Carbon 2 calculated using the atomic coordinates from vdW-DF2 relaxed geometry with experimental data suggests that hydrogen positions are more accurately represented by this functional compared with GGA-PBE and the XRD crystal structure.

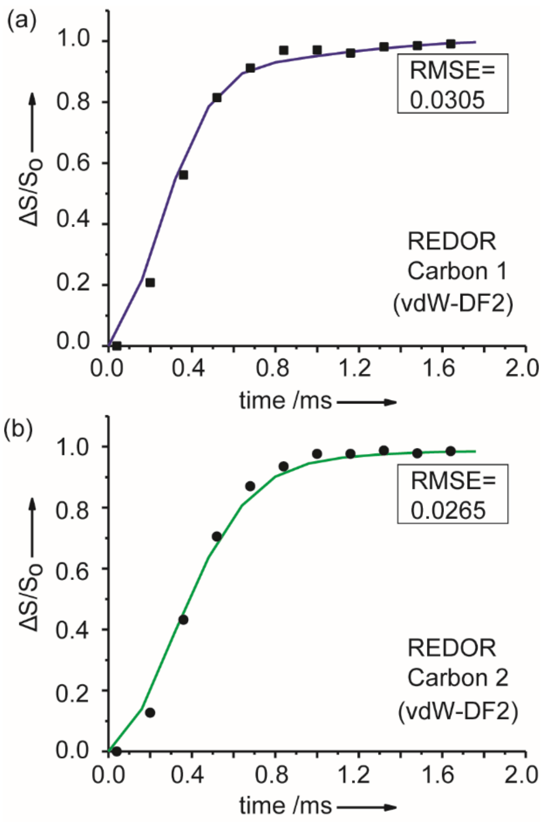

Figure 4.12 $^{13}C\{^1H\}$ REDOR NMR data (black squares and circles for Carbon 1 and Carbon 2, respectively) and calculated dephasing for (a) Carbon 1 at 163 ppm (blue line) and (b) Carbon 2 at 165.3 ppm (green line). The $^{13}C\{^1H\}$ REDOR simulations use atomic coordinates from relaxed crystal structure using vdW-DF2 functional RMSE values are given in the legend, comparing the agreement of the calculated REDOR curve to the experimental data.

4.3.6 Comparison between Experimental XRD curve and Prediction

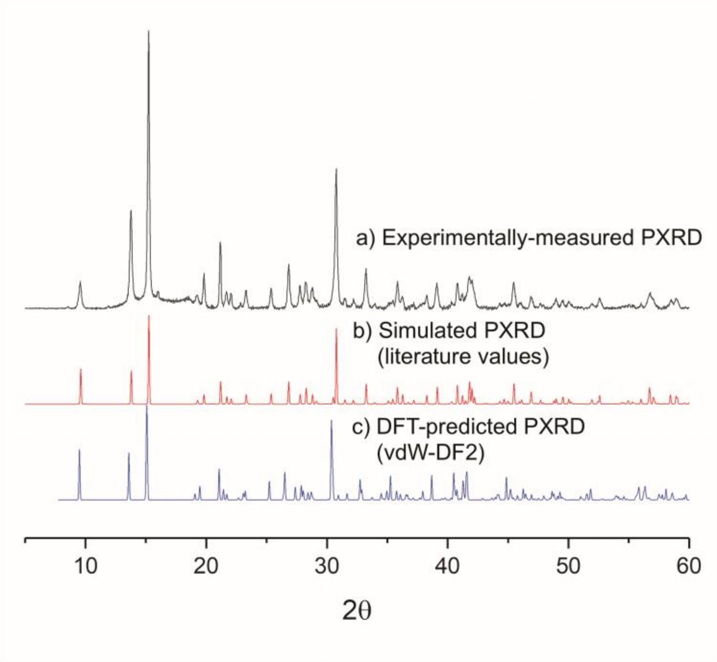

Figure 4.13 Comparison of powder-X-ray diffraction (PXRD) patterns: a) experimentally measured PXRD data (shown in black), and simulated powder patterns b) for the atomic coordinates determined from a published structure of hydromagnesite "Simulated PXRD (literature values)" (shown in red), and c) for the VASP calculation from the structure relaxation using the vdW-DF2 functional "DFT-predicted powder diffraction (vdW-DF2)" (shown in blue). The CrystalMaker program was used to generate simulated PXRD patterns.

In the computation, the unit cell and atomic coordinates are allowed to be relaxed for geometry optimization. Consequently, it is better to compare the prediction of PXRD after geometry optimization with the experimental XRD pattern. Figure 4.13 shows the comparison of PXRD among experiment (room temperature), simulated PXRD from the published XRD structure, and simulated PXRD using atomic coordinates from the vdW-DF2 functional optimized structure (0 K). The results indicate there is good agreement between the optimized structure using vdW-DF2 functionals and experimental data.

Meanwhile, the lattice parameter differences are also considered in the comparison. In Table 4.3, we show the lattice parameter values, including a, b and c. In previous studies, less than 2% alteration is expected to be reasonable for comparison between experiment and DFT computations. In our results, the lattice changes of vdW-DF2 is less than 2% for each lattice parameter.[135,136] By comparison, the difference of lattice parameter b is around 2.7% for GGA-PBE relaxed structure, showing those coordinates are not as good as of a match.

Table 4.3 Lattice parameters (Å) from the powder XRD and DFT calculations.

	Crystal structure (Ref. 4) at room temperature from powder XRD	DFT-predicted atomic coordinates (vdW-DF2) at 0 Kelvin	DFT-predicted atomic coordinates (GGA-PBE) at 0 Kelvin
a*	8.378 Å	8.431 Å (0.63%)	8.421 Å (0.51%)
b	8.954 Å	9.115 Å (1.80%)	9.198 Å (2.73%)
c*	10.105 Å	10.184 Å (0.78%)	10.146 Å (0.41%)

Percent error is indicated in parentheses. * Lattice parameter a and c are interchanged to match the output of VASP, as described in the text (sextion)

4.3.7 Comparison of vdW-DF2, GGA-PBE Optimized Structures and XRD Crystal Structure

Here, we have a unique opportunity with hydromagnesite, because there are two magnetically inequivalent carbon sites that have multiple interstitial water molecules (in common), the effects of which are encoded in both the CSA and ^{13}C-^{1}H distance measurement by NMR. Atomic coordinates should yield good agreement for the ^{13}C-^{1}H distances of all nearby H_2O and OH^- species (by ^{13}C{^{1}H} REDOR), and the spatial arrangement of these moieties will be accurately reflected by the CSA lineshapes.

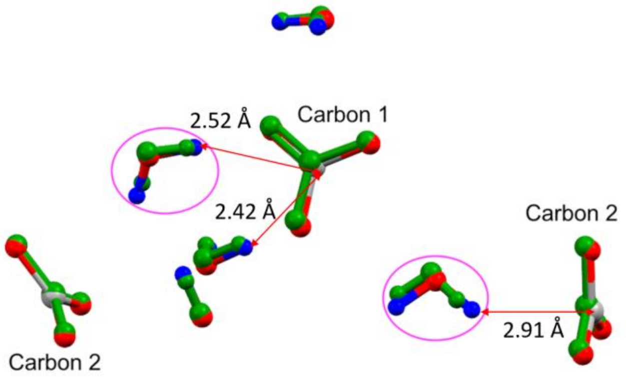

Figure 4.14 Graphical depiction of differences in atomic coordinates between published XRD structure of hydromagnesite (ICSD 920)[127] (shown in green) and VASP-computed (vdW-DF2 functional) atomic coordinates, where carbon is gray, oxygen is red, and hydrogen is blue. The two circled water molecules show the largest change and interact with both carbons, such that a deflection of the position of H_2O influences both carbonate sites. A distance between protons and carbon are shown in the picture for vdW-DF2 functional optimized structure.

The difference in atomic coordinates from the published XRD structure to that predicted by vdW-DF2 is depicted in Figure 4.14. The multi-color structure is the vdW-DF2 predicted structure, and shown in green is the X-ray crystal structure (ICSD 920). While the carbonates (shown in red and gray) have only small deviations in their atomic coordinates, several of the hydrogens (shown in blue) move substantially. There are displacements of up to 0.34 Å between hydrogen coordinates, when comparing the two structures.

When the H_2O positions are adjusted using the model provided by the vdW-DF2 relaxed structure, the calculated $^{13}C\{^1H\}$ REDOR curves have better agreement with the experimental data. The vdW-DF2-relaxed structure brings several H_2O species into closer proximity with Carbon 2. Notably, the CSA lineshape for Carbon 2 does not deviate substantially, though $^{13}C\{^1H\}$ REDOR dephasing is affected. For Carbon 1 however, the ^{13}C CSA lineshape is strongly influenced by the movement of water in close proximity to it, leading to both an adjusted CSA lineshape and REDOR dephasing behavior. Ultimately, the new positions of all the surrounding species, lead to a better agreement in both $^{13}C\{^1H\}$ REDOR and ^{13}C CSA lineshape data for both carbon sites. A comparison of distances between the 9 hydrogens near to Carbon 1 and Carbon 2 is summarized in Table 4.4.

Table 4.4 Distances between the 9 hydrogens and carbons in hydromagnesite surrounding Carbon 1 and Carbon 2 from the X-ray crystal structure, and VASP calculations from relaxations using the GGA-PBE functional and vdW-DF2 functional. Hydrogens surrounding Carbon 1 are numbered, and those surround Carbon 2 are lettered. Hydrogens are all from H_2O unless noted for hydroxide (H3 and Hg)

	X-ray Diffraction		GGA-PBE		vdW-DF2	
	Internuclear pair	Bond Distance (Å)	Internuclear pair	Bond Distance (Å)	Internuclear pair	Bond Distance (Å)
Carbon 1	C1-H1	3.52	C1-H1	3.61	C1-H1	3.73
	C1-H2	2.62	C1-H2	2.41	C1-H2	2.52
	C1-H3 (OH^-)	3.81	C1-H3 (OH^-)	3.78	C1-H3 (OH^-)	3.78
	C1-H4	2.49	C1-H4	2.41	C1-H4	2.42
	C1-H5	3.60	C1-H5	3.66	C1-H5	3.67
	C1-H6	3.30	C1-H6	3.37	C1-H6	3.41
	C1-H7	3.90	C1-H7	3.86	C1-H7	4.08
	C1-H8	4.20	C1-H8	4.49	C1-H8	4.46
	C1-H9	3.38	C1-H9	3.45	C1-H9	3.42
Carbon 2	C2-Ha	3.27	C2-Ha	3.27	C2-Ha	3.22
	C2-Hb	4.23	C2-Hb	4.23	C2-Hb	4.16
	C2-Hc	4.42	C2-Hc	4.52	C2-Hc	4.56
	C2-Hd	3.45	C2-Hd	3.57	C2-Hd	3.53
	C2-He	3.11	C2-He	2.99	C2-He	2.91
	C2-Hf	4.13	C2-Hf	4.44	C2-Hf	4.34
	C2-Hg (OH^-)	2.80	C2-Hg (OH^-)	2.72	C2-Hg (OH^-)	2.76
	C2-Hh	4.11	C2-Hh	4.33	C2-Hh	4.22
	C2-Hi	3.14	C2-Hi	3.20	C2-Hi	3.14

4.4 Conclusions

In summary, NMR as “a crystallographic refinement tool” can provide significant insight into molecular structure, especially in hydrated systems such as hydromagnesite. The combination of ^{13}C{^{1}H} REDOR to measure ^{13}C-^{1}H distances and the ^{13}C static CSA lineshapes to determine tensor values is a powerful way to probe local structures. When used in combination with DFT calculations, an accurate map of hydrogen positions can be obtained.^{13}C static NMR spectra of carbonate minerals can yield insight into the organization of chemical entities such as H_2O and OH^- around a carbonate group through their influence on the ^{13}C tensor—reflected in both the isotropic chemical shift and the value for η_{CSA}. Measurement of ^{13}C-^{1}H dipolar couplings with ^{13}C{^{1}H} REDOR in minerals such as hydromagnesite is feasible for probing ^{13}C-^{1}H distances because the protons are sufficiently isolated to not be broadened by ^{1}H-^{1}H homonuclear dipole-dipole interactions. Multiple hydrogens differ in position by as much as 0.34 Å between XRD and NMR-predicted structures. The work presented here demonstrates how the combination of XRD, SSNMR (chemical shift anisotropy and dipole-dipole coupling), and computational chemistry leads to improved determinations of hydrogen atomic coordinates.

In addition, since many chemical properties are dependent on a material’s structure, there is an urgent need for improvement in the accuracy of computations. An important benefit of this NMR crystallography study is the ability to demonstrate the efficacy of different DFT functionals, ultimately to implement improved computational tools when dispersive bonding interactions need to be considered. Such interactions govern not only hydrated minerals and materials, but also biological materials.

4.5 Acknowledgements

This work is supported by the U.S. National Science Foundation (NSF), Award Number 1640899. This work made use of computational resources provided by the Extreme Science and Engineering Discovery Environment (XSEDE), which is supported by the NSF (ACI-1053575), as well as the Savio computational cluster resource provided by the Berkeley Research Computing program at the University of California, Berkeley. A portion of this work was performed at the National High Magnetic Field Laboratory, which is supported by the NSF (DMR-1644779) and the State of Florida.

Chapter 5: NMR Crystallography Study of Nesquehonite - Implication for the Chemical Formula

5.1 Introduction

Nesquehonite is one of several magnesium carbonate minerals that are the products for geological carbon dioxide sequestration reactions.[137,138] There are about 470 papers and patents studying the properties and application of nesquehonite according to Scifinder.[139–141] The chemical formula of nesquehonite has been a controversial issue since 1890,[142] debated to be $MgCO_3 \cdot 3H_2O$[128,143–145] or $Mg(HCO_3)(OH) \cdot 2H_2O$[146,147]. Some studies have used infrared spectroscopy (IR), Raman spectroscopy, and thermogravimetric analysis (TGA) to determine the presence of bicarbonate and hydroxide.[146–148] However, the bicarbonate and hydroxide were not observed in a similar study that also used IR and Raman spectroscopy.[149] Additional X-ray diffraction (XRD) studies for structure refinement did not show the presence of bicarbonate or hydroxide.[128,145] In 2015, G. Jauffret et al. indicated that previous investigations proposing the chemical formula for nesquehonite, $Mg(HCO_3)(OH) \cdot 2H_2O$, could be wrong due to a temperature-induced phase change.[150] Until now, there remains an ongoing debate about the true chemical formula of nesquehonite.

In this study, we apply NMR crystallography to resolve the controversial chemical formula for nesquehonite. The $^{13}C\{^1H\}$ REDOR experiment introduces the ability to distinguish bicarbonate and carbonate in the solid-state sample. NMR enables a better understanding of the structures of hydrated materials or organic/biological samples.

5.2 Experimental methods

5.2.1 Preparation of 10% ^{13}C Enriched Nesquehonite

10% ^{13}C enriched nesquehonite was synthesized by adding 0.044g of 98% ^{13}C-enriched $NaH^{13}CO_3$ and 0.394g natural abundance $NaHCO_3$ to a solution of 1.050g $MgCl_2 \cdot 6H_2O$ in 9.18 ml of de-ionized (DI) water.[91] After 1 min. of mixing, the solution was sealed and kept at room temperature for three days. The precipitate was then rinsed with DI water and dried under vacuum oven at 40°C for 10 mins. The powder was air-dried overnight. The rinsing and drying process was repeated twice to remove impurities in the sample.

5.2.2 Powder XRD

Powder X-ray diffraction (PXRD) of the 10% ^{13}C enriched nesquehonite was obtained with a Bruker d8 Advance X-ray diffractometer using Cu-Kα radiation at 40 kV and 40 mA. The sample was held in a Plexiglas PXRD slide. Data were collected over a 2θ range from 5° to 90° with a step size of 0.019°. The PXRD pattern of the synthesized sample is shown in Figure 5.1 along with the reference pattern of nesquehonite[128] (ICSD 91710).

5.2.3 Solid-State NMR

Static ^{13}C (74.18 MHz) NMR spectra with ^{1}H (294.97 MHz) decoupling were collected in an Oxford superconducting 7.05 T magnet with a Tecmag (Houston, TX) console equipped with a Chemagnetics 4 mm MAS HXY probe. ^{13}C spectra were acquired using a Hahn-echo pulse sequence [28,111]($\pi/2$-τ-π-τ-echo) with a $\pi/2$-pulse of 4 μs, a π-pulse of 8 μs, and a τ delay of 30 μs.

1440 transients were recorded with a recycle delay of 180 s, which is approximately five times of the spin-lattice relaxation time.[91] ^{1}H decoupling was applied with an RF power of ν_{RF} = 42 kHz. The static ^{13}C NMR spectrum was fit using Dmfit[112] to obtain principal values of the chemical shift tensor: δ_{xx}, δ_{yy} and δ_{zz}, which are reported using the Haeberlen convention.[20]

^{13}C (148.34 MHz) and ^{1}H (589.84 MHz) NMR spectra with MAS were recorded on a 13.8 T Oxford superconducting magnet using a Bruker 2.5 mm HX MAS probe. ^{1}H MAS NMR spectra were acquired using a rotor-synchronized Hahn-echo with a $\pi/2$-pulse length of 6 μs, π-pulse length of 12 μs, MAS rotation frequency (ν_r) of 25 kHz, and a τ delay of 31 μs to center the π-pulse at the middle of the rotor period. ^{1}H MAS spectra were recorded with 8 transients and a 10 s recycle delay. $^{13}C\{^{1}H\}$ CPMAS spectra were acquired with an initial ^{1}H $\pi/2$ pulse width of 3.4 μs, ^{1}H-^{13}C cross-polarization Hartman-Hahn contact time of 2 ms, 64 transients, and a recycle delay of 10 s. The MAS rotational frequency was maintained at 25 kHz with a Tecmag MAS controller.

$^{13}C\{^{1}H\}$ REDOR[29] measurements were acquired with ^{13}C π-pulse widths of 15 μs and ^{1}H π-pulse widths of 7.5 μs. Observe spin (^{13}C) refocusing pulses were centered every rotor period, and dephasing (^{1}H) pulses were centered halfway through the rotor period for maximum dephasing. (It is as same as to the Figure 4.8). XY-4 phase cycling of the rotor-synchronized ^{13}C and ^{1}H π-pulses was used to minimize artifacts from RF-inhomogeneity and resonance frequency offsets during the REDOR evolution time.[113] The MAS rotational frequency was maintained at 25 kHz with a Tecmag MAS controller.

For all NMR experiments, ^{13}C chemical shifts were referenced to adamantane as an external secondary reference with the $^{13}CH_2$ resonance set to 38.48 ppm. ^{1}H chemical shifts were referenced to liquid tetramethylsilane (TMS) at 0 ppm.

$^{13}C\{^{1}H\}$REDOR simulations of the 11-spin systems (1 carbon and 10 nearest hydrogens) were carried out using SIMPSON[114]. The maximum time step (max dt) over which the Hamiltonian is approximated to be time-independent was set to 1 μs in SIMPSON. XY-4 phase cycling of the rotor-synchronized ^{13}C and ^{1}H π-pulses was used to simulate the real experiment. Finite pulse widths were assumed. All calculations contained negligible imaginary contributions, and the initial amplitudes of the real parts were taken for REDOR analyses. Data convergence was checked by repeating selected calculations using smaller max dt and more extensive powder averaging schemes. RMSE values are computed between the experimental data and the REDOR curve and are denoted to assess the quality of the match.

5.2.4 DFT Calculations

All of the DFT calculations were performed using the Vienna ab initio simulation package (VASP)[115], versions 5.3.5 and 5.4.4.18Apr17-6-g9f103f2a35. These calculations made use of the projector-augmented wave (PAW) method[116,117] and Perdew−Burke−Ernzerhof (PBE)[59] GGA based potentials from the VASP library. All calculations were non-spin-polarized. In the structural optimizations, use was made of the PBE-GGA, as well as two different functionals incorporating van der Waals (vdW) interactions within DFT, which are the vdW-DF[118–120] and vdW-DF2 [118–121] functionals.

The electronic wave functions were expanded in a plane-wave basis set, using a kinetic-energy cutoff of 610 eV. In the structure optimization calculations, cell parameters and atomic positions were relaxed until the components of the stress tensor were less than 0.1 kbar, and the force on each atom was less than 0.001 eV/Å in magnitude. During the structural relaxations of the nesquehonite compound (which has a finite bandgap), the sampling of the Brillouin zone was performed using the tetrahedron method with Blöchl corrections and a k-point density of 3x2x1.[122]

The calculation of NMR chemical shifts made use of the linear response formalism[124,125] implemented in VASP. In these calculations, a Gaussian smearing was used of 0.1 eV set to ensure negligible partial occupancies of the electronic states. Convergence was tested for the k-point grid, the real-space grid, and the plane wave cutoff. Using higher levels of convergence only led to small changes in calculated NMR CSA parameters: the largest variation in η_{CSA} was 0.002, and the largest variation in δ_{iso} or ζ_{δ} was 1 ppm.

The vdW-DF functional was found to yield the best agreement with experimental measurements and is the focus of the calculation results presented in the main text.

5.3 Results and Discussion

5.3.1 XRD of Synthesized Hydromagnesite

The powder XRD (PXRD) pattern of lab-synthesized nesquehonite is shown in Figure 5.1, along with the reference pattern of nesquehonite[128] (ICSD 91710). There is good agreement between the powder XRD (PXRD) pattern of the synthesized sample (with 10% ^{13}C enrichment) and that of the reference, indicating that nesquehonite is formed with no other phases of hydrated magnesium carbonate.

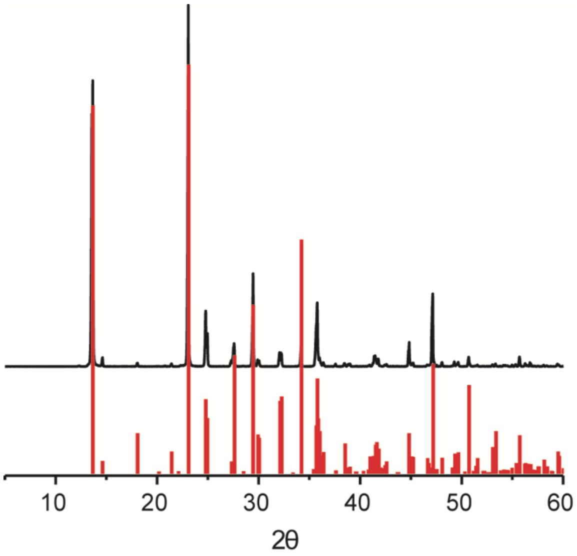

Figure 5.1 Powder XRD characterization of synthesized nesquehonite. The top (black) diffraction pattern is experimental data, and the bottom (red) pattern is the nesquehonite reference diffraction pattern.(ICSD 91710)

5.3.2 ^{13}C CPMAS NMR and ^{1}H MAS NMR

Consistent with prior results[91], only one ^{13}C NMR resonance is observed (Figure 5.2a) with an isotropic chemical shift of 165.2 ppm, which is consistent with the single carbon site present in the XRD crystal structure of nesquehonite published by Giester.[128] In Figure 5.2b, a single ^{1}H resonance is observed in the ^{1}H spin-echo MAS NMR spectrum at 6.0 ppm, which is assigned to H_2O.[129] There is no obvious evidence of the existence of hydroxide according to the ^{1}H MAS NMR.

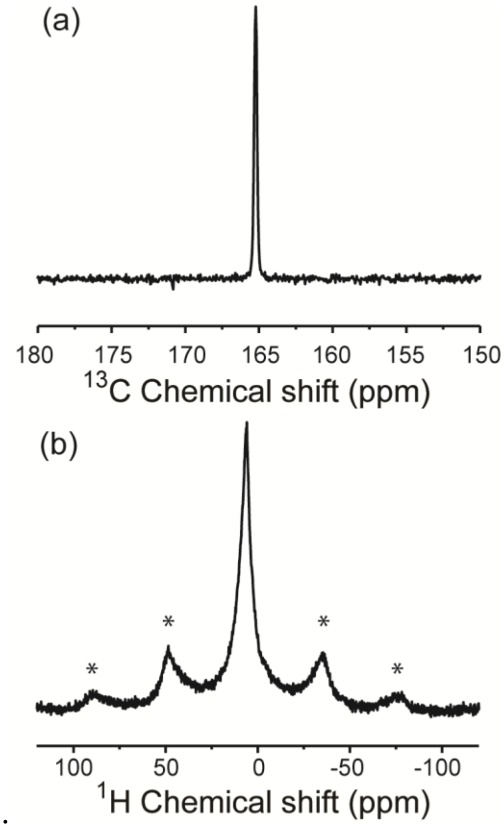

Figure 5.2 SSNMR of 10 % ^{13}C-enriched nesquehonite powder. (a) $^{13}C\{^{1}H\}$ CPMAS (ν_r=25 kHz), and (b) ^{1}H rotor-synchronized Hahn echo MAS (ν_r=25 kHz). * denotes spinning sidebands of H_2O.

The crystal structure of nesquehonite published by Giester (2000) is shown in Figure 5.3. In the crystal structure of nesquehonite, there is only one chemically distinct carbon site and there is a question in the literature as to whether it is a carbonate or a bicarbonate.[146] However, to distinguish bicarbonate from carbonate merely from its ^{13}C isotropic chemical shift may be precarious, since the isotropic chemical shift of either bicarbonate or carbonate can be anywhere in the range between 160 and169 ppm depending on the pH.[151]

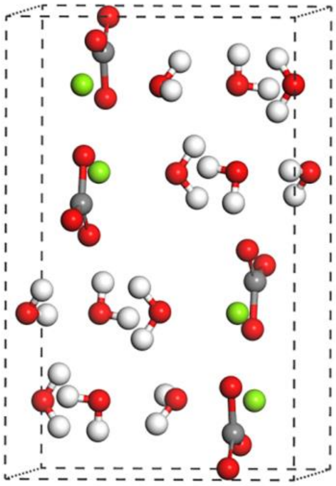

Figure 5.3 Crystal structure of nesquehonite. Magnesium is shown in green (spheres), oxygen is red, hydrogen is white, and carbon is gray.

5.3.3 Static ^{13}C NMR and Slow Spinning ^{13}C{^{1}H} CPMAS NMR

The static ^{13}C NMR spectrum (with ^{1}H decoupling) at 7.05T for 10% ^{13}C-enriched nesquehonite is shown in Figure 5.4 (in black). Using the 2008 IUPAC conventions[130] (that derive from the Haeberlen convention[20]), we can describe the CSA lineshape by algebraic expression from elements of the diagonalized chemical shift tensor: the asymmetry parameter (η_{CSA}), isotropic chemical shift (δ_{iso}) and reduced anisotropic chemical shift (δ_{aniso}), which was discussed in Chapter 4. Deconvolution of the static ^{13}C NMR

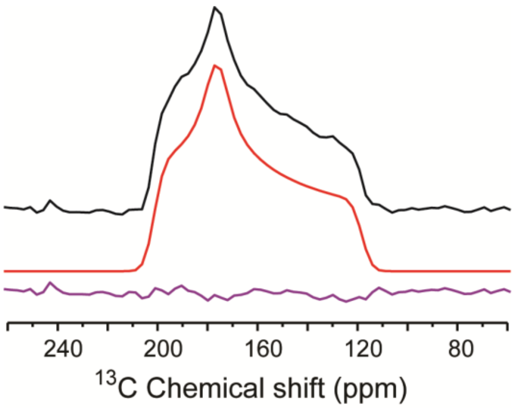

Figure 5.4 Static ^{13}C (with ^{1}H decoupling) NMR spectrum of nesquehonite. Experimental ^{13}C lineshape is shown in black, simulated CSA-broadened lineshape is shown in red, the difference between experimental data and simulation is shown in purple.

spectrum is performed with Dmfit (Figure 5.4). The fitting of static ^{13}C NMR of nesquehonite yields a η_{CSA} value of 0.54 and δ_{aniso} value of -47.09 ppm. The η_{CSA} value of 0.54 indicates a relatively asymmetric local environment for carbon in nesquehonite, meaning the site lacks a high symmetry rotation axis, such as the C_3 of carbonate. However, such asymmetry could be due to two possibilities: one is from water creating a distortion around carbonate, and another is that the species is bicarbonate. Thus, it is impossible to distinguish the chemical formula for nesquehonite just from the static ^{13}C lineshape.

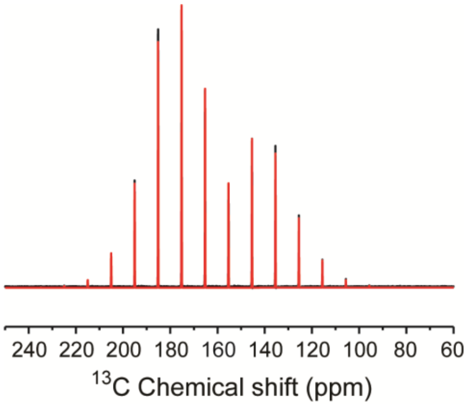

Figure 5.5 Slow spinning ^{13}C{^{1}H} CPMAS NMR (ν_r = 2 kHz) of nesquehonite and the simulation of the spectrum by Dmfit. Experimental ^{13}C spectrum is shown in black, and the simulation is shown in red. The η_{CSA} and the δ_{aniso} of carbon is 0.53 and -48.4 ± 0.1 ppm, respectively.

Slow spinning $^{13}C\{^{1}H\}$ CPMAS NMR of nesquehonite ($\nu_{rotation}$ = 2 kHz) and the simulation of the spectrum are also shown in Figure 5.5 as evidence to confirm the η_{CSA} and reduced δ_{aniso} value for ^{13}C. Experimental ^{13}C data are shown in black, and the simulation is shown in red. The η_{CSA} of ^{13}C in nesquehonite from slow spinning $^{13}C\{^{1}H\}$ CPMAS is 0.53 and δ_{aniso} is 48.40 ppm. Three elements of the diagonalized chemical shift tensor determined by static ^{13}C NMR and slow spinning $^{13}C\{^{1}H\}$ CPMAS NMR are summarized in Table 5.1. There is good agreement between static ^{13}C NMR and slow spinning $^{13}C\{^{1}H\}$ CPMAS NMR for the three values in nesquehonite. We will use the CSA parameters from static ^{13}C NMR for discussion later.

Table 5.1 ^{13}C chemical shift tensor elements determined from slow spinning (ν_r = 2 kHz) $^{13}C\{^{1}H\}$ CPMAS NMR and static NMR for nesquehonite

	δ_{11} (ppm)* δ_{XX} (ppm)	δ_{22} (ppm)* δ_{YY} (ppm)	δ_{33} (ppm)* δ_{ZZ} (ppm)
Slow MAS NMR	202.2	176.6	116.8
Static NMR	201.5	176.0	118.1

*we are presenting both “standard” notation δ_{11}, δ_{22} and δ_{33}, (ordered by frequency from high to low) and the Haeberlen notation δ_{XX}, δ_{YY} and δ_{ZZ}, (where $| \delta_{ZZ} - \delta_{iso} | \geq | \delta_{XX} - \delta_{iso} | \geq | \delta_{YY} - \delta_{iso} | \geq$) for the diagonalized chemical shift tensor values.

5.3.4 $^{13}C\{^{1}H\}$ REDOR and SIMPSON Simulation

It is not reliable to discriminate the chemical formula of nesquehonite from $MgCO_3 \cdot 3H_2O$ to $Mg(HCO_3)(OH) \cdot 2H_2O$ merely by the ^{13}C NMR isotropic chemical shift. Thus, complementary information from the the ^{1}H-^{13}C distance was sought by measuring the ^{13}C-^{1}H heteronuclear dipolar coupling using the NMR sequence, $^{13}C\{^{1}H\}$ REDOR. [132–134]

$^{13}C\{^{1}H\}$ REDOR data is collected in two sets of experiments (same pulse sequence as shown in Figure 4.6): a full-echo (S_o) spectrum with rotor-synchronized π-pulses on the ^{13}C observe spin to account for the effects of T_2 relaxation, and the S spectrum with dephasing π-pulses on the ^{1}H

channel, which reintroduces the ^{13}C-^{1}H dipolar coupling. The intensity difference ($\Delta S = S_o - S$) between the full-echo (S_o) and the dephased (S) spectra reflects the ^{1}H-^{13}C dipolar coupling. S_o and S spectra were deconvoluted with Dmfit. Figure. 5.6 shows $^{13}C\{^{1}H\}$ REDOR dephasing ($\Delta S/S_o$) as a function of REDOR evolution time for carbon (black squares) in nesquehonite.

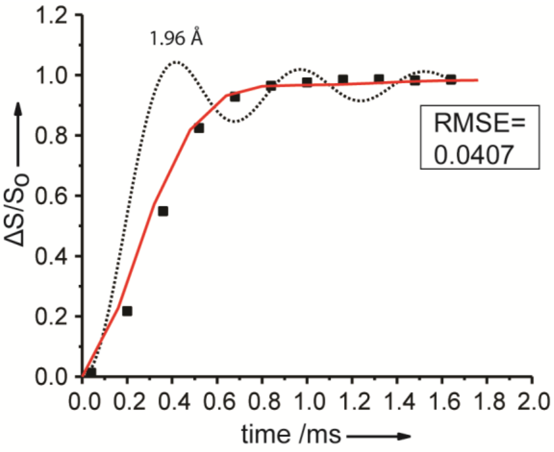

Figure 5.6 $^{13}C\{^{1}H\}$ REDOR NMR data black squares and the simulation curve (red curve). The $^{13}C\{^{1}H\}$ REDOR simulation uses atomic coordinates from the DFT (GGA-PBE functional) optimized structure. The dashed line represents the $^{13}C\{^{1}H\}$ REDOR simulation curve between one spin pair, with an internuclear distance of 1.96 Å. RMSE value of simulation REDOR curve of GGA-PBE functional optimized structure is 0.0407.

The $^{13}C\{^{1}H\}$ REDOR curves were also simulated with SIMPSON[152] using the positions of the ten closest protons specified by the DFT-optimized crystal structure. DFT optimization was made in the Vienna Ab-initio Simulation Program (VASP)[115] using the GGA-PBE functional,[59] which has worked well for solid-state systems in the last twenty years.[60,61] The atomic coordinates of published crystal structure of nesquehonite ($MgCO_3 \cdot 3H_2O$) was imported into VASP for DFT optimization.[128]

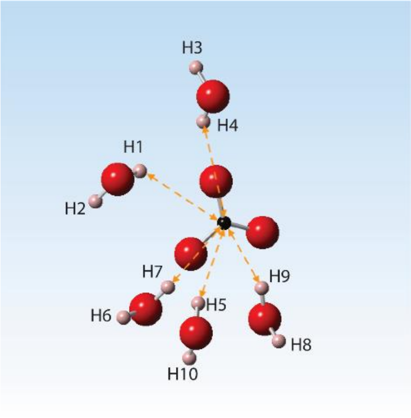

Figure 5.7 Positions of the ten hydrogens (shown in pink) from the GGA-PBE functional optimized structure used in the calculation of REDOR dephasing. Oxygens are colored red. Distances of the five closest protons are exhibited by dashed lines in the picture.

Once an optimized structure is obtained, the 10 close hydrogens (5 closest protons from the surrounding water, and plus 5 hydrogens in same water molecules) around one carbon (11 nuclei total in the simulation, shown in Figure 5.7) are imported to SIMPSON[152] to simulate the $^{13}C\{^{1}H\}$ REDOR curve.

The simulated $^{13}C\{^{1}H\}$ REDOR curve from atomic coordinates optimized using the GGA-PBE functional (solid red curve in Figure 5.6) exhibits an overall shape that agrees relatively well to the experimental data (black squares). In nesquehonite, the first initial decay results from dipolar coupling between carbon and the nearest hydrogens, which have distances of 2.49, 2.67 and 2.71 Å in nearby water molecules. The $^{13}C\{^{1}H\}$ REDOR curve is consistent with the crystal structure of nesquehonite being $MgCO_3 \cdot 3H_2O$. Also, a simulated $^{13}C\{^{1}H\}$ REDOR curve of a single ^{13}C-^{1}H spin pair, with a distance of value of 1.96 Å, is also shown in Figure 5.6 to test the other model structure. If the chemical formula of nesquehonite is $Mg(HCO_3)(OH) \cdot 2H_2O$, the closest distance between carbon and proton will be around 1.96 Å for HCO_3^- (typical distance in an HCO_3^- structure). This shorter distance should dominate the initial slope of the REDOR curve, which would adopt a sharper initial dephasing behavior than the experimental data shown here.

The discrepancy between this simulation of REDOR with one spin pair and experimental data allows us to rejects the chemical formula of $Mg(HCO_3)(OH)\cdot 2H_2O$. Additionally, the chemical formula of $Mg(HCO_3)(OH)\cdot 2H_2O$ is not reasonable from an NMR perspective, because there is no ^1H resonance for OH^- observed in the ^1H MAS NMR. Here, we can safely conclude that SSNMR is a powerful tool to directly distinguish bicarbonate and carbonate by measuring the ^1H-^{13}C dipolar coupling strength through $^{13}C\{^1H\}$ REDOR, and we conclude the chemical formula of nesquehonite is $MgCO_3\cdot 3H_2O$.

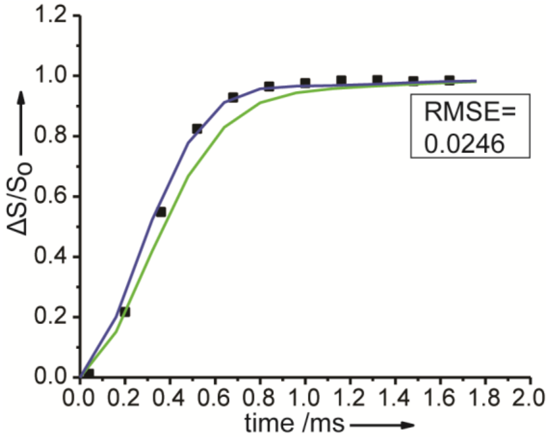

Figure 5.8 $^{13}C\{^1H\}$ REDOR NMR data black squares and simulation curve use atomic coordinates from vdW-DF functional optimized structure (blue curve) and X-ray diffraction (XRD) measurements (green curve). RMSE value of simulation REDOR curve of vdW-DF functional optimized structure is 0.0246 and 0.0522 for XRD structure.

However, although the overall shape of simulated $^{13}C\{^1H\}$ REDOR (red curve, Figure 5.6) of nesquehonite ($MgCO_3\cdot 3H_2O$) shows good agreement with experimental data, the initial slope of the simulated REDOR dephasing curve still exhibits a slight deviation from that found by experiment. This discrepancy suggests that the proton coordinates surrounding the carbon could be improved using refinement by NMR ("NMR crystallography").[48,153,154] Thus, besides confirmation of the chemical formula of nesquehonite, the combination of $^{13}C\{^1H\}$ REDOR and DFT computation can be used to improve the protons' position, which is similar to the previous study of hydromagnesite.[153] To improve the protons' location, in this study, van der Waals interactions within VASP density functional theory computations (vdW-DF) and version 2 (vdW-DF2) are used to optimize the structure, instead of the GGA-PBE functional.[118,120,155] It is found that the simulations of $^{13}C\{^{1}H\}$ REDOR curves from the vdW-DF and vdW-DF2 optimized structure are almost the same. Thus, only the simulation of $^{13}C\{^{1}H\}$ REDOR curve from the optimized structure using the vdW-DF functional is shown here in Figure 5.8. After optimization, the closest hydrogen distances become 2.54, 2.77 and 2.79 Å, instead of 2.49, 2.67 and 2.71 Å. It is found that simulation of $^{13}C\{^{1}H\}$ REDOR curve has a slightly better prediction (RMSE of 0.0246) compared with the GGA-PBE functional (RMSE of 0.0407).

A simulation of $^{13}C\{^{1}H\}$ REDOR curve generated from the XRD structure (without any geometry optimization) is also shown in Figure 5.8 (green line) as a reference. The simulated REDOR curve from XRD determined atomic coordinates has a worse match to the experimental data than the optimized structure using either the GGA-PBE or vdW-DF functional.

Table 5.2 Distance between closest hydrogens to carbon in nesquehonite from XRD atomic coordinates and atomic structures derived from DFT relaxation using different functionals. The labels of protons are shown in Figure 5.7.

Hydrogen Label	XRD	GGA-PBE	vdW-DF
	Bond distance (Å)		
H1	3.127	3.113	3.129
H2	3.734	3.877	3.896
H3	4.555	4.646	4.714
H4	3.465	3.320	3.421
H5	2.832	2.675	2.766
H6	3.922	4.050	4.090
H7	2.871	2.708	2.789
H8	3.675	3.884	3.920
H9	2.670	2.487	2.539
H10	4.079	4.109	4.206

The distances of the ten closet protons from the XRD determined crystal structure, GGA-PBE and vdW-DF optimized structures are summarized in Table 5.2. Through simulations of $^{13}C\{^1H\}$ REDOR, we found that DFT optimization by vdW-DF functional can slightly improve the agreement between simulation and experimental data.

5.3.5 Chemical Shift Computation by DFT and Simulation of Static Line-shape

CSA tensors can also be calculated using quantum mechanical methods that reflect the atomic and electronic structure. The results of such calculations depend on the atomic coordinates in crystals, especially the protons' positions around the carbonate in nesquehonite. Thus, the CSA tensors should be used as a standard for NMR crystallography. The experimentally determined CSA parameters from static ^{13}C NMR are shown in Table 5.3. To convert the calculated tensors values to the predicted chemical shift for nesquehonite, a linear relationship between calculated CSA tensor elements and experimentally determined chemical shifts of magnesite and hydro-magnesite is shown in Figure 5.9.

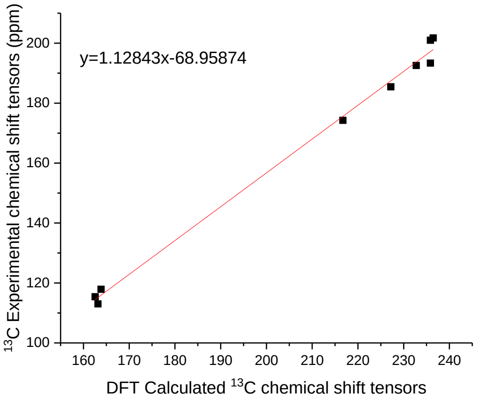

Figure 5.9 Linear rescaling of ^{13}C chemical shift tensor values. Experimentally-measured values of diagonalized tensors are plotted versus VASP calculated values for magnesite ($MgCO_3$) and hydromagnesite ($4MgCO_3.Mg(OH)_2•4H_2O$). The experimental data of magnesite is from a previous publication, and hydromagnesite from the previous chapter.

In Figure 5.9, experimentally determined chemical shift tensors of magnesite ($MgCO_3$) are from a prior publication,[91] and hydromagnesite values are from a recent publication.[153] Because it has been shown the vdW-DF2 functional optimized structure is more accurate, the calculated chemical shift tensor of hydromagnesite from vdW-DF2 optimization is used in the linear relationship. Here, using atomic coordinates from the nesquehonite crystal structure from the published X-ray refinement in the ICSD,[127] Vienna Ab initio Simulation Package (VASP)[115] calculations of the ^{13}C CSA parameters were performed, values given shown in Table 5.3, focusing on isotropic chemical shift (δ_{iso}), values for η_{CSA} and reduces chemical shift anisotropy (δ_{aniso}).

Table 5.3 Experimental and computationally (VASP) determined ^{13}C NMR CSA parameters for nesquehonite using XRD atomic coordinates and atomic structures derived from DFT relaxation using different functionals

Method	δ_{iso} (ppm)	δ_{aniso} (ppm)	η_{CSA}
Exp ^{13}C NMR (Dmfit)	165.2	-47.09	0.54
DFT (XRD)	157.9	-49.80	0.70
DFT (GGA-PBE)	162.5	-50.39	0.58
DFT (vdW-DF)	165.3	-50.69	0.58
DFT (vdW-DF2)	164.5	-52.24	0.57

CSA parameters derived from the GGA-PBE relaxed structure are shown in Table 5.3 (labeled as DFT (GGA-PBE)). Through comparison, the δ_{iso} of carbonate and η_{CSA} through GGA-PBE functional match experimental data better compared to XRD determined atomic coordinates. However, there is still a 2.7 ppm difference for the isotropic chemical shift between GGA-PBE functional optimized structure and experiment.

CSA parameters calculated by DFT using vdW-DF and vdW-DF2 functionals optimized structure are also shown in Table 5.3. They both improve the agreement for δ_{iso} compared with the

XRD determined atomic coordinates or the GGA-PBE functional optimized structure. The overall best agreement with the CSA parameter is obtained using the relaxed geometries obtained from the vdW-DF functional. δ_{iso} is the value known with the standard where good agreement is required. Although η_{CSA} and δ_{aniso} could have slightly errors, these values help us select vdW-DF as the best agreement to experiment.

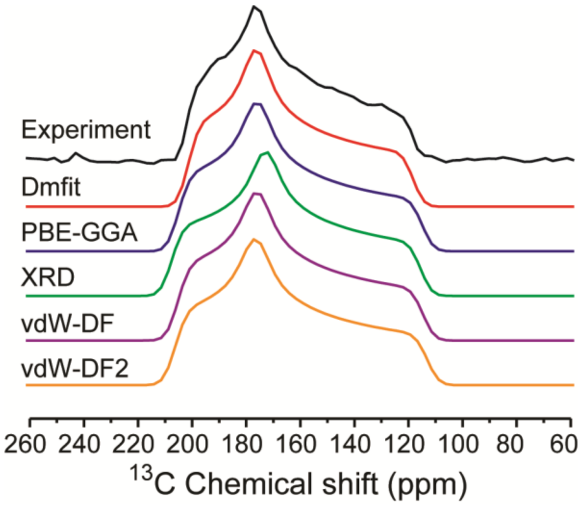

Figure 5.10 Static ^{13}C NMR spectra of nesquehonite from experiment and simulation. Experimental ^{13}C data are shown in black, the simulated CSA-broadened lineshapes for nesquehonite in red. Best fit using Dmfit, denoted "Dmfit"; and simulated from NMR tensors determined from VASP calculations using atomic coordinates from X-ray diffraction, denoted "XRD", from relaxations using the GGA-PBE functional, denoted "GGA-PBE" and from relaxations using the vdW-DF and vdW-DF2 functionals, denoted "vdW-DF" and "vdW-DF2", respectively.

Additionally, the static ^{13}C lineshape can be generated through DFT calculated NMR parameters. In the simulation of the static ^{13}C CSA lineshape, δ_{iso} is constrained to the experimentally-measured value, while the values for η_{CSA} and δ_{aniso} are from DFT predictions. Figure 5.10 displays the deconvolution by Dmfit, along with simulated static ^{13}C lineshapes from DFT calculation using atomic coordinates from X-ray diffraction, from relaxations from using GGA-PBE, vdW-DF and vdW-DF2 functionals. For the XRD crystal structure, the simulation of the static ^{13}C lineshape indicates a higher asymmetry (η_{CSA} =0.7). However, it is also found that there are slight differences in the simulation of ^{13}C static lineshape between GGA-PBE, vdW-DF and vdW-DF2. Therefore, it is decided to explore the three chemical shift tensors from experimental deconvolution, the prediction from XRD atomic coordinates, GGA-PBE, vdW-DF and vdW-DF2 functionals. They are summarized in Table 5.4. RMSE value between the predictions and experimental deconvolution indicates the vdW-DF has the best agreement with the experimental data.

Table 5.4 Experimental and computationally (VASP) determined ^{13}C NMR diagonalized chemical shift tensor values for nesquehonite using XRD atomic coordinates and atomic structures derived from DFT relaxation using different functionals

Method	δ_{XX} δ_{11}	δ_{YY} δ_{22}	δ_{ZZ} δ_{33}	δ_{iso}	RMSE (ppm)
Exp ^{13}C NMR (Dmfit)	201.5	176.0	118.1	165.2	--
DFT (XRD)	200.1	165.4	108.1	157.9	8.47
DFT (GGA-PBE)	202.2	173.2	112.1	162.5	3.87
DFT (vdW-DF)	205.4	175.8	114.6	165.3	3.03
DFT (vdW-DF2)	205.4	175.8	112.3	164.5	4.07

*we are presenting both "standard" notation δ_{11}, δ_{22} and δ_{33}, (ordered by frequency from high to low) and the Haeberlen notation δ_{XX}, δ_{YY} and δ_{ZZ}, (where $| \delta_{ZZ} - \delta_{iso} | \geq | \delta_{XX} - \delta_{iso} | \geq | \delta_{YY} - \delta_{iso} | \geq$) for the diagonalized chemical shift tensor values.

5.3.6 Comparison Between Experimental XRD Curve and Prediction

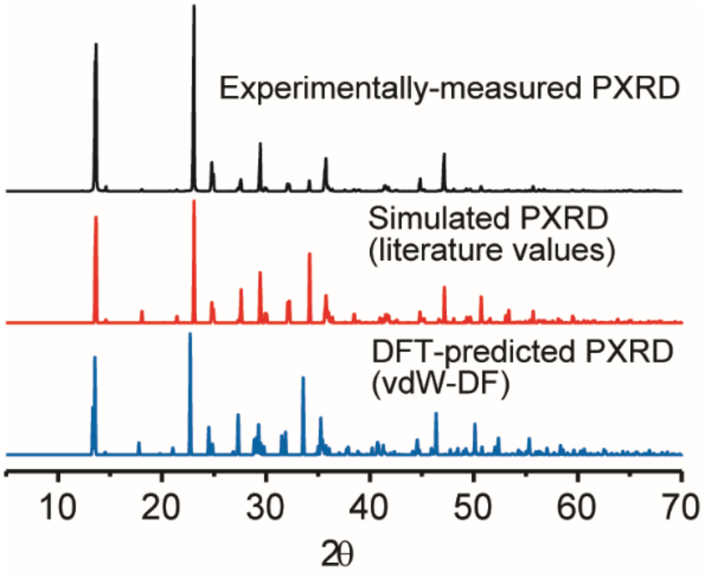

Figure 5.11 Comparison of powder-X-ray diffraction (PXRD) patterns: a) experimentally measured PXRD data (shown in black), and simulated powder patterns b) for the atomic coordinates determined from a published structure of nesquehonite “Simulated PXRD (literature values)” (shown in red), and c) for the VASP calculation from relaxations using the vdW-DF functional “DFT-predicted powder diffraction (vdW-DF)” (shown in blue). The CrystalMaker program was used to generate simulated PXRD patterns.

In the last section, we showed that the vdW-DF functional could lead to a better agreement between simulation and experiment, using the $^{13}C\{^{1}H\}$ REDOR and CSA. However, in the computation, the unit cell and atomic coordinates are optimized from geometry optimization. Consequently, it is reasonable to compare the predicted XRD patterns with the experimental XRD patterns after geometry optimization. Figure 5.11 shows the comparison of powder XRD patterns among experimental data (room temperature), simulated PXRD from the published XRD structure (0 K), and from the geometry-optimized structure using vdW-DF functional (0 K). There is reasonably good agreement between DFT-predicted PXRD using the vdW-DF functional optimized structure and experimental data. In Table 5.5, the lattice parameter changes for each lattice constant, including a, b and c, are presented including the percentage change. Using vdW-DF, the change in each lattice parameter is less than 2%. However, the lattice changes from the GGA-PBE functional is larger than 2% for lattice parameter c. Generally, a bad computation usually change the lattice parameter more than 2%.[135,136]

Table 5.5 Lattice parameters (Å) from the powder XRD and DFT calculation.

	Crystal structure at room temperature from powder XRD	DFT-predicted atomic coordinates (vdW-DF) at 0 Kelvin	DFT-predicted atomic coordinates (GGA-PBE) at 0 Kelvin
a*	5.365 Å	5.466 Å (1.88%)	5.458 Å (1.73%)
b	7.701 Å	7.827 Å (1.64%)	7.784 Å (1.08%)
c*	12.126 Å	12.189 Å (0.52%)	11.851 Å (2.27%)

Percent error is indicated in parentheses. * Lattice parameter a and b are interchanged to match the output of VASP

5.4 Conclusions

In our prior study, the ^{13}C CSA tensor indicates an asymmetric structure, and it is concluded that the chemical formula of $Mg(HCO_3)OH \cdot 2H_2O$ is more accurate, which is also consistent with previous studies of nesquehonite.[146,147] However, under the 25 KHz spinning rate used in this study, the $^{13}C\{^1H\}$ REDOR curve can determine the distances between the surrounding ^1H and ^{13}C. Here, it has been shown that the chemical formula of $MgCO_3 \cdot 3H_2O$ is more reasonable for the $^{13}C\{^1H\}$ REDOR experiment. The asymmetry of the carbonate site (the static ^{13}C NMR lineshape) is due to the proximity of the waters around the CO_3^{2-} group, which distorts the carbonate away from D_{3h} symmetry. The CSA tensors and parameters of carbonate in nesquehonite can also be predicted by DFT after structure optimization. It is also found that the optimized structure using the vdW-DF functional, can be used to better predict CSA parameters, along with a slight improvement for $^{13}C\{^{1}H\}$ REDOR. The combination of static ^{13}C lineshape, $^{13}C\{^{1}H\}$ REDOR, and DFT calculations suggested that the correct chemical formula of nesquehonite is $MgCO_3{\cdot}3H_2O$.

Finally, two major contributions of this study depend on the experimental results and analysis above are summarized as follows:

a) δ_{iso} of ^{13}C NMR is not enough to unambiguously assign carbonate versus bicarbonate. Using a combination of $^{13}C\{^{1}H\}$ REDOR experiment and SIMPSON simulations of DFT optimized crystal structures, those two become distinguishable and favors the chemical formula of nesquehonite is $MgCO_3{\cdot}3H_2O$.

b) The vdW-DF functional can better model weak interactions, such as hydrogen bonding, to improve the predictions of hydrogen positions. This aspect can be experimentally validated by using REDOR NMR and ^{13}C chemical shift tensors. Such solid-state NMR will help to consider the appropriate functionals for structure optimization in the DFT community.

5.5 Acknowledgements

This work is supported by the U.S. National Science Foundation (NSF), Award Number 1640899. This work made use of computational resources provided by the Extreme Science and Engineering Discovery Environment (XSEDE), which is supported by the NSF (ACI-1053575), as well as the Savio computational cluster resource provided by the Berkeley Research Computing

ting program at the University of California, Berkeley. A portion of this work was performed at the National High Magnetic Field Laboratory, which is supported by the NSF (DMR-1644779) and the State of Florida.

Appendix A

CO_2 Mineralization

Fo_{100}_f

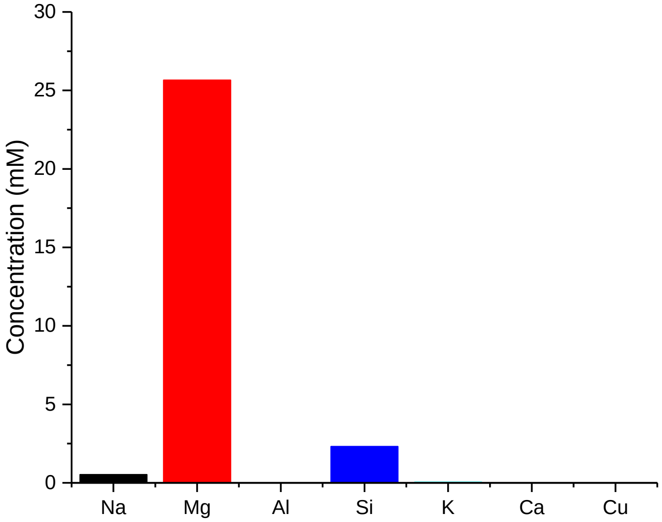

Figure A.1 ICP-MS results of solution from the batch reaction vessel.

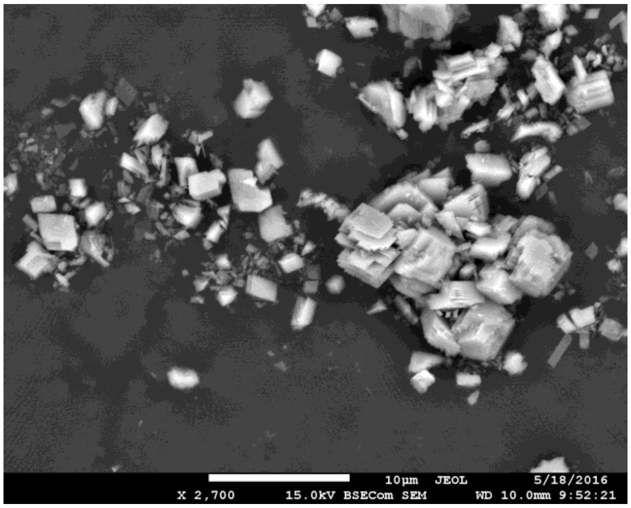

Figure A.2 SEM pictures of magnesite powder in the bottom of batch reaction vessel.

Fo_{100}_fr

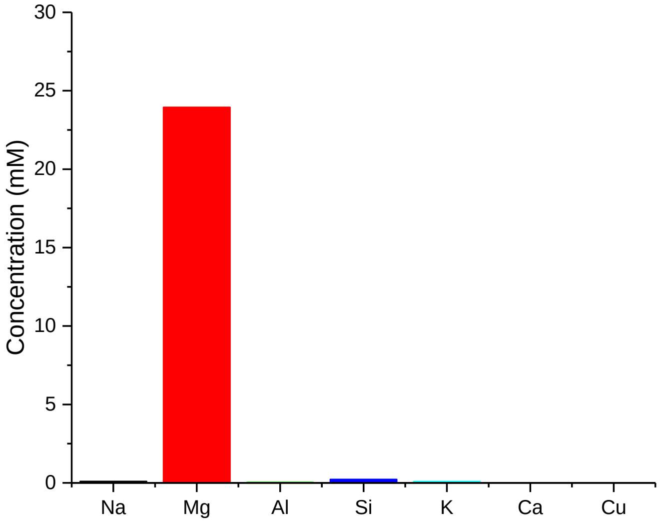

Figure A.3 ICP-MS results of solution from the mixing vessel in flow-through reaction.

Appendix B

Hydromagnesite

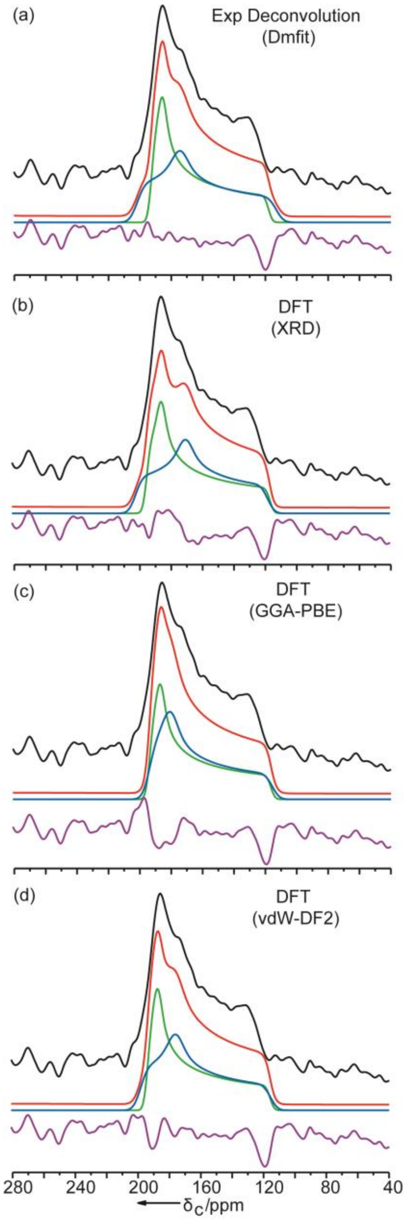

Figure B.1 ^{13}C static NMR spectra of hydromagnesite and computed ^{13}C lineshapes. Experimental ^{13}C data is shown in black, Carbon 1 in blue, Carbon 2 in green, their sum in red, and the residual between experiment and simulation is in purple. Deconvolutions: using Dmfit (a); and (b) –(d) simulated from NMR tensors determined from VASP calculations using atomic coordinates from X-ray diffraction (b), from relaxations using the GGA-PBE functional (c), and from relaxations using the vdW-DF2 functional (d).

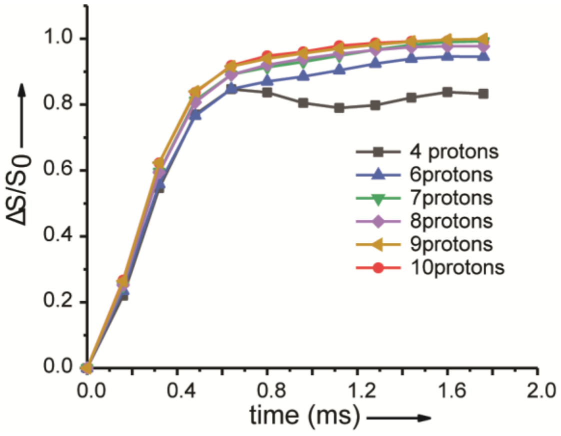

Figure B.2 Calculated $^{13}C\{^{1}H\}$ REDOR curve for different numbers of nearby hydrogens as indicated in the legend for hydromagnesite

Table B.1 Three chemical shift tensor components and RMSE values for Carbon 1 and Carbon 2 from the X-ray crystal structure, and VASP calculations from relaxations using the GGA-PBE functional and vdW-DF2 functional.

Carbon 1	δ_{11} (ppm)* δ_{XX} (ppm)	δ_{22} (ppm)* δ_{YY} (ppm)	δ_{33} (ppm)* δ_{ZZ} (ppm)	RMSE (ppm)
GGA-PBE	192.3	179.0	114.1	6.15
vdWDF2	200	177.8	117.3	3.36
XRD	192.9	160.8	108.6	9.68
Experimentally determined	201.8	174.3	113	----
Carbon 2	δ_{11} (ppm) δ_{XX} (ppm)	δ_{22} (ppm) δ_{YY} (ppm)	δ_{33} (ppm) δ_{ZZ} (ppm)	RMSE (ppm)
GGA-PBE	193.3	186.3	116.1	1.25
vdWDF2	195.8	189.5	118.1	3.04
XRD	190.6	181.1	112.3	4.22
Experimentally determined	192.5	185.4	117.9	----

Table B.2 Distances between the oxygen of carbonate and the closest hydrogens from water and hydroxide surrounding Carbon 1 and Carbon 2 from the X-ray crystal structure, and VASP calculations from relaxations using the GGA-PBE functional and vdW-DF2 functional.

O(water or hydroxide) – H – O (carbonate) *inter*molecular distances						
	X-ray Diffraction		GGA-PBE		vdW-DF2	
	Intermolecular	Bond Distance (Å)	Intermolecular	Bond Distance (Å)	Intermolecular	Bond Distance (Å)
Carbon 1	**H2**: OH_2 —(CO_3^{2-})	2.026	**H2**: OH_2 —(CO_3^{2-})	1.636	**H2**: OH_2 —(CO_3^{2-})	1.817
	H4: OH_2 —(CO_3^{2-})	1.781	**H4**: OH_2 —(CO_3^{2-})	1.658	**H4**: OH_2 —(CO_3^{2-})	1.692
Carbon 2	**He**: OH_2 —(CO_3^{2-})	2.809	**He**: OH_2 —(CO_3^{2-})	2.729	**He**: OH_2 —(CO_3^{2-})	2.544
	Hg:OH^- —(CO_3^{2-})	2.745	**Hg**:OH^- —(CO_3^{2-})	2.698	**Hg**:OH^- —(CO_3^{2-})	2.710

Table B.3 Intramolecular distances between hydrogen and oxygen in water or a hydroxide ion surrounding Carbon 1 and Carbon 2 from the X-ray crystal structure, and VASP calculations from relaxations using the GGA-PBE functional and vdW-DF2 functional.

O(water or hydroxide) – H *intra*molecular distance						
	X-ray Diffraction		GGA-PBE		vdW-DF2	
	Intramolecular	Bond Distance (Å)	Intramolecular	Bond Distance (Å)	Intramolecular	Bond Distance (Å)
Carbon 1	**H2**: H — OH	0.820	**H2**: H — OH	1.020	**H2**: H — OH	1.001
	H4: H — OH	0.895	**H4**: H — OH	1.007	**H4**: H — OH	1.003
Carbon 2	**He**: H — OH	0.802	**He**: H — OH	0.980	**He**: H — OH	0.982
	Hg: H — O^-	0.752	**Hg**: H — O^-	0.972	**Hg**: H — O^-	0.972

References

[1] Mearns, L. O.; Hulme, M.; Carter, T. R.; Leemans, R.; Lal, M.; Whetton, P. Climate Scenario Development (Chapter 13). In Climate Change 2001: The Scientific Basis, Contribution of Working Group I to the Third Assessment Report of the IPCC. **2001**, 583–638. https://doi.org/10.1111/j.1749-8198.2011.00426.x.

[2] IPCC. *IPCC Special Report on CCS*; 2011; Vol. 45. https://doi.org/10.1021/es200619j.

[3] Bachu, Stefan. Sequestration of CO2 in Geological Media in Response to Climate Change: Road Map for Site Selection Using the Transform of the Geological Space into the CO2 Phase Space. *Energy Convers. Manag.* **2002**, *43* (1), 87–102. https://doi.org/10.1016/S0196-8904(01)00009-7.

[4] Bachu, Stefan. Sequestration of CO2 in Geological Media: Criteria and Approach for Site Selection in Response to Climate Change. *Energy Convers. Manag.* **2000**, *41* (9), 953–970. https://doi.org/10.1016/S0196-8904(99)00149-1.

[5] Schrag, Daniel P. Storage of Carbon Dioxide in Offshore Sediments. *Science (80-.).* **2009**, *325* (5948), 1658 LP-1659. https://doi.org/10.1126/science.1175750.

[6] Stéphenne, Karl. Start-up of World's First Commercial Post-Combustion Coal Fired CCS Project: Contribution of Shell Cansolv to SaskPower Boundary Dam ICCS Project. *Energy Procedia* **2014**, *63*, 6106–6110. https://doi.org/10.1016/J.EGYPRO.2014.11.642.

[7] DePaolo, Donald J.; Cole, David R. Geochemistry of Geologic Carbon Sequestration: An Overview. *Rev. Mineral. Geochemistry* **2013**, *77* (1), 1–14. https://doi.org/10.2138/rmg.2013.77.1.

[8] Jun, Young-Shin; Giammar, Daniel E.; Werth, Charles J. Impacts of Geochemical Reactions on Geologic Carbon Sequestration. *Environ. Sci. Technol.* **2013**, *47* (1), 3–8. https://doi.org/10.1021/es3027133.

[9] Carbon Sequestration. *Science (80-.).* **2009**, *325* (5948), 1644 LP-1645. https://doi.org/10.1126/science.325_1644.

[10] Béarat, Hamdallah; McKelvy, Michael J.; Chizmeshya, Andrew V. G.; Gormley, Deirdre; Nunez, Ryan; Carpenter, R. W.; Squires, Kyle; Wolf, George H. Carbon Sequestration via Aqueous Olivine Mineral Carbonation: Role of Passivating Layer Formation. *Environ. Sci. Technol.* **2006**, *40* (15), 4802–4808. https://doi.org/10.1021/es0523340.

[11] Matter, Jürg M.; Kelemen, Peter B. Permanent Storage of Carbon Dioxide in Geological Reservoirs by Mineral Carbonation. *Nat. Geosci.* **2009**, *2*, 837.

[12] McGrail, B. Peter; Schaef, H. Todd; Ho, Anita M.; Chien, Yi-Ju; Dooley, James J.; Davidson, Casie L. Potential for Carbon Dioxide Sequestration in Flood Basalts. *J. Geophys. Res. Solid Earth* **2006**, *111* (B12). https://doi.org/10.1029/2005JB004169.

[13] Harrison, Anna L.; Dipple, Gregory M.; Power, Ian M.; Wilson, Siobhan A.; Kelemen, Peter B.; Hitch, Michael; Southam, Gordon. Carbon Mineralization: From Natural Analogues to Engineered Systems. *Rev. Mineral. Geochemistry* **2013**, *77* (1), 305–360. https://doi.org/10.2138/rmg.2013.77.9.

[14] Surface, J. Andrew; Skemer, Philip; Hayes, Sophia E.; Conradi, Mark S. In Situ Measurement of Magnesium Carbonate Formation from CO_2 Using Static High-Pressure and -Temperature ^{13}C NMR. *Environ. Sci. Technol.* **2013**, *47* (1), 119–125. https://doi.org/10.1021/es301287n.

[15] Surface, J. Andrew; Wang, Fei; Zhu, Yanzhe; Hayes, Sophia E.; Giammar, Daniel E.; Conradi, Mark S. Determining PH at Elevated Pressure and Temperature Using in Situ 13 C NMR. *Environ. Sci. Technol.* **2015**, *49* (3), 1631–1638. https://doi.org/10.1021/es505478y.

[16] Rabi, I. I. Space Quantization in a Gyrating Magnetic Field. *Phys. Rev.* **1937**, *51* (8), 652–654. https://doi.org/10.1103/PhysRev.51.652.

[17] Duer, Melinda J. The Basics of Solid-State NMR. *Solid-State NMR Spectroscopy Principles and Applications*. October 23, 2001. https://doi.org/doi:10.1002/9780470999394.ch1.

[18] Gan, Zhehong; Hung, Ivan; Wang, Xiaoling; Paulino, Joana; Wu, Gang; Litvak, Ilya M.; Gor’kov, Peter L.; Brey, William W.; Lendi, Pietro; Schiano, Jeffrey L.; et al. NMR Spectroscopy up to 35.2 T Using a Series-Connected Hybrid Magnet. *J. Magn. Reson.* **2017**, *284*, 125–136. https://doi.org/10.1016/J.JMR.2017.08.007.

[19] Masion, Armand; Alexandre, Anne; Ziarelli, Fabio; Viel, Stéphane; Santos, Guaciara M. Dynamic Nuclear Polarization NMR as a New Tool to Investigate the Nature of Organic Compounds Occluded in Plant Silica Particles. *Sci. Rep.* **2017**, *7* (1), 3430. https://doi.org/10.1038/s41598-017-03659-z.

[20] Haeberlen, U. *Advance in Magnetic Resonance*; Academic Press: New York, 1976.

[21] ANDREW, E. R.; BRADBURY, A.; EADES, R. G. Removal of Dipolar Broadening of Nuclear Magnetic Resonance Spectra of Solids by Specimen Rotation. *Nature* **1959**, *183* (4678), 1802–1803. https://doi.org/10.1038/1831802a0.

[22] Terry, Gullion. Introduction to Rotational-echo, Double-resonance NMR. *Concepts Magn. Reson.* **1999**, *10* (5), 277–289. https://doi.org/10.1002/(SICI)1099-0534(1998)10:5<277::AID-CMR1>3.0.CO;2-U.

[23] Bennett, Andrew E.; Rienstra, Chad M.; Griffiths, Janet M.; Zhen, Weiguo; Lansbury, Peter T.; Griffin, Robert G. Homonuclear Radio Frequency-Driven Recoupling in Rotating Solids. *J. Chem. Phys.* **1998**, *108* (22), 9463–9479. https://doi.org/10.1063/1.476420.

[24] Duer, Melinda J.; Farnan, Ian. Quadrupole Coupling: Its Measurement and Uses. *Solid-State NMR Spectroscopy Principles and Applications*. October 23, 2001.

https://doi.org/doi:10.1002/9780470999394.ch4.

[25] Samoson, A.; Pines, A. Double Rotor for Solid-state NMR. *Rev. Sci. Instrum.* **1989**, *60* (10), 3239–3241. https://doi.org/10.1063/1.1140558.

[26] ANDREW, E. R.; BRADBURY, A.; EADES, R. G. Nuclear Magnetic Resonance Spectra from a Crystal Rotated at High Speed. *Nature* **1958**, *182* (4650), 1659. https://doi.org/10.1038/1821659a0.

[27] Hao Yang. Solid-State NMR Study of the Tertiary Structure of the Peptidoglycan of Enterococcus Faecalis and the Structures of Phorbol Diacetate and Bryostatin Bound to Protein Kinase Cδ C1b Domain. **2015**.

[28] Hahn, E. L. Spin Echoes. *Phys. Rev.* **1950**, *80* (4), 580–594. https://doi.org/10.1103/PhysRev.80.580.

[29] Gullion, Terry; Schaefer, Jacob. Rotational-Echo Double-Resonance NMR. *J. Magn. Reson.* **1989**, *81* (1), 196–200. https://doi.org/10.1016/0022-2364(89)90280-1.

[30] Spiegelmann, Roberto. Introduction. *J. Neurooncol.* **2010**, *98* (2), 153. https://doi.org/10.1007/s11060-010-0219-4.

[31] Xu, Yijue; Southern, Scott A.; Szell, Patrick M. J.; Bryce, David L. The Role of Solid-State Nuclear Magnetic Resonance in Crystal Engineering. *CrystEngComm* **2016**, *18* (28), 5236–5252. https://doi.org/10.1039/C6CE01206J.

[32] Harris, Kenneth D. M.; Hughes, Colan E.; Williams, P. Andrew; Edwards-Gau, Gregory R. `NMR Crystallization': {\it in-Situ} NMR Techniques for Time-Resolved Monitoring of Crystallization Processes. *Acta Crystallogr. Sect. C* **2017**, *73* (3), 137–148. https://doi.org/10.1107/S2053229616019811.

[33] Martineau, Charlotte. NMR Crystallography: Applications to Inorganic Materials. *Solid State Nucl. Magn. Reson.* **2014**, *63–64*, 1–12. https://doi.org/https://doi.org/10.1016/j.ssnmr.2014.07.001.

[34] Brouwer, Darren H.; Enright, Gary D. Probing Local Structure in Zeolite Frameworks: Ultrahigh-Field NMR Measurements and Accurate First-Principles Calculations of Zeolite 29Si Magnetic Shielding Tensors. *J. Am. Chem. Soc.* **2008**, *130* (10), 3095–3105. https://doi.org/10.1021/ja077430a.

[35] Fyfe, Colin A.; Brouwer, Darren H.; Lewis, Andrew R.; Villaescusa, Luis A.; Morris, Russell E. Combined Solid State NMR and X-Ray Diffraction Investigation of the Local Structure of the Five-Coordinate Silicon in Fluoride-Containing as-Synthesized STF Zeolite. *J. Am. Chem. Soc.* **2002**, *124* (26), 7770–7778. https://doi.org/10.1021/ja012558s.

[36] Harper, James K.; Grant, David M.; Zhang, Yuegang; Lee, Peter L.; Von Dreele, Robert. Characterizing Challenging Microcrystalline Solids with Solid-State NMR Shift Tensor and Synchrotron x-Ray Powder Diffraction Data: Structural Analysis of Ambuic Acid. *J. Am. Chem. Soc.* **2006**, *128*, 1547–1552. https://doi.org/10.1021/ja055570j.

[37] Salager, Elodie; Day, Graeme M.; Stein, Robin S.; Pickard, Chris J.; Elena, Bénédicte; Emsley, Lyndon. Powder Crystallography by Combined Crystal Structure Prediction and High-Resolution 1H Solid-State NMR Spectroscopy. *J. Am. Chem. Soc.* **2010**, *132* (8), 2564–2566. https://doi.org/10.1021/ja909449k.

[38] Beran, Gregory J. O.; Hartman, Joshua D.; Heit, Yonaton N. Predicting Molecular Crystal Properties from First Principles: Finite-Temperature Thermochemistry to NMR Crystallography. *Acc. Chem. Res.* **2016**, *49* (11), 2501–2508. https://doi.org/10.1021/acs.accounts.6b00404.

[39] Harper, James K.; Iuliucci, Robbie; Gruber, Matthew; Kalakewich, Keyton. Refining Crystal Structures with Experimental13C NMR Shift Tensors and Lattice-Including Electronic Structure Methods. *CrystEngComm* **2013**, *15*, 8693–8704. https://doi.org/10.1039/c3ce40108a.

[40] Gajda, J.; Olejniczak, S.; Bryndal, I.; Potrzebowski, M. J. Elucidation of Structural Restraints for Phosphate Residues with Different Hydrogen Bonding and Ionization States. *J. Phys. Chem. B* **2008**, *112*, 14036–14044. https://doi.org/10.1021/jp807516b.

[41] Harper, J. K.; Mulgrew, A. E.; Li, J. Y.; Barich, D. H.; Strobel, G. A.; Grant, D. M. Characterization of Stereochemistry and Molecular Conformation Using Solid-State NMR Tensors. *J. Am. Chem. Soc.* **2001**, *123*, 9837–9842. https://doi.org/10.1021/ja010997l.

[42] Panina, N.; Leusen, F. J. J.; Janssen, F. F. B. J.; Verwer, P.; Meekes, H.; Vlieg, E.; Deroover, G. Crystal Structure Prediction of Organic Pigments: Quinacridone as an Example. *J. Appl. Crystallogr.* **2007**, *40* (1), 105–114. https://doi.org/10.1107/S0021889806043767.

[43] Payne, R. S.; Roberts, R. J.; Rowe, R. C.; Docherty, R. Examples of Successful Crystal Structure Prediction: Polymorphs of Primidone and Progesterone. *Int. J. Pharm.* **1999**, *177* (2), 231–245. https://doi.org/10.1016/S0378-5173(98)00348-2.

[44] Lekgoathi, M. D. S.; Kock, L. D. Effect of Short and Long Range Order on Crystal Structure Interpretation: Raman and Powder X-Ray Diffraction of LiPF6. *Spectrochim. Acta Part A Mol. Biomol. Spectrosc.* **2016**, *153*, 651–654. https://doi.org/https://doi.org/10.1016/j.saa.2015.09.025.

[45] Nielsen, Ulla Gro; Majzlan, Juraj; Grey, Clare P. Determination and Quantification of the Local Environments in Stoichiometric and Defect Jarosite by Solid-State 2H NMR Spectroscopy. *Chem. Mater.* **2008**, *20* (6), 2234–2241. https://doi.org/10.1021/cm702523d.

[46] Martineau, Charlotte; Bouchevreau, Boris; Tian, Zhijian; Lohmeier, Sven Jare; Behrens, Peter; Taulelle, Francis. Beyond the Limits of X-Ray Powder Diffraction: Description of the Nonperiodic Subnetworks in Aluminophosphate-Cloverite by NMR Crystallography. *Chem. Mater.* **2011**, *23* (21), 4799–4809. https://doi.org/10.1021/cm2021033.

[47] Webber, Amy L.; Emsley, Lyndon; Claramunt, Rosa M.; Brown, Steven P. NMR Crystallography of Campho [2 , 3-c] Pyrazole (Z ′) 6): Combining High-Resolution H-

13 C Solid-State MAS NMR Spectroscopy and GIPAW Chemical-Shift Calculations. *J. Phys. Chem. A* **2010**, *114* (38), 10435–10442.

[48] Wang, Luther; Uribe-Romo, Fernando J.; Mueller, Leonard J.; Harper, James K. Predicting Anisotropic Thermal Displacements for Hydrogens from Solid-State NMR: A Study on Hydrogen Bonding in Polymorphs of Palmitic Acid. *Phys. Chem. Chem. Phys.* **2018**, *20* (13), 8475–8487. https://doi.org/10.1039/C7CP06724K.

[49] Hofstetter, Albert; Emsley, Lyndon. Positional Variance in NMR Crystallography. *J. Am. Chem. Soc.* **2017**, *139* (7), 2573–2576. https://doi.org/10.1021/jacs.6b12705.

[50] Ashbrook, Sharon E.; Sneddon, Scott. New Methods and Applications in Solid-State NMR Spectroscopy of Quadrupolar Nuclei. *J. Am. Chem. Soc.* **2014**, *136*, 15440–15456. https://doi.org/10.1021/ja504734p.

[51] Phillips, Brian L. Crystallography and NMR: Applications to Geochemistry. *eMagRes*. March 15, 2009. https://doi.org/doi:10.1002/9780470034590.emrstm1045.

[52] Andrew, E. R. The Narrowing of NMR Spectra of Solids by High-Speed Specimen Rotation and the Resolution of Chemical Shift and Spin Multiplet Structures for Solids. *Prog. Nucl. Magn. Reson. Spectrosc.* **1971**, *8* (1), 1–39. https://doi.org/10.1016/0079-6565(71)80001-8.

[53] Kohn, W.; Sham, L. J. Self-Consistent Equations Including Exchange and Correlation Effects. *Phys. Rev.* **1965**, *140* (4A). https://doi.org/10.1103/PhysRev.140.A1133.

[54] Rajagopal, A. K.; Callaway, J. Inhomogeneous Electron Gas. *Phys. Rev. B* **1973**, *7* (5), 1912–1919. https://doi.org/10.1103/PhysRevB.7.1912.

[55] Paluch, Piotr; Pawlak, Tomasz; Oszajca, Marcin; Lasocha, Wieslaw; Potrzebowski, Marek J. Fine Refinement of Solid State Structure of Racemic Form of Phospho-Tyrosine Employing NMR Crystallography Approach. *Solid State Nucl. Magn. Reson.* **2015**, *65*, 2–11. https://doi.org/https://doi.org/10.1016/j.ssnmr.2014.08.002.

[56] Lüdeker, David; Brunklaus, Gunther. NMR Crystallography of Ezetimibe Co-Crystals. *Solid State Nucl. Magn. Reson.* **2015**, *65*, 29–40. https://doi.org/https://doi.org/10.1016/j.ssnmr.2014.11.002.

[57] Facelli, Julio C.; Grant, David M. Determination of Molecular Symmetry in Crystalline Naphthalene Using Solid-State NMR. *Nature* **1993**, *365*, 325.

[58] Chebbi, H.; Chebbi, M.; Guesmi, A.; Arfaoui, Y. Crystal Structure Determination, and DFT Calculations of Dichlorobis-(Dimethylsulfoxide-O)Copper(II). *J. Struct. Chem.* **2016**, *57* (6), 1104–1110. https://doi.org/10.1134/S002247661606007X.

[59] Perdew, John P.; Burke, Kieron; Ernzerhof, Matthias. Generalized Gradient Approximation Made Simple. *Phys. Rev. Lett.* **1996**, *77* (18), 3865–3868. https://doi.org/10.1103/PhysRevLett.77.3865.

[60] Brik, M. G. First-Principles Calculations of Structural, Electronic, Optical and Elastic

Properties of Magnesite MgCO3 and Calcite CaCO3. *Phys. B Condens. Matter* **2011**, *406* (4), 1004–1012. https://doi.org/10.1016/j.physb.2010.12.049.

[61] Hossain, Faruque M.; Dlugogorski, B. Z.; Kennedy, E. M.; Belova, I. V.; Murch, Graeme E. Electronic, Optical and Bonding Properties of MgCO3. *Solid State Commun.* **2010**, *150* (17–18), 848–851. https://doi.org/10.1016/j.ssc.2010.02.008.

[62] Björkman, Torbjörn. A van Der Waals Density Functional for Solids. **2012**, *085108* (2005), 1–12. https://doi.org/10.1103/PhysRevB.86.165109.

[63] Zhang, Guo Xu; Tkatchenko, Alexandre; Paier, Joachim; Appel, Heiko; Scheffler, Matthias. Van Der Waals Interactions in Ionic and Semiconductor Solids. *Phys. Rev. Lett.* **2011**, *107* (24), 1–5. https://doi.org/10.1103/PhysRevLett.107.245501.

[64] Grimme, Stefan. Density Functional Theory with London Dispersion Corrections. *Wiley Interdiscip. Rev. Comput. Mol. Sci.* **2011**, *1* (2), 211–228. https://doi.org/10.1002/wcms.30.

[65] Oelkers, Eric H.; Gislason, Sigurdur R.; Matter, Juerg. Mineral Carbonation of CO2. *Elements* **2008**, *4* (5), 333–337. https://doi.org/10.2113/gselements.4.5.333.

[66] Lackner, Klaus S.; Wendt, Christopher H.; Butt, Darryl P.; Joyce, Edward L.; Sharp, David H. Carbon Dioxide Disposal in Carbonate Minerals. *Energy* **1995**, *20* (11), 1153–1170. https://doi.org/10.1016/0360-5442(95)00071-N.

[67] Giammar, Daniel E.; Bruant, Robert G.; Peters, Catherine A. Forsterite Dissolution and Magnesite Precipitation at Conditions Relevant for Deep Saline Aquifer Storage and Sequestration of Carbon Dioxide. *Chem. Geol.* **2005**, *217* (3–4), 257–276. https://doi.org/10.1016/J.CHEMGEO.2004.12.013.

[68] Hänchen, M.; Prigiobbe, V.; Storti, G.; Seward, T. M.; Mazzotti, M. Dissolution Kinetics of Fosteritic Olivine at 90–150 °C Including Effects of the Presence of CO2. *Geochim. Cosmochim. Acta* **2006**, *70* (17), 4403–4416. https://doi.org/10.1016/J.GCA.2006.06.1560.

[69] Surface, JA. In Situ High Pressure and Temperature 13C NMR for the Study of Carbonation Reactions of CO2. **2013**.

[70] Alderman, Donald W.; Grant, David M. An Efficient Decoupler Coil Design Which Reduces Heating in Conductive Samples in Superconducting Spectrometers. *J. Magn. Reson.* **1979**, *36* (3), 447–451. https://doi.org/10.1016/0022-2364(79)90123-9.

[71] Sesti, Erika L.; Cui, Jinlei; Hayes, Sophia E.; Conradi, Mark S. A Flow-through, Elevated-Temperature and -Pressure NMR Apparatus for in-Situ CO_2 Sequestration Studies. *J. Magn. Reson.* **2017**, *282*, 136–141. https://doi.org/10.1016/j.jmr.2017.08.005.

[72] Gribb, Tye T.; Cooper, Reid F. Low-Frequency Shear Attenuation in Polycrystalline Olivine: Grain Boundary Diffusion and the Physical Significance of the Andrade Model for Viscoelastic Rheology. *J. Geophys. Res. Solid Earth* **1998**, *103* (B11), 27267–27279.

https://doi.org/10.1029/98JB02786.

[73] Wolff-Boenisch, D.; Galeczka, I. M.; Mesfin, K. G.; Gislason, S. R. A Foray into False Positive Results in Mineral Dissolution and Precipitation Studies. *Appl. Geochemistry* **2016**, *71*, 9–19. https://doi.org/10.1016/J.APGEOCHEM.2016.05.011.

[74] Wells, Rachel K.; Xiong, Wei; Sesti, Erika; Cui, Jinlei; Giammar, Daniel; Skemer, Philip; Hayes, Sophia E.; Conradi, Mark S. Spatially-Variable Carbonation Reactions in Polycrystalline Olivine. *Geochim. Cosmochim. Acta* **2017**, *204*, 252–266. https://doi.org/10.1016/j.gca.2017.02.003.

[75] Davies, Peter J.; Bubela, B. The Transformation of Nesquehonite into Hydromagnesite. *Chem. Geol.* **1973**, *12* (4), 289–300. https://doi.org/https://doi.org/10.1016/0009-2541(73)90006-5.

[76] Hänchen, Markus; Prigiobbe, Valentina; Baciocchi, Renato; Mazzotti, Marco. Precipitation in the Mg-Carbonate System—effects of Temperature and CO2 Pressure. *Chem. Eng. Sci.* **2008**, *63* (4), 1012–1028. https://doi.org/10.1016/J.CES.2007.09.052.

[77] Qafoku, Odeta; Hu, Jianzhi; Hess, Nancy J.; Hu, Mary Y.; Ilton, Eugene S.; Feng, Ju; Arey, Bruce W.; Felmy, Andrew R. Formation of Submicron Magnesite during Reaction of Natural Forsterite in H2O-Saturated Supercritical CO2. *Geochim. Cosmochim. Acta* **2014**, *134*, 197–209. https://doi.org/10.1016/J.GCA.2013.09.024.

[78] Xiong, Wei; Giammar, Daniel. Forsterite Carbonation in Zones with Transport Limited by Diffusion. *Environ. Sci. Technol. Lett.* **2014**, *1* (8), 333–338. https://doi.org/10.1021/ez500182s.

[79] Daval, Damien; Sissmann, Olivier; Menguy, Nicolas; Saldi, Giuseppe D.; Guyot, François; Martinez, Isabelle; Corvisier, Jérôme; Garcia, Bruno; Machouk, Imène; Knauss, Kevin G.; et al. Influence of Amorphous Silica Layer Formation on the Dissolution Rate of Olivine at 90 °C and Elevated PCO2. *Chem. Geol.* **2011**, *284* (1–2), 193–209. https://doi.org/10.1016/J.CHEMGEO.2011.02.021.

[80] Castañeda-Herrera, C. A.; Black, J. R.; Llanos, E. M.; Stevens, G. W.; Haese, R. R. Formation of an Amorphous Silica Gel Barrier under CO2 Storage Conditions. *Int. J. Greenh. Gas Control* **2018**, *78*, 27–36. https://doi.org/https://doi.org/10.1016/j.ijggc.2018.07.013.

[81] Pokrovsky, Oleg S.; Schott, Jacques. Kinetics and Mechanism of Forsterite Dissolution at 25°C and PH from 1 to 12. *Geochim. Cosmochim. Acta* **2000**, *64* (19), 3313–3325. https://doi.org/10.1016/S0016-7037(00)00434-8.

[82] Wang, Fei; Giammar, Daniel E. Forsterite Dissolution in Saline Water at Elevated Temperature and High CO_2 Pressure. *Environ. Sci. Technol.* **2013**, *47* (1), 168–173. https://doi.org/10.1021/es301231n.

[83] Kwak, Ja Hun; Hu, Jian Zhi; Hoyt, David W.; Sears, Jesse A.; Wang, Chongming; Rosso, Kevin M.; Felmy, Andrew R. Metal Carbonation of Forsterite in Supercritical CO2 and

H2O Using Solid State 29Si, 13C NMR Spectroscopy. *J. Phys. Chem. C* **2010**, *114* (9), 4126–4134. https://doi.org/10.1021/jp1001308.

[84] Stebbins, Jonathan F.; Smyth, Joseph R.; Panero, Wendy R.; Frost, Daniel J. Forsterite, Hydrous and Anhydrous Wadsleyite and Ringwoodite (Mg2SiO4): 29Si NMR Results for Chemical Shift Anisotropy, Spin-Lattice Relaxation, and Mechanism of Hydration. *Am. Mineral.* **2009**, *94* (7), 905–915. https://doi.org/10.2138/am.2009.3184.

[85] Ashbrook, Sharon E.; Le Pollès, Laurent; Pickard, Chris J.; Berry, Andrew J.; Wimperis, Stephen; Farnan, Ian. First-Principles Calculations of Solid-State 17O and 29Si NMR Spectra of Mg2SiO4 Polymorphs. *Phys. Chem. Chem. Phys.* **2007**, *9* (13), 1587–1598. https://doi.org/10.1039/B618211A.

[86] Magi, M.; Lippmaa, E.; Samoson, A.; Engelhardt, G.; Grimmer, A. R. Solid-State High-Resolution Silicon-29 Chemical Shifts in Silicates. *J. Phys. Chem.* **1984**, *88* (8), 1518–1522. https://doi.org/10.1021/j150652a015.

[87] Simakin, A. G.; Salova, T. P.; Zavelsky, V. O. Mechanism of Water Dissolution in Sodium-Silicate Melts and Glasses: Structural Interpretation of Spectroscopic Data. *Geochemistry Int.* **2008**, *46* (2), 107–115. https://doi.org/10.1134/S0016702908020018.

[88] Giammar, Daniel E.; Wang, Fei; Guo, Bin; Surface, J. Andrew; Peters, Catherine A.; Conradi, Mark S.; Hayes, Sophia E. Impacts of Diffusive Transport on Carbonate Mineral Formation from Magnesium Silicate-CO2-Water Reactions. *Environ. Sci. Technol.* **2014**, *48* (24), 14344–14351. https://doi.org/10.1021/es504047t.

[89] Icenhower, Jonathan P.; Dove, Patricia M. The Dissolution Kinetics of Amorphous Silica into Sodium Chloride Solutions: Effects of Temperature and Ionic Strength. *Geochim. Cosmochim. Acta* **2000**, *64* (24), 4193–4203. https://doi.org/10.1016/S0016-7037(00)00487-7.

[90] Dove, Patricia M.; Elston, Stephen F. Dissolution Kinetics of Quartz in Sodium Chloride Solutions: Analysis of Existing Data and a Rate Model for 25°C. *Geochim. Cosmochim. Acta* **1992**, *56* (12), 4147–4156. https://doi.org/10.1016/0016-7037(92)90257-J.

[91] Moore, Jeremy K.; Surface, J. Andrew; Brenner, Allison; Skemer, Philip; Conradi, Mark S.; Hayes, Sophia E. Quantitative Identification of Metastable Magnesium Carbonate Minerals by Solid-State 13 C NMR Spectroscopy. *Environ. Sci. Technol.* **2015**, *49* (1), 657–664. https://doi.org/10.1021/es503390d.

[92] Gilli, Gastone; Gilli, Paola. *The Nature of the Hydrogen Bond: Outline of a Comprehensive Hydrogen Bond Theory*; Oxford University Press: Oxford, 2009. https://doi.org/10.1093/acprof:oso/9780199558964.001.0001.

[93] Brédas, J. L.; Poskin, M. P.; Delhalle, J.; André, J. M.; Chojnacki, H. Electronic Structure of Hydrogen-Bonded Imidazole Chains. Influence of the Proton Position. *J. Phys. Chem.* **1984**, *88* (24), 5882–5887. https://doi.org/10.1021/j150668a028.

[94] Mottamal, Madhusoodanan; Lazaridis, Themis. The Contribution of Cα-H...O Hydrogen

Bonds to Membrane Protein Stability Depends on the Position of the Amide. *Biochemistry* **2005**, *44* (5), 1607–1613. https://doi.org/10.1021/bi048065s.

[95] Aakeroy, Christer B.; Seddon, Kenneth R. The Hydrogen Bond and Crystal Engineering. *Chem. Soc. Rev.* **1993**, *22* (6), 397–407. https://doi.org/10.1039/cs9932200397.

[96] Truhlar, Donald G. Test of Bond-Order Methods for Predicting the Position of the Minimum-Energy Path for Hydrogen Atom Transfer Reactions. *J. Am. Chem. Soc.* **1972**, *94* (21), 7584–7586. https://doi.org/10.1021/ja00776a055.

[97] Petković, Milena. O-H Stretch in Phenol and Its Hydrogen-Bonded Complexes: Band Position and Relaxation Pathways. *J. Phys. Chem. A* **2012**, *116* (1), 364–371. https://doi.org/10.1021/jp209897y.

[98] Lackner, Klaus S.; Wendt, Christopher H.; Butt, Darryl P.; Joyce, Edward L.; Sharp, David H. Carbon Dioxide Disposal in Carbonate Minerals. *Energy* **1995**, *20* (11), 1153–1170. https://doi.org/10.1016/0360-5442(95)00071-N.

[99] Pan, Shu-Yuan; Chung, Tai-Chun; Ho, Chang-Ching; Hou, Chin-Jen; Chen, Yi-Hung; Chiang, Pen-Chi. CO 2 Mineralization and Utilization Using Steel Slag for Establishing a Waste-to-Resource Supply Chain. *Sci. Rep.* **2017**, *7* (October), 1–11. https://doi.org/10.1038/s41598-017-17648-9.

[100] Hänchen, Markus; Prigiobbe, Valentina; Baciocchi, Renato; Mazzotti, Marco. Precipitation in the Mg-Carbonate System-Effects of Temperature and CO2 Pressure. *Chem. Eng. Sci.* **2008**, *63* (4), 1012–1028. https://doi.org/10.1016/j.ces.2007.09.052.

[101] King, Helen E.; Plümper, Oliver; Putnis, Andrew. Effect of Secondary Phase Formation on the Carbonation of Olivine. *Environ. Sci. Technol.* **2010**, *44* (16), 6503–6509. https://doi.org/10.1021/es9038193.

[102] Chaka, Anne M.; Felmy, Andrew R. Ab Initio Thermodynamic Model for Magnesium Carbonates and Hydrates. *J. Phys. Chem. A* **2014**, *118* (35), 7469–7488. https://doi.org/10.1021/jp500271n.

[103] Xu, Jie; Yan, Chao; Zhang, Fangfu; Konishi, Hiromi; Xu, Huifang; Teng, H. Henry. Testing the Cation-Hydration Effect on the Crystallization of Ca–Mg–CO3 Systems. *Proc. Natl. Acad. Sci.* **2013**, *110* (44), 17750–17755.

[104] Saharay, Moumita; Yazaydin, A. Ozgur; Kirkpatrick, R. James. Dehydration-Induced Amorphous Phases of Calcium Carbonate. *J. Phys. Chem. B* **2013**, *117* (12), 3328–3336. https://doi.org/10.1021/jp308353t.

[105] Tommaso, Devis Di; de Leeuw, Nora H. Structure and Dynamics of the Hydrated Magnesium Ion and of the Solvated Magnesium Carbonates: Insights from First Principles Simulations. *Phys. Chem. Chem. Phys.* **2010**, *12* (4), 894–901. https://doi.org/10.1039/B915329B.

[106] Gullion, Terry; Schaefer, Jacob. Rotational-Echo Double-Resonance NMR. *J. Magn.*

Reson. **1989**, *81* (1), 196–200. https://doi.org/https://doi.org/10.1016/0022-2364(89)90280-1.

[107] Wickramasinghe, Nalinda P.; Shaibat, Medhat A.; Jones, Christopher R.; Casabianca, Leah B.; De Dios, Angel C.; Harwood, John S.; Ishii, Yoshitaka. Progress in C13 and H1 Solid-State Nuclear Magnetic Resonance for Paramagnetic Systems under Very Fast Magic Angle Spinning. *J. Chem. Phys.* **2008**, *128* (5). https://doi.org/10.1063/1.2833574.

[108] Wang, Mingfei; Bertmer, Marko; Demco, Dan E.; Blümich, Bernhard. Segmental and Local Chain Mobilities in Elastomers by 13C- 1H Residual Heteronuclear Dipolar Couplings. *J. Phys. Chem. B* **2004**, *108* (30), 10911–10918. https://doi.org/10.1021/jp048392+.

[109] Ishii, Yoshitaka; Wickramasinghe, Nalinda P.; Chimon, Sandra. A New Approach in 1D and 2D 13C High-Resolution Solid-State NMR Spectroscopy of Paramagnetic Organometallic Complexes by Very Fast Magic-Angle Spinning. *J. Am. Chem. Soc.* **2003**, *125* (12), 3438–3439. https://doi.org/10.1021/ja0291742.

[110] Mehta, Anil K.; Hirsh, Donald J.; Oyler, Nathan; Drobny, Gary P.; Schaefer, Jacob. Carbon-Proton Dipolar Decoupling in REDOR. *J. Magn. Reson.* **2000**, *145* (1), 156–158. https://doi.org/https://doi.org/10.1006/jmre.2000.2098.

[111] Carr, H. Y.; Purcell, E. M. Effects of Diffusion on Free Precession in Nuclear Magnetic Resonance Experiments. *Phys. Rev.* **1954**, *94* (3), 630–638. https://doi.org/10.1103/PhysRev.94.630.

[112] Massiot, Dominique; Fayon, Franck; Capron, Mickael; King, Ian; Le Calvé, Stéphanie; Alonso, Bruno; Durand, Jean Olivier; Bujoli, Bruno; Gan, Zhehong; Hoatson, Gina. Modelling One- and Two-Dimensional Solid-State NMR Spectra. *Magn. Reson. Chem.* **2002**, *40* (1), 70–76. https://doi.org/10.1002/mrc.984.

[113] Gullion, Terry; Schaefer, Jacob. Elimination of Resonance Offset Effects in Rotational-Echo, Double-Resonance NMR. *J. Magn. Reson.* **1991**, *92* (2), 439–442. https://doi.org/10.1016/0022-2364(91)90286-3.

[114] Bak, Mads; Rasmussen, Jimmy T.; Nielsen, Niels Chr. SIMPSON: A General Simulation Program for Solid-State NMR Spectroscopy. *J. Magn. Reson.* **2000**, *147* (2), 296–330. https://doi.org/10.1006/jmre.2000.2179.

[115] Kresse, G.; Furthmüller, J. Efficient Iterative Schemes for Ab Initio Total-Energy Calculations Using a Plane-Wave Basis Set. *Phys. Rev. B - Condens. Matter Mater. Phys.* **1996**, *54* (16), 11169–11186. https://doi.org/10.1103/PhysRevB.54.11169.

[116] Joubert, D. From Ultrasoft Pseudopotentials to the Projector Augmented-Wave Method. *Phys. Rev. B - Condens. Matter Mater. Phys.* **1999**, *59* (3), 1758–1775. https://doi.org/10.1103/PhysRevB.59.1758.

[117] Blöchl, P. E. Projector Augmented-Wave Method. *Phys. Rev. B* **1994**, *50* (24), 17953–17979. https://doi.org/10.1103/PhysRevB.50.17953.

[118] Dion, M.; Rydberg, H.; Schröder, E.; Langreth, D. C.; Lundqvist, B. I. Van Der Waals Density Functional for General Geometries. *Phys. Rev. Lett.* **2004**, *92* (24), 246401.

[119] Román-Pérez, Guillermo; Soler, José M. Efficient Implementation of a van Der Waals Density Functional: Application to Double-Wall Carbon Nanotubes. *Phys. Rev. Lett.* **2009**, *103* (9), 96102. https://doi.org/10.1103/PhysRevLett.103.096102.

[120] Klimeš, Jiří; Bowler, David R.; Michaelides, Angelos. Van Der Waals Density Functionals Applied to Solids. *Phys. Rev. B* **2011**, *83* (19), 195131.

[121] Lee, Kyuho; Murray, Éamonn D.; Kong, Lingzhu; Lundqvist, Bengt I.; Langreth, David C. Higher-Accuracy van Der Waals Density Functional. *Phys. Rev. B* **2010**, *82* (8), 81101. https://doi.org/10.1103/PhysRevB.82.081101.

[122] Blöchl, Peter E.; Jepsen, O.; Andersen, O. K. Improved Tetrahedron Method for Brillouin-Zone Integrations. *Phys. Rev. B* **1994**, *49* (23), 16223–16233. https://doi.org/10.1103/PhysRevB.49.16223.

[123] Ong, Shyue Ping; Richards, William Davidson; Jain, Anubhav; Hautier, Geoffroy; Kocher, Michael; Cholia, Shreyas; Gunter, Dan; Chevrier, Vincent L.; Persson, Kristin A.; Ceder, Gerbrand. Python Materials Genomics (Pymatgen): A Robust, Open-Source Python Library for Materials Analysis. *Comput. Mater. Sci.* **2013**, *68*, 314–319. https://doi.org/https://doi.org/10.1016/j.commatsci.2012.10.028.

[124] Yates, Jonathan R.; Pickard, Chris J.; Mauri, Francesco. Calculation of NMR Chemical Shifts for Extended Systems Using Ultrasoft Pseudopotentials. *Phys. Rev. B - Condens. Matter Mater. Phys.* **2007**, *76* (2), 1–11. https://doi.org/10.1103/PhysRevB.76.024401.

[125] Pickard, Chris J.; Mauri, Francesco. All-Electron Magnetic Response with Pseudopotentials: NMR Chemical Shifts. *Phys. Rev. B* **2001**, *63* (24), 245101. https://doi.org/10.1103/PhysRevB.63.245101.

[126] Akao, M.; Marumo, F.; Iwai, S. The Crystal Structure of Hydromagnesite. *Acta Crystallogr. Sect. B* **1974**, *30* (11), 2670–2672. https://doi.org/10.1107/S0567740874007771.

[127] Akao, M.; Iwai, S. The Hydrogen Bonding of Hydromagnesite. *Acta Crystallogr. Sect. B* **1977**, *33* (4), 1273–1275. https://doi.org/10.1107/S0567740877005834.

[128] Giester, G.; Lengauer, C. L.; Rieck, B. The Crystal Structure of Nesquehonite, MgCO 3 · 3H 2 O, from Lavrion, Greece. *Mineral. Petrol.* **2000**, *70* (3–4), 153–163. https://doi.org/10.1007/s007100070001.

[129] Gaffey, S. J. H2O and OH in Echinoid Calcite: A Spectroscopic Study. *Am. Mineral.* **1995**, *80* (9–10), 947–959.

[130] Harris, Robin K.; Becker, Edwin D.; De Cabral Menezes, Sonia M.; Granger, Pierre; Hoffman, Roy E.; Zilm, Kurt W. Further Conventions for NMR Shielding and Chemical Shifts (IUPAC Recommendations 2008). *Magn. Reson. Chem.* **2008**, *46* (6), 582–598.

https://doi.org/10.1002/mrc.2225.

[131] Sen, Sabyasachi; Kaseman, Derrick C.; Colas, Bruno; Jacob, Dorrit E.; Clark, Simon M. Hydrogen Bonding Induced Distortion of CO3 Units and Kinetic Stabilization of Amorphous Calcium Carbonate: Results from 2D 13C NMR Spectroscopy. *Phys. Chem. Chem. Phys.* **2016**, *18* (30), 20330–20337. https://doi.org/10.1039/C6CP02729F.

[132] Schmidt-Rohr, Klaus; Hong, Mei. Measurements of Carbon to Amide-Proton Distances by C-H Dipolar Recoupling with 15N NMR Detection. *J. Am. Chem. Soc.* **2003**, *125* (19), 5648–5649. https://doi.org/10.1021/ja0344415.

[133] Van Rossum, B. J.; De Groot, C. P.; Ladizhansky, V.; Vega, S.; De Groot, H. J. M. A Method for Measuring Heteronuclear (1H-13C) Distances in High Speed MAS NMR. *J. Am. Chem. Soc.* **2000**, *122* (14), 3465–3472. https://doi.org/10.1021/ja992714j.

[134] Agarwal, Vipin; Unser, Rasmus; Fink, Uwe; Faelber, Katja; Reif, Bernd. Identification of Hydroxyl Protons, Determination of Their Exchange Dynamics, and Characterization of Hydrogen Bonding in a Microcrystallin Protein. *J. Am. Chem. Soc.* **2010**, *132* (9), 3187–3195. https://doi.org/10.1021/ja910167q.

[135] He, Lianhua; Liu, Fang; Hautier, Geoffroy; Oliveira, Micael J. T.; Marques, Miguel A. L.; Vila, Fernando D.; Rehr, J. J.; Rignanese, G. M.; Zhou, Aihui. Accuracy of Generalized Gradient Approximation Functionals for Density-Functional Perturbation Theory Calculations. *Phys. Rev. B* **2014**, *89* (6), 64305. https://doi.org/10.1103/PhysRevB.89.064305.

[136] van de Walle, A.; Ceder, G. Correcting Overbinding in Local-Density-Approximation Calculations. *Phys. Rev. B* **1999**, *59* (23), 14992–15001. https://doi.org/10.1103/PhysRevB.59.14992.

[137] Kloprogge, J. T.; Martens, W. N.; Nothdurft, L.; Duong, L. V; Webb, G. E. Low Temperature Synthesis and Characterization of Nesquehonite. *J. Mater. Sci. Lett.* **2003**, *22* (11), 825–829. https://doi.org/10.1023/A:1023916326626.

[138] Ferrini, Vincenzo; De Vito, Caterina; Mignardi, Silvano. Synthesis of Nesquehonite by Reaction of Gaseous CO2 with Mg Chloride Solution: Its Potential Role in the Sequestration of Carbon Dioxide. *J. Hazard. Mater.* **2009**, *168* (2–3), 832–837. https://doi.org/10.1016/J.JHAZMAT.2009.02.103.

[139] Harrison, Anna L.; Power, Ian M.; Dipple, Gregory M. Accelerated Carbonation of Brucite in Mine Tailings for Carbon Sequestration. *Environ. Sci. Technol.* **2013**, *47* (1), 126–134. https://doi.org/10.1021/es3012854.

[140] Langmuir, Donald. Stability of Carbonates in the System $MgO-CO2-H2O. *J. Geol.* **1965**, *73* (5), 730–754. https://doi.org/10.1086/627113.

[141] Lanas, J.; Alvarez, J. I. Dolomitic Lime: Thermal Decomposition of Nesquehonite. *Thermochim. Acta* **2004**, *421* (1–2), 123–132. https://doi.org/10.1016/J.TCA.2004.04.007.

[142] Genth, Frederick Augustus; S. L., Penfield. On Lansfordite, Nesquehonite, a New Mineral, and Pseudomorphs of Nesquehonite after Lansfordite. *Am. J. Sci.* **1890**, *39*, 121–137. https://doi.org/10.2475/ajs.s3-39.230.121.

[143] White, William. B. Infrared Characterization of Water and Hydroxyl Ion in the Basic Magnesium Carbonate Minarals. *Am. Mineral.* **1971**, *56* (1965), 46–53.

[144] Coleyshaw, Esther E.; Crump, Gregory; Griffith, William P. Vibrational Spectra of the Hydrated Carbonate Minerals Ikaite, Monohydrocalcite, Lansfordite and Nesquehonite. *Spectrochim. Acta - Part A Mol. Biomol. Spectrosc.* **2003**, *59* (10), 2231–2239. https://doi.org/10.1016/S1386-1425(03)00067-2.

[145] Stephan, G. W.; MacGillavry, C. H. The Crystal Structure of Nesquehonite, MgCO $_3$ .3H $_2$ O. *Acta Crystallogr. Sect. B Struct. Crystallogr. Cryst. Chem.* **1972**, *28* (4), 1031–1033. https://doi.org/10.1107/S0567740872003668.

[146] Frost, Ray L.; Palmer, Sara J. Infrared and Infrared Emission Spectroscopy of Nesquehonite Mg(OH)(HCO3)·2H2O–implications for the Formula of Nesquehonite. *Spectrochim. Acta Part A Mol. Biomol. Spectrosc.* **2011**, *78* (4), 1255–1260. https://doi.org/https://doi.org/10.1016/j.saa.2010.12.059.

[147] Hopkinson, Laurence; Kristova, Petra; Rutt, Ken; Cressey, Gordon. Phase Transitions in the System MgO – CO 2 – H 2 O during CO 2 Degassing of Mg-Bearing Solutions. **2012**, *76*, 1–13. https://doi.org/10.1016/j.gca.2011.10.023.

[148] Hales, Matthew C.; Frost, Ray L.; Martens, Wayde N. Thermo-Raman Spectroscopy of Synthetic Nesquehonite – Implication for the Geosequestration of Greenhouse Gases. **2008**, No. March, 1141–1149. https://doi.org/10.1002/jrs.

[149] Kloprogge, J. T.; Martens, W. N.; Nothdurft, L.; Duong, L. V.; Webb, G. E. Low Temperature Synthesis and Characterization of Nesquehonite. *J. Mater. Sci. Lett.* **2003**, *22* (11), 825–829. https://doi.org/10.1023/A:1023916326626.

[150] Jauffret, G. On the Thermal Decomposition of Nesquehonite. *J. Therm. Anal. Calorim.* **2015**, *122* (2), 601–609. https://doi.org/10.1007/s10973-015-4756-0.

[151] Mani, Fabrizio; Peruzzini, Maurizio; Stoppioni, Piero. CO2 Absorption by Aqueous NH3 Solutions: Speciation of Ammonium Carbamate, Bicarbonate and Carbonate by a 13C NMR Study. *Green Chem.* **2006**, *8* (11), 995. https://doi.org/10.1039/b602051h.

[152] Bak, Mads; Rasmussen, Jimmy T.; Nielsen, Niels Chr. SIMPSON: A General Simulation Program for Solid-State NMR Spectroscopy. *J. Magn. Reson.* **2000**, *147* (2), 296–330. https://doi.org/10.1006/jmre.2000.2179.

[153] Cui, Jinlei; Olmsted, David L.; Mehta, Anil K.; Asta, Mark; Hayes, Sophia E. NMR Crystallography: Evaluation of Hydrogen Positions in Hydromagnesite by 13C{1H} REDOR Solid-State NMR and Density Functional Theory Calculation of Chemical Shielding Tensors. *Angew. Chemie Int. Ed.* **2019**, *58* (13), 4210–4216. https://doi.org/10.1002/anie.201813306.

[154] Powell, Jacob; Kalakewich, Keyton; Uribe-Romo, Fernando J.; Harper, James K. Solid-State NMR and DFT Predictions of Differences in COOH Hydrogen Bonding in Odd and Even Numbered: N -Alkyl Fatty Acids. *Phys. Chem. Chem. Phys.* **2016**, *18*, 12541–12549. https://doi.org/10.1039/c6cp00416d.

[155] Andersson, Y.; Langreth, D. C.; Lundqvist, B. I. Van Der Waals Interactions in Density-Functional Theory. *Phys. Rev. Lett.* **1996**, *76* (1), 102–105.